論文 / 著書情報
Article / Book Information

題目(和文)	金電極に架橋したBDT分子の構造と電子状態の解析法の開発及び電子伝導性の解明
Title(English)	Development of system to analyze atomic and electronic structure for elucidation of electron transport property of BDT molecule bridging between Au electrodes
著者(和文)	松下龍二
Author(English)	Ryuji Matsushita
出典(和文)	学位:博士(理学), 学位授与機関:東京工業大学, 報告番号:甲第10072号, 授与年月日:2016年3月26日, 学位の種別:課程博士, 審査員:木口 学,大島 康裕,西野 智昭,沖本 洋一,河合 明雄,北島 昌史
Citation(English)	Degree:Doctor (Science), Conferring organization: Tokyo Institute of Technology, Report number:甲第10072号, Conferred date:2016/3/26, Degree Type:Course doctor, Examiner:,,,,,
学位種別(和文)	博士論文
Type(English)	Doctoral Thesis

博士論文

Development of system to analyze atomic and electronic structure for elucidation of electron transport property of BDT molecule bridging between Au electrodes

金電極に架橋した BDT 分子の構造と電子状態の解析法の開発及び電子伝導性の解明

東京工業大学　理工学研究科　化学専攻
松下　龍二
指導教員：木口　学, 西野　智昭

2016 年 2 月

Acknowledgments

This thesis has been executed under the supervision of Professor Dr. Manabu Kiguchi and Associated Professor Dr. Tomoaki Nishino. I would like to express to the supervisors my deepest gratitude for plenty of fruitful discussion, advices, instructions, supports, and encouragements. I would like to sincerely grateful to Professor Emeritus Dr. Toshiaki Enoki for encouragements and fruitful discussion and suggestions.

I am sincerely grateful to Assistant Professor Satoshi Kaneko and Associated Professor Dr. Shitaro Fujii for their tireless encouragements, significant discussion and advices, and instructions.

I would like to considerably thank Dr. Yasuhisa Naitoh and Dr. Masayo Horikawa in National Institute for Advanced Industrial Science and Technology (AIST) for providing the nanogap electrodes.

I would like to thank Dr. Hisao Nakamura in AIST, Associated Professor Dr. Tomofumi Tada in Tokyo Institute of Technology, Associated Professor Dr. Ryo Yamada in Osaka University, and Professor Dr. Masateru Taniguchi in Osaka University for fruitful discussions and suggestions on the electronic structure of the single atomic/molecular junctions.

I would like to thank Mr. Yuta Takahashi in Enoki-Kiguchi Laboratory and Mr. Yuki Komoto in Kiguchi-Nishino Laboratory for giving me the program for IV measurement. I cannot thank enough my colleagues in Kiguchi-Nishino Laboratory and Enoki – Kiguchi Laboratory for encouragements and unforgettable joyful days.

Finally, many thanks to my family for never-ending support and encouragements.

This work was partially supported by JSPS KAKENHI Grant-in-Aid for JSPS Fellows No. 26011516.

Ryuji Matsushita
Tokyo, February 2016

A list of publications

1, Original papers

1.1. Satoshi Kaneko, Yuuga Nakamura, **Ryuuji Matsushita**, Santiago Marqués-González, Manabu Kiguchi “Simultaneous measurement of electrical conductance and thermopower of single benzenedithiol molecular junctions” *Appl. Phys. Express* **8**, 065201/1 - 065201/4, 2015.

1.2. **Ryuji Matsushita**, Satoshi Kaneko, Shintaro Fujii, Hisao Nakamura, Manabu Kiguchi “Temperature dependence of the thermopower and its variation of the Au atomic contact ” *Nanotechnology* **26**, 045709/1 - 045709/6, 2015.

1.3. **Ryuji Matsuhita**, Masayo Horikawa, Yasuhisa Naitoh, Hisao Nakamura, Manabu Kiguchi “Conductance and SERS Measurement of Benzenedithiol Molecules Bridging Between Au Electrodes” *J. Phys. Chem. C* **117**, pp1791-1795, 2013.

1.4. Yasuhisa Naitoh, Tatsuhiko Ohata, **Ryuji Matsushita**, Eri Okawa, Masayo Horikawa, Makiko Oyama, Masakazu Mukaida, Dong F Scott Wang, Manabu Kiguchi, Kazuhito Tsukagoshi, and Takao Ishida, "Self-Aligned Formation of Sub-1-nm-Gaps Utilizing Electromigration during Metal Deposition", *ACS appl. mater. Interfaces,* **5**, pp12869-12875, 2013.

1.5. Tomoka Nakazumi, Satoshi Kaneko, **Ryuuji Matsushita**, Manabu Kiguchi “Electric Conductance of Single Ethylene and Acetylene Molecules Bridging between Pt Electrodes” *J. Phys. Chem. C* **116**, pp18250-18255, 2012.

1.6. **Ryuji Matsushita**, Satoshi Kaneko, Tomoka Nakazumi, Manabu Kiguchi “Effect of metal-molecule contact on electron-vibration interaction in single hydrogen molecule junction” *Phys. Rev. B* **84**, 245412/1-245412/5, 2011.

2, Reviews and books

2.1. Santiago Marques-Gonzalez, **Ryuji Matsushita**, Manabu Kiguchi, “Surface enhanced Raman scattering of molecules in metallic nanogaps”, *Journal of Optics* **17,** 114001/1 - 114001/14, 2015.

2.2. Manabu Kiguchi, **Ryuji Matsushita**, “Vibration Spectroscopy of Single Molecular Junctions”, in "Molecular Electronics: A Theoretical and Experimental Approach", ed. Ioan Baldea, Pan Stanford Publishing, 2015.

2.3. **Ryuji Matsushita**, Manabu Kiguchi, "Surface Enhanced Raman Scattering of a Single

Molecular Junction", *Phys. Chem. Chem. Phys.*, 2015.

2.4. 木口学, 松下龍二, 金子哲, 中住友香, “単一分子接合の作製およびその物性評価”, *日本画像学会誌*, **52**, 26-33, 2013.

A list of presentations

1, International conferences

1.1. **Ryuji Matsushita**, Satoshi Kaneko, Manabu Kiguchi “Thermopower Measurement of Gold Atomic Junctions”, ECOSS30, Antalya (Turkey), September, 2014.

1.2. **Ryuji Matsushita**, Satoshi Kaneko, Tomoka Nakazumi, Manabu Kiguchi “Effect of molecular vibration excitation by conduction electron on conductance of single hydrogen molecular junction” China-Japan Joint Symposium on Current and Future Molecular Electronics, Nanjing, October, 2011.

2, Domestic conferences

2.1. 松下龍二，金子哲、木口学　“金単原子接合の熱電能の温度依存性”，分子科学討論会，東京, 2015年9月

2.2. 松下龍二，金子哲、木口学　“金単原子接合における熱起電力の揺らぎ”，分子科学討論会，東広島, 2014年9月

2.3. 松下龍二　“1，4‐ベンゼンジチオール分子接合の電気伝導特性と振動スペクトル計測”　第2回ナノスケール分子デバイスセミナー，東京，2013年3月(invited)

2.4. 松下龍二，金子哲，中住友香，木口学　“水素単分子ワイヤの作製およびその電子伝導特性の解明”　表面界面スペクトロスコピー2012（第6回），大阪，2012年12月

2.5. 松下龍二，木口学，堀川昌代，内藤泰久　“Au電極に架橋した1，4-ベンゼンジチオール分子の電子伝導および光学特性の計測”，分子科学討論会，東京，2012年9月

2.6. 松下龍二，木口学，内藤泰久，堀川昌代　“1,4‐ベンゼンジチオール分子接合における電気伝導度とラマンスペクトル計測”　日本物理学会第67回年次大会，兵庫，2012年3月

2.7. 松下龍二，金子哲，中住友香，木口学　“水素単分子接合における伝導電子による分子振動励起効果”　日本物理学会2011年秋季大会，富山, 2011年9月

Contents

1, General introduction

2, Methods to analyze atomic and electronic structure

3, Analysis of atomic structure of 1,4-benzenedithiol molecule bridging between Au electrodes by Surface Enhanced Raman Spectroscopy

4, Development of system to measure thermopower and electrical conductance simultaneously

5, Measurement of thermopower of single Au atomic junction

6, Analysis of atomic and electronic structure of 1,4-benzenedithiol molecule bridging between Au electrodes

1, General introduction

1.1. History and background

Wolfgang Ernst Pauli said, “God made the bulk; surfaces were invented by the devil.” Atoms in low dimensional systems do not have an isotropic environment. As a result, the properties of the atoms are very different from those in the bulk systems. This leads to difficulty in understanding phenomena in the low dimensional systems[1]. In addition, it is difficult to control properties of the low dimensional systems including surfaces because their atomic structures fluctuate and change easily. In spite of these “diabolical” characteristics, low dimensional systems have attracted wide attention because they sometimes provide the novel properties. For example, graphene, a single, tightly packed layer of carbon atoms, displays remarkable electron mobility at room temperature[2].

Among the low dimensional systems, there are structures where a small number of atoms or molecules bridge between metal electrodes. (Fig. 1.1.1.) They are called atomic or molecular junctions[3, 4]. Especially, the junctions are called single atomic or molecular junction when one atom or molecule bridges between the electrodes. The size of atomic and molecular junctions is of the order of the nanometers. The junctions have attracted attention due to its potential application in ultrasmall electronic devices. The utilization of single molecules/atoms as active components in electronic devices leads to a drastic decrease in device size, and increases in the density of the devices and the calculation speed. The utilization of a single molecule in electronic devices has another advantage. The recent development of synthetic techniques makes it possible to design the properties of molecules. The performance of devices can thus be freely controlled by choosing the appropriate molecule and designing its properties. Molecules are mainly made of carbon (C), hydrogen (H), nitrogen (N), and oxygen (O), all of which are present in large amounts on Earth. Hence, high-performance electronic devices can be fabricated without using rare earth elements. The use of single molecules as electronic devices was first proposed by Aviram and Ratner in 1974[5]. They theoretically predicted the diode properties of a molecular junction in which a donor π system and an acceptor π system were connected with an insulating part between the metallic electrodes. (Fig.

1.1.2)

Though it had been difficult to fabricate molecular junctions, the development of technology in nanoscience enabled people to do it. In 1997, Metzger *et al.* fabricated the structure in which a single monolayer of organic molecules was sandwiched between metallic layers by evaporating the metallic layer on the monolayer fabricated on the metallic layer[6]. They measured the IV characteristic for the structure and observed the rectification property. (Fig. 1.1.3) In 2001, Holmin *et al*. fabricated the structure of Ag-SAM(1)SAM(2)-Hg (SAM (N): Self assembled monolayer of organic molecule N)[7]. They measured the electrical conduction characteristic of the structures. (Fig. 1.1.4) In 2009, H. Song *et al*. fabricated the structure in which molecules bridged between the metal electrodes by electromigration technique[8]. (Electromigration technique will be explained in Chapter 3.) They modulated the transport current thorough the molecules by an external gate voltage. (Fig. 1.1.5.)

The development of the technology in nanoscience enabled people to fabricate the structure where a single atom or molecule bridges between the electrodes. In 1998, Ohnishi *et al*. succeeded in the fabrication of a single gold atomic wire by breaking the gold wire[9]. They observed the single atomic wire by transmission electron microscope. (Fig. 1.1.6.) In 1997, Reed *et al*. proposed the Break-Junction (BJ) technique to fabricate single molecular junctions[10]. In BJ technique, the metal wire is broken to make the nanogap in the presence of the target molecules. When a single molecule bridges between the electrodes, a single molecular junction forms. (Fig. 1.1.7. (a)) In 2002, Smit *et al*. fabricated the single hydrogen molecular junction, where a single hydrogen molecule bridged between the Pt electrodes, by mechanically controllable break junction (MCBJ) technique[11]. (MCBJ is a kind of BJ technique and will be explained in Chapter 5.) They characterized the single molecular junction by point contact spectroscopy (PCS) which is one of the methods for vibrational spectroscopy. (Fig. 1.1.7. (b), PCS will be explained in Chapter 2.) Some research groups fabricated the single molecular junctions which had the functionality such as switching property and diode property[12, 13]. (Fig. 1.1.8.)

In the study of the atomic and molecular junctions, electrical conductance of a single atom or molecule is used to estimate the number of atoms or molecules bridging between the electrodes. To estimate electrical conductance of a single atom or molecule, the conductance trace is measured. This is the record of the conductance in the breaking process of the metal wire. When the atomic or molecular junction forms, the plateau appears in the trace. By collecting the traces, the conductance histogram is constructed. In the histogram, the peaks appear because of the plateaus in the traces. A peak with the smallest conductance is always regarded as the conductance of a single atomic or molecular junction. (Fig. 1.1.9.) In 2003, Xu *et al*. measured the conductance histogram for gold/1, 4-benzenedithiol (BDT) system (Fig. 1.1.10.). They estimated the value of a single BDT molecule bridging between gold electrodes to be 0.01 G_0[14]. (G_0 is quantized conductance. $G_0 = 2e^2/h = 13\ \mathrm{k\Omega}$, e: elementary charge, h: Plancks constant)

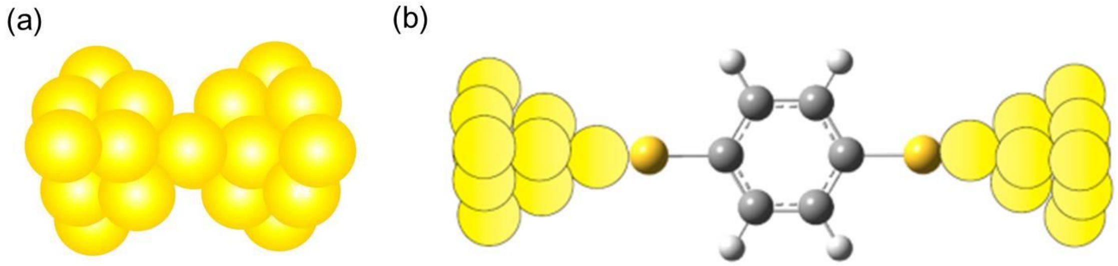

Fig. 1.1.1.Shematic views of atomic (a) and molecular (b) junctions.

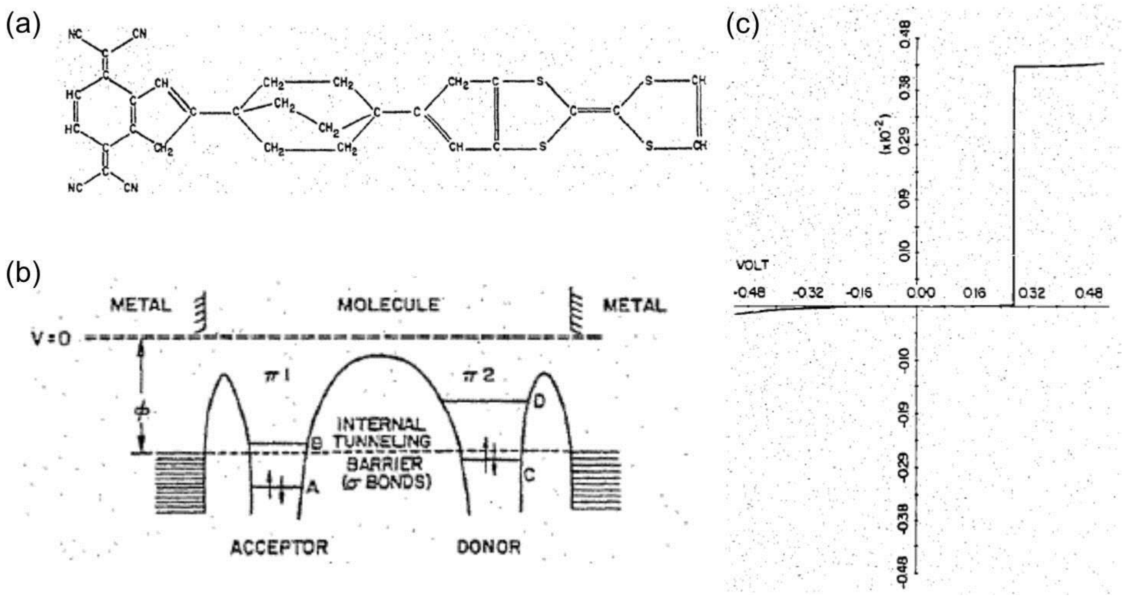

Fig.1.1.2. (a) An example of a rectifier molecule. (b) Energy versus distance of the device (schematic). B and D are the affinity levels and A and C the highest occupied levels, of acceptor and donor, respectively. (c) Current-bias voltage characteristics of a molecular rectifier including direct electrode to electrode tunneling. Current in A/cm^2, bias voltage in volt. Reprinted with permission from A. Aviram and M. A. Ratner, Molecular Rectifiers ,*Chemical Physics Letters*, 1974, 29, 277. Copyright 1974 Elsevier.[5]

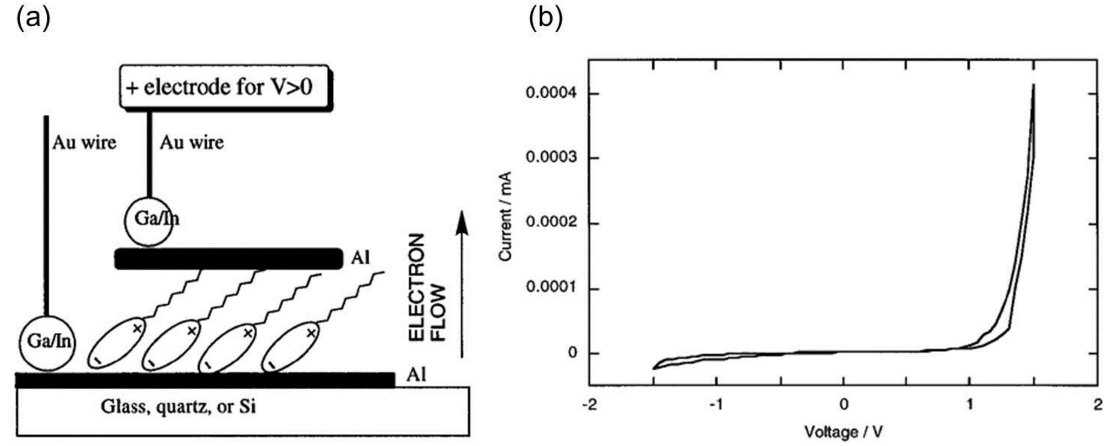

Fig. 1.1.3.(a) Orientation of the Langmuir Blodgett monolayer on the glass, quartz, or Si substrate; the electrode (+) for positive bias, and the direction of “easy” electron flow for *V* > 0 are marked. (b) Rectification through a single monolayer sandwiched between Al electrodes (top Al pad area 4.5 mm^2, thickness 100 nm), using Ga/In eutectic and Au wires. The dc voltage is swept at a rate of 10 $mV\ s^{-1}$. Reprinted with permission from R. M. Metzger, B. Chen, Ulf Ho1pfner, M. V. Lakshmikantham, D. Vuillaume, T. Kawai, X. Wu, H. Tachibana, T. V. Hughes, J. Hiromi Sakurai, W. Baldwin, C. Hosch, M. P. Cava, L. Brehmer and G. J. Ashwell, Unimolecular Electrical Rectification in Hexadecylquinolinium Tricyanoquinodimethanide ,*Journal of the American Chemical Society*, 1997, 119, 10455. Copyright 1997 American Chemical Society.[6]

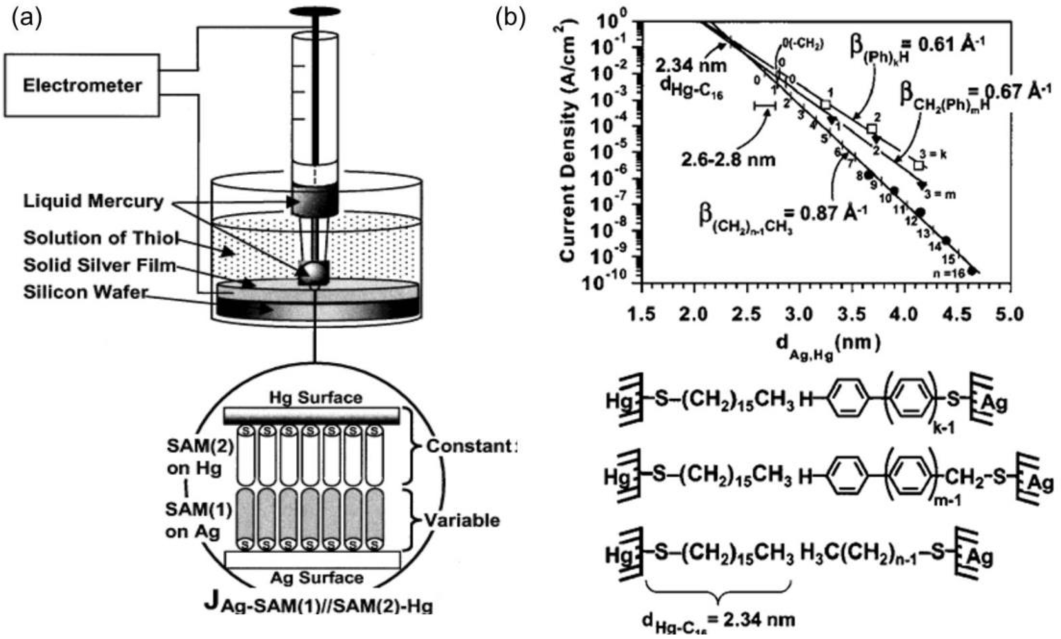

Fig.1.1.4. (a) Schematic illustration of a Ag-SAM(1) SAM(2)-Hg junction. (b) Plot comparing the distance dependence of the current density in Ag-SAM(1) C_{16}-Hg junctions (C_{16}: $HS(CH_2)_{15}CH_3$) for SAMs composed of aliphatic thiols ($HS(CH_2)_{n\text{-}1}CH_3$; solid circles) and for SAMs composed of oligophenylene thiols ($HS(Ph)_kH$; open squares) and for their benzylic homologues ($HSCH_2(Ph)_mH$; solid triangles). Current densities were obtained at 0.5 V bias. The solid lines through the data points correspond to computer-generated, linear least squares fits of the natural log of current density to $\ln(I) = -\beta d_{Ag,Hg} + \ln(I_0)$. β and $d_{Ag,Hg}$ are the structure-dependent attenuation factor and the distance between the electrodes, respectively. Lower illustrations show the schematic representation of junctions formed from the three classes of thiols. Reprinted with permission from R. E. Holmlin, R. Haag, M. L. Chabinyc, R. F. Ismagilov, A. E. Cohen, A. Terfort, M. A. Rampi and G. M. Whitesides, Electron Transport through Thin Organic Films in Metal−Insulator−Metal Junctions Based on Self-Assembled Monolayers, *Journal of the American Chemical Society*, 2001, 123, 5075. Copyright 2001 American Chemical Society.[7]

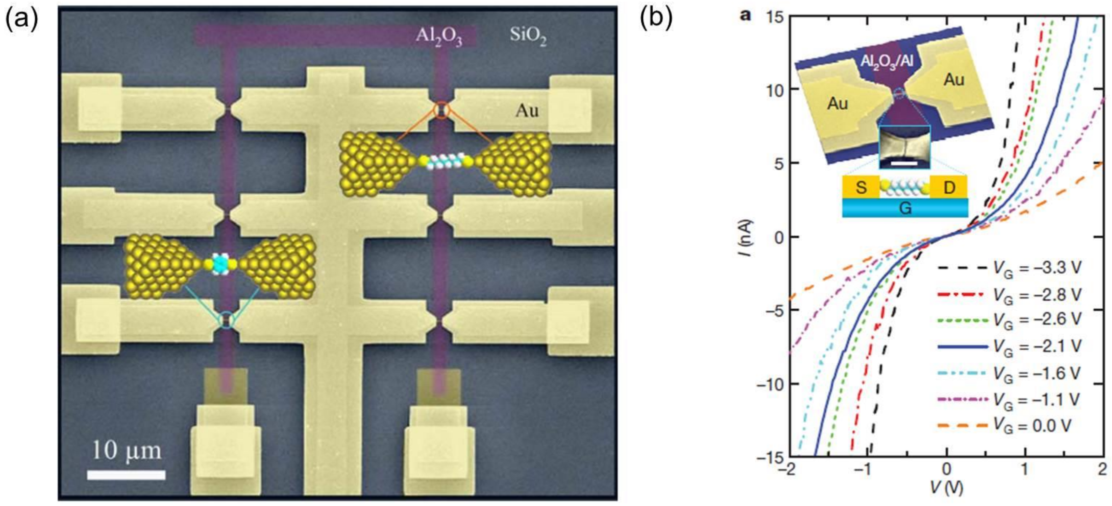

Fig. 1.1.5. (a) Scanning electron microscope image (false color) illustrating a full pattern of the devices to apply the gate voltage to the molecular junctions. The whole structure was defined on an oxidized Si wafer. The yellow regions show portions of the multi-layered Au electrodes (a thin Au layer with a thickness of ~15 nm; a thick Au layer with a thickness of ~100 nm), and the purple region represents the oxidized Al gate electrode. Au wires broken by the electromigration technique are placed on the top of the bottom-gate electrode. (b) Gate-controlled charge transport characteristics of ODT(1,8-octanedithiol) molecules bridging between Au electrodes. Representative IV curves measured at 4.2 K for different values of gate voltage. Inset, the device structure and schematic. S, source; D, drain; G, gate. Scale bar, 100 nm. Reprinted with permission from H. Song, Y. Kim, Y. H. Jang, H. Jeong, M. A. Reed and T. Lee, Observation of molecular orbital gating, *Nature*, 2009, 462, 1039. Copyright 2009 Nature Publishing Group. [8]

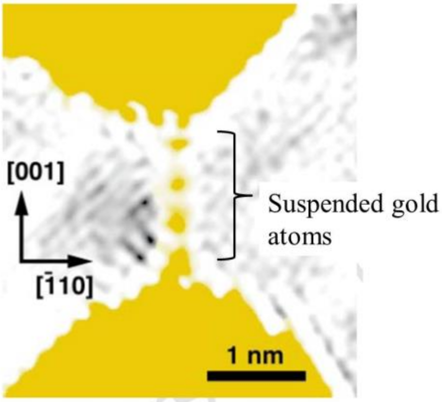

Fig. 1.1.6. Electron microscope image of a linear strand of gold atoms (four coloured dots) forming a bridge between two gold films (coloured areas). The spacings of the four gold atoms are 0.35–0.40 nm. The strand is oriented along the [001] direction of the gold (110) film. Adapted with permission from H. Ohnishi, Y. Kondo and K. Takayanagi, Quantized conductance through individual rows of suspended gold atoms, *Nature*, 1998, 395, 780. Copyright 1998 Nature Publishing Group.[9]

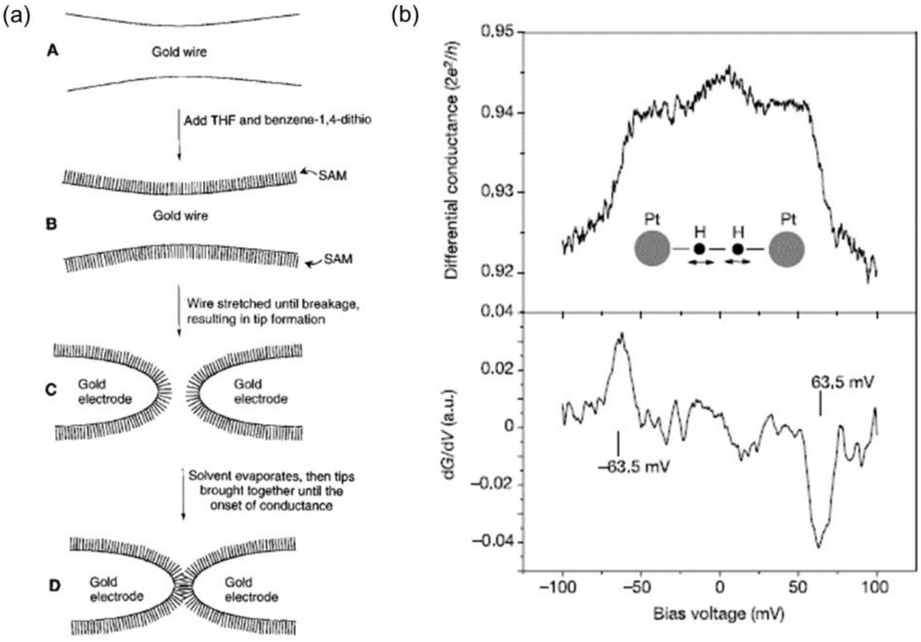

Fig.1.1.7. (a) Schematic illustration of break junction (BJ) technique. Reprinted with permission from M. A. Reed, C. Zhou, C. J. Muller, T. P. Burgin and J. M. Tour, Conductance of a Molecular Junction, *Science*, 1997, 278, 252. Copyright 1997 AAAS.[10] (b) Vibrational spectroscopy of a single hydrogen molecule bridging between platinum electrodes. Reprinted with permission from R. H. M. Smit, Y. Noat, C. Untiedt, N. D. Lang, M. C. van Hemert and J. M. van Ruitenbeek, Measurement of the conductance of a hydrogen molecule, *Nature*, 2002, 419, 906. Copyright 2002 Nature Publishing Group. [11]

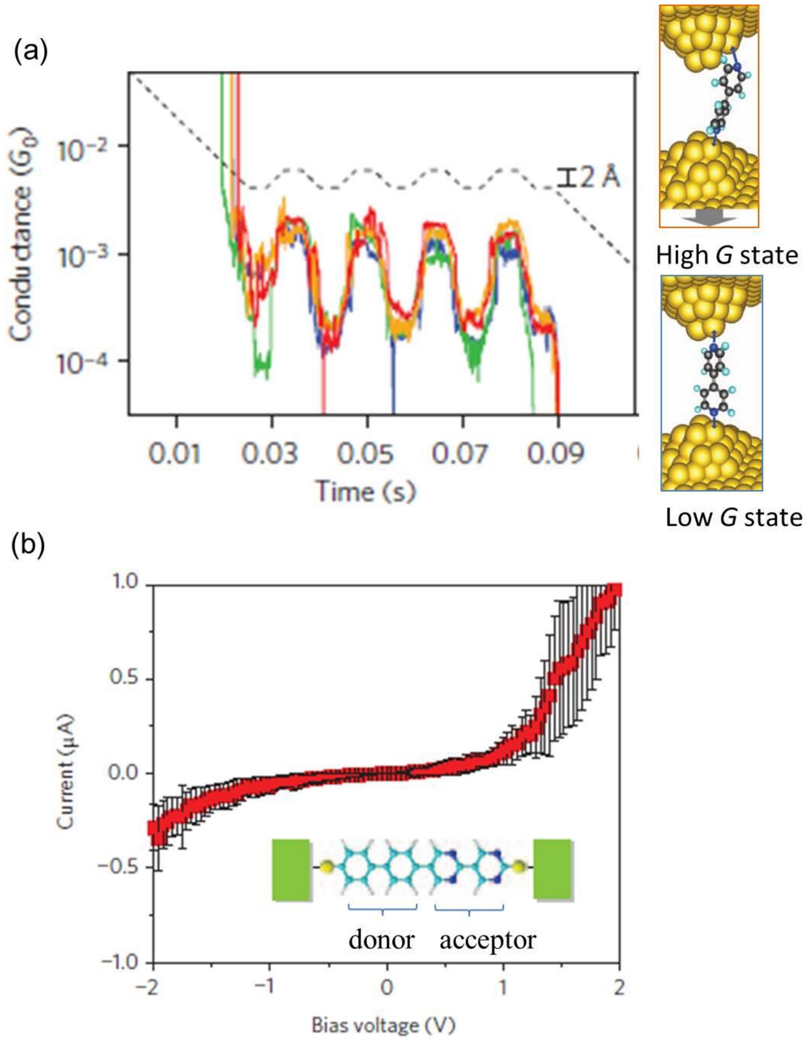

Fig. 1.1.8. (a) Controlled conductance switching by mechanical manipulation of gold–gold distances. 4,4’-bipyridine–gold single-molecule junctions can be reversibly switched between two conductance states through repeated junction elongation and compression. Schematics illustrate the high G (upper) and low G (lower) states, respectively. Reprinted with permission from S. Y. Quek, M. Kamenetska, M. L. Steigerwald, H. J. Choi, S. G. Louie, M. S. Hybertsen, J. B. Neaton and L. Venkataraman, Mechanically controlled binary conductance switching of a single-molecule junction, *Nature Nanotechnology*, 2009, 4, 230-234. Copyright 2009 Nature Publishing Group. [12] (b) IV characteristics for the non-symmetric molecules shown in the graph. Diode property appeared. Adapted with permission from I. Diez-Perez, J. Hihath, Y. Lee, L. Yu, L. Adamska, M. A. Kozhushner, Oleynik, II and N. Tao, Rectification and stability of a single molecular diode with controlled orientation, *Nature Chemistry*, 2009, 1, 635. Copyright 2009 Nature Publishing Group.[13]

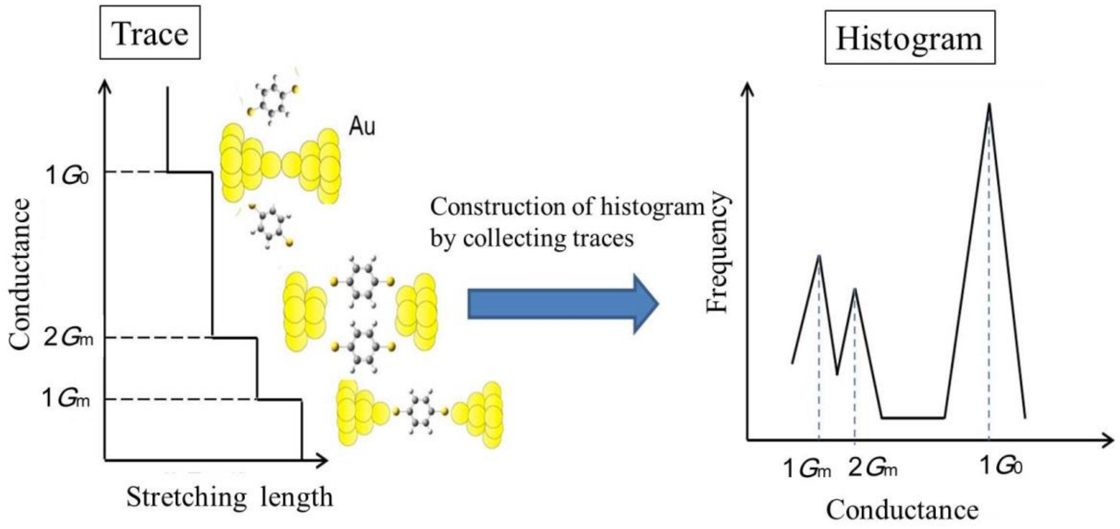

Fig.1.1.9. Schematic illustration of the measurement of the conductance trace (left) and histogram (right). G_m: conductance of a single molecule. The Plateau and peak at $1G_0$ correspond to the formation of the single gold atomic junction.

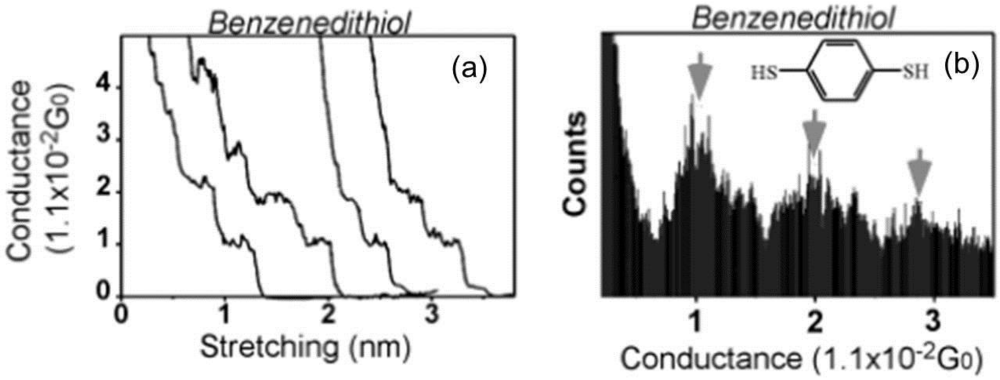

Fig. 1.1.10. Conductance trace (a) and histogram (b) for gold/BDT system. Reprinted with permission from B. Q. Xu and N. J. J. Tao, Measurement of Single-Molecule Resistance by Repeated Formation of Molecular Junctions, *Science*, 2003, 301, 1221-1223. Copyright 2003 AAAS.[14]

1.2. Electron transport of atomic/molecular junctions

1.2.1. Electron transport in metallic nanowire

The electrical conductance in macroscopic metallic wire is described by Ohm's low, which describes the proportionality of the current to the applied voltage. For a given sample, the constants of proportionality (conductance G) can be described by

$$G = \sigma S / L \qquad \text{1-2-1}$$

where σ, S, L are the conductivity, the transverse area, and the length, respectively. G is proportional to S and inversely proportional to L. However, the Ohm's low is not applicable at the atomic scale.

In the sample, there are impurities which scatter electrons. When the length of the sample L is much larger than the elastic mean free path l, the electron motion can be viewed as a random walk of step size l among the impurities in the semi-classical picture. (diffusive transport, Fig. 1.2.1.(a)) On the other hand, when L is smaller than l, the electron momentum can be assumed to be constant. (ballistic transport, Fig. 1.2.1.(b)) In ballistic transport, electron behavior cannot be described in the semi-classical way. Here, let me consider the transport in the one dimensional nanometer sized wire[15]. In this system, the electron is trapped in two directions (x, y) and free in one direction (z). Then, wave function ϕ and energy $E_{\mathrm{i,j}}(\mathrm{k}_z)$ (k_z is the z component of the wave vector) can be described by

$$\phi(x, y, z) = \phi_{\mathrm{i,j}}(x, y)\exp(\mathrm{i}k_z z) \qquad \text{1-2-2}$$

$$E_{\mathrm{i,j}}(k_z) = \varepsilon_{\mathrm{i,j}} + \hbar^2 k_z^2 / 2m \qquad \text{1-2-3}$$

where i and j are the quantum numbers to describe the eigenstate in the xy plane. The dispersion relation described in eq.1-2-3 shows the formation of subband as shown in Fig. 1.2.2.

As discussed above, the behavior of electron is quantized in one dimensional system. Each states can be responsible for the electron transport. The conductance G of the one dimensional system can be described with the Landauer formula by

$$G = \frac{2e^2}{h}\sum_n \tau_n(E_F) = G_0 \sum_n \tau_n(E_F) \qquad \text{1-2-4}$$

where E_{F} and $\tau_{\mathrm{n}}(E_{\mathrm{F}})$ are Fermi level and transmission of n-th current-carrying eigenmode at Fermi level. The constant G_0 is equal to 77.5 μS (=12.9 kΩ). In order to determine the total conductance, one has to solve the Schrödinger equation, find the current-carrying eigenmmodes, calculate their transmission values and sum up their contributions. [3]

1.2.2. Electron transport in single molecular junction

In a conventional single molecular junction, molecules are attached to the metal electrodes via anchoring groups[4]. The thiol group is the most popular anchoring group and Au is most widely utilized as metal electrodes for single molecular junctions. This is because stable single molecular junctions can be prepared using a strong covalent Au–S bond. However, thiol groups act as resistive spacers between the electrodes and the molecule. The two anchors can be regarded as the two potential barriers. (Fig. 1.2.3.) Before discussing the electron transport in the single molecular junction, let me describe the one in the double barrier system shown in Fig. 1.2.4. In the following, the total transmission T of the double barrier system will be derived.

To calculate T, we need to obtain the expression of total transmission amplitude of the double barrier t. The amplitude t can be described by[15]

$$t = \frac{t_1 t_2 e^{ikd}}{1 - r_1 r_2 e^{2ikd}} \qquad \text{1-2-5}$$

where t_i, r_i, d, k are transmission and reflectance amplitude of i (=1, 2) th barrier, distance between two barriers, and wave number of electron, respectively. Then, the total transmission T (= $|t|^2$) can be described by

$$T = \frac{T_1 T_2}{1 - 2\sqrt{R_1 R_2}\cos\theta + R_1 R_2} \qquad \text{1-2-6}$$

where T_i, $R_{i,}$, θ are $|t_i|^2$, $|r_i|^2$, and the total phase, respectively. When $\theta = 2n\pi$ (n: integer), T is the maximum value of $T_1 T_2 / (1 - R_1^{0.5} R_2^{0.5})^2$. This means that there are resonance levels between the barriers. Electrons can transmit the double barrier with the maximum probability when the energy (or wave vector) of electron correspond to the resonance level.

Here, let me consider the case of $\theta = 2kd$. The wavenumber k_0 is set so as to satsfy the condition of $2k_0d = 2n\pi$. If T_1, $T_2 < 1$ and the difference between k and k_0 is small, T can be approximated by[3]

$$T \cong \frac{4\Gamma_L\Gamma_R}{(E-\varepsilon_0)^2 + (\Gamma_L + \Gamma_R)^2} \qquad \text{1-2-7}$$

where $\varepsilon_0=\hbar^2k_0^2/2m$, $E = \hbar^2k^2/2m$, $\Gamma_L=\hbar^2k_0T_1/4dm$, $\Gamma_R=\hbar^2k_0T_2/4dm$, respectively. Now, the total transmission has a Lorentzian type shape. Γ (= $\Gamma_L + \Gamma_R$) corresponds to the width of the resonant peak. The formula in eq.1-2-7 is called Breit-Wigner formula.

Next, let me discuss the electron transport in the single molecular junction. Assuming that one molecular level (HOMO or LUMO) dominates transport, as is often the case in molecular junctions, the transmission function is also represented by Lorentzian:

$$\tau(E,V) = \frac{4\Gamma_L\Gamma_R}{[E-\varepsilon_0(V)]^2 + [\Gamma_L + \Gamma_R]^2} \qquad \text{1-2-8}$$

where V, $\varepsilon_0(V)$ and $\Gamma_{L(R)}$ are the applied voltage between the electrodes, the energy of the conduction orbital in the presence of the applied voltage V, and the coupling between molecule and left (right) electrode, respectively. (Fig. 1.2.5.)

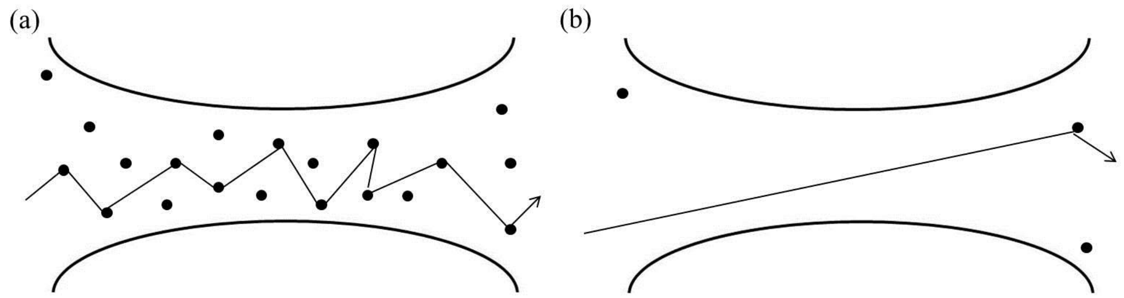

Fig.1.2.1. Schematic illustration of a diffusive (a) and ballistic (b) conductor.

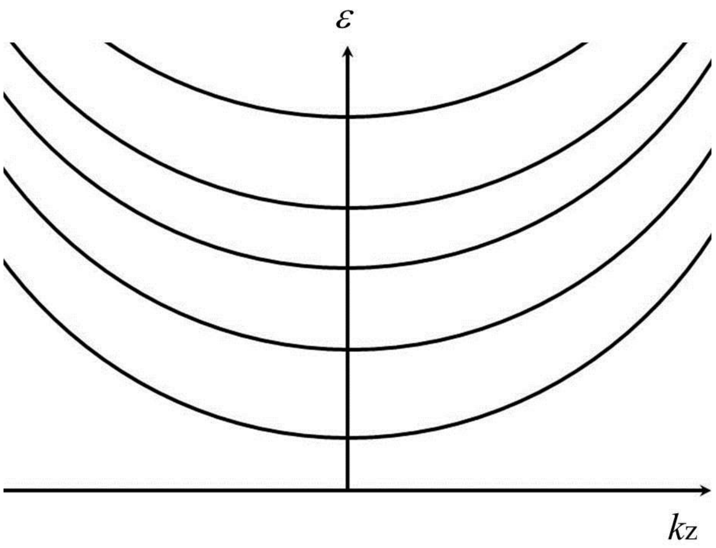

Fig. 1.2.2. Dispersion relation in in the nanometer sized wire.

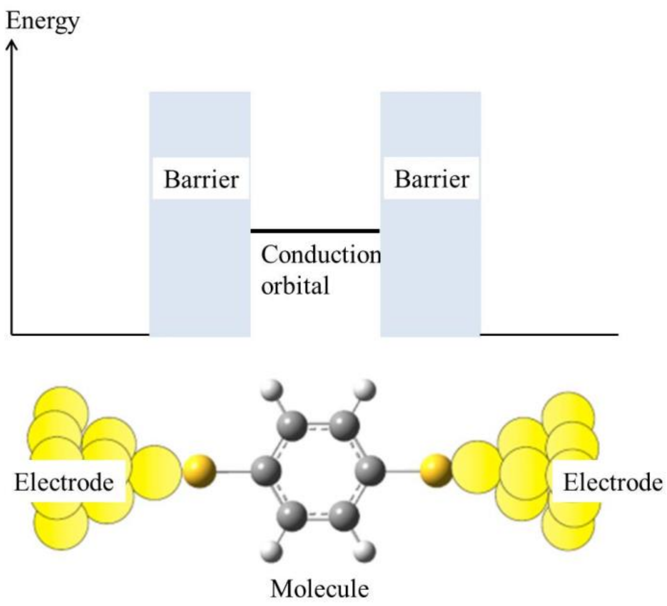

Fig. 1.2.3. Schematic illustration of single molecular junction with anchors. Two anchors are regarded as the two potential barriers.

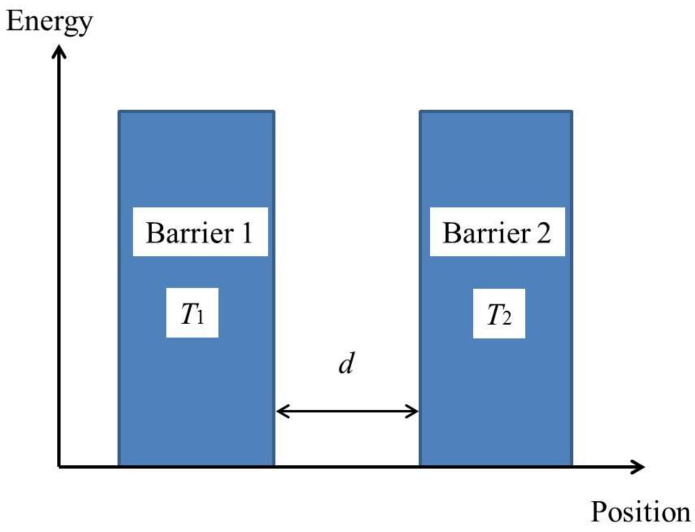

Fig.1.2.4. Schematic illustration of the double barrier system. d: distance between the two barriers, $T_{1(2)}$: transmission of barrier 1 (2).

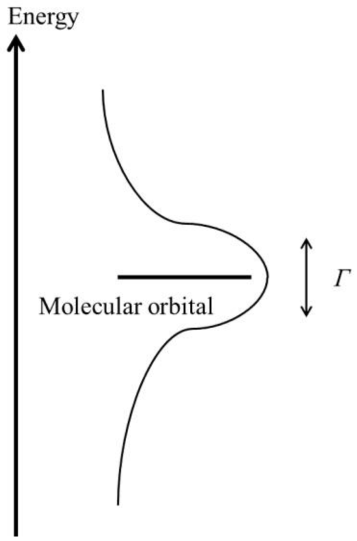

Fig. 1.2.5. Schematic illustration of the energy diagram.

1.3. Purpose of this study

To exploit the physical properties of the molecular junction, it is necessary to understand their origin. The physical property is determined by the atomic and electronic structure of the junction. Therefore, analyzing the atomic and electronic structure is needed to understand the origin.

Molecular junctions are atomic-sized system. Their atomic and electronic structures fluctuate easily, which results in the fluctuation of the physical property. This instability makes people difficult to use the molecular junctions as the electronic device. On the other hand, the molecular junction can be regarded as the system which can show a variety of values of the physical property. In the dynamics of the molecular junction, the junctions show a variety of values of the physical property. To understand the origin of them appearing in the dynamics, it is necessary to analyze the atomic and electronic structure of the junctions in the dynamics.

Some studies have been performed to analyze the atomic and electronic structures of the molecular junctions in the dynamics. Ward *et al*. and Konishi e*t al*. succeeded in the simultaneous conductance and SERS measurements of the molecular junction in the dynamics.[16, 17] They observed the appearance of the b_2 modes for the molecular junctions, which were not observed in the bulk crystal. While the combination of SERS and conductance measurement of the molecular junctions is a powerful technique to characterize the molecular junction, most previously reported experimental measurements have been limited to the conductance near zero bias. To analyze the electronic structure of the junctions, it is necessary to perform the analyses such as IV characteristics measurement or thermopower measurement. IV characteristic measurements provide the energy difference between conduction orbital and Fermi level. Thermopower measurements provide the slope of the transmission curve at the Fermi level. To analyze the atomic structure of the junction, it is necessary to perform the vibrational spectroscopy such as SERS (Surface Enhanced Raman Spectroscopy) and IETS (Inelastic Electron Tunneling Spectroscopy). (Each method will be explained in the Chapter 2.) Combining these methods enable people to understand the atomic and electronic structure comprehensively in the dynamics of the molecular junctions. In this study, measurement systems were constructed to analyze the atomic and electronic structure of the junction in situ. To perform the analysis, I applied the methods above for 1, 4-benzendithiol molecules bridging between the gold electrodes. (Au/BDT junction) The electron transport property of Au/BDT junctions has been studied well in terms of the theory and experiment. Therefore, I can refer to the previous studies to understand my experimental results in detail.

First, SERS was performed with the measurements of the IV characteristics for Au/BDT junctions. The measured IV characteristics provided the information on the number of molecules bridging metal electrodes, and energy difference between conduction orbital and Fermi level. SERS measurement provided the basic information on the atomic structure of the Au/BDT junctions. (Chapter 3)

Then, the system for the simultaneous measurement of conductance and thermopower was constructed to get the information of the slope of the transmission curve at the Fermi level. Thermopower measurements of the platinum-steel thermocouple were performed to check whether the thermopower measurements can be performed properly with the system. (Chapter 4)

After the construction of the system, simultaneous measurements of thermopower and conductance were performed for the single gold atomic junctions. The measurements were performed to (1) check whether the thermopower measurements can be performed properly for the atomic-sized system and (2) elucidate the thermoelectric property of the single gold atomic junctions which were used as the electrodes in the Au/BDT junctions. (Chapter 5)

Finally, thermopower measurements were performed for the Au/BDT junctions around room temperature and at low temperature. In addition to the thermopower measurement, IETS and IV characteristics were also measured at low temperature in situ to elucidate the atomic and electronic structure comprehensively in the dynamics of the junctions. (Chapter 6)

2, Methods for analyzing atomic and electronic structure

2.1 Surface enhanced Raman spectroscopy (SERS)

The irradiation of incident light on material results in emission of scattering light whose wavelength differs from that of the incident light[18]. (Fig.2.1.1.) This phenomenon (Raman effect) is a kind of optical phenomenon in which light interacts with material. By collecting and analyzing the scattering light, people can get structural information of material. The first report about Raman effect was published in 1928 by C. Raman and K Krishnan[19]. Raman effect is partially originated from modification of polarizability of molecule by vibrational modes. Therefore, we can perform vibrational spectroscopy using Raman effect. (Raman spectroscopy) In the following, let me explain the Raman scattering by molecular vibration classically.[18]

Electric field of the incident light E_i can be described by

$$E_\mathrm{i}=E\cos(\omega_\mathrm{i} t) \qquad \text{2-1-1}$$

where E, ω_i, t are the amplitude, frequency, and time, respectively. When the incident light interacts with the molecule, dipole moment μ is induced. Dipole moment μ is described by

$$\mu = \alpha E_\mathrm{i} \qquad \text{2-1-2}$$

where α is the polarizability of the molecule. As mentioned above, the polarizability is modified by the molecular vibration. Using Taylor expansion around the equilibrium position, α can be expressed as follows.

$$\alpha = \alpha_0 + \left(\frac{\partial\alpha}{\partial Q}\right)_0 Q \qquad \text{2-1-3}$$

Here, α_0, Q, $(\partial\alpha/\partial Q)_0$ are the polarizability at the equilibrium position, the normal coordinate, and the derivative of α at the equilibrium position, respectively. Q is described by

$$Q = Q_0\cos\omega t \qquad \text{2-1-4}$$

where Q_o and ω_k are the amplitude and frequency of the vibrational mode. By using equations (2-1-1) ~ (2-1-4), the following expression is obtained.

$$\mu=\alpha_0 E_i\cos\omega_0 t + \frac{1}{2}\,\alpha E_i\cos(\omega_0 - \omega)t \qquad \text{2-1-5}$$

$$+\frac{1}{2}\,\alpha E_i \cos(\omega_0+\omega)t$$

The induced dipole moment μ contains the three components. The oscillating dipole emits the electric field (scattering light) whose frequency is equal to that of the oscillating dipole. The scattering related the first term, second term, and third term in eq.2-1-5 are known as Rayleigh scattering, Stokes scattering, and anti-Stokes scattering, respectively. By collecting Stokes or anti-Stokes scattering light, vibrational spectroscopy can be performed. Stokes scattering light is always used in the Raman spectroscopy because the intensity of the Stokes scattering light is higher than that of anti-Stokes scattering light. In the following, SERS will be explained.

In the 1970's, it was found that the Raman scattering cross section of molecules adsorbed on the roughed noble metal substrate is remarkably larger than that of free molecules[18, 20]. This phenomenon (Surface Enhanced Raman Scattering) enhances the intensity of the Raman signal and enables people to get structural information of low concentration analytes on the metal substrate. The spectroscopy with the use of surface enhanced Raman scattering (Surface Enhanced Raman Spectroscopy, SERS) has been utilized to perform the vibrational spectroscopy for molecules at the interface. In 1997, Nie and Emory demonstrated the detection of single fluorescent molecules (R6G) using silver nanoparticles. (Fig. 2.1.2.) [21] The enhancement factors of the Raman signal were estimated to be the order of $10^{14}\sim10^{15}$. The signal enhancement in SERS is thought to be originated from electromagnetic (EM) and chemical (CM) effects .I will explain each effect below.

EM effect is related to the enhancement of the electric field at the nanometer-sized metal structure by the excitation of plasmon. Plasmon is generated by the incident light when an oscillation of electrons takes place. The oscillation affects the electric field in the system.[15, 22] Here, let me consider the nanoparticle irradiated by the electromagnetic wave. When the wavelength of the electromagnetic wave is larger than the size of the nanoparticle, the nanoparticle is considered to be in the homogeneous field. Then, a single dipole is induced in the particle. An electric field $\boldsymbol{E}(\boldsymbol{r},\,t)$ is induced at $\mathbf{r}$ by the oscillating dipole $\boldsymbol{p}$ positioned in vacuum at the origin as follows.

$$\boldsymbol{E}\,(\mathrm{r},\mathrm{t}) = \frac{1}{4\pi\varepsilon_0}\left\{-\frac{\boldsymbol{p}(t_0)}{r^3}+\frac{3\boldsymbol{r}[\boldsymbol{r}\cdot\boldsymbol{p}(t_0)]}{r^5}-\frac{\dot{\boldsymbol{p}}(t_0)}{cr^2}\right. \qquad \text{2-1-6}$$

$$+\frac{3\boldsymbol{r}[\boldsymbol{r}\cdot\dot{\boldsymbol{p}}(t_0)]}{cr^4}+\frac{\boldsymbol{r}\times[\boldsymbol{r}\times\ddot{\boldsymbol{p}}(t_0)]}{c^2r^3}\Bigg\}$$

Here, $r = |\boldsymbol{r}|$, $t_0 = t - r/c$ (c: light speed in vacuum). $\dot{\boldsymbol{p}}$ and $\ddot{\boldsymbol{p}}$ are the first and second derivative with respect to time, respectively. In eq.2-1-6, the first two terms, the second two terms, and the last term are called static field, induction field, and radiation field, respectively. The static and induction fields are proportional to r^{-3} or r^{-2}. On the other hand, the radiation field is proportional to r^{-1}. The static and induction fields are near field components. the radiation field is a far field component. At the nano-sized structures, an enhanced electric field (near field light) is induced by the excitation of plasmon. The property of the near field light depends on the wavelength of incident light, structure, and metal (Cu or Au or Ag or ···). Fig. 2.1.3. shows the simulated results of the electric field at the nano-sized structure[23]. In the result of Fig. 2.1.3. (b), the enhancement factor of the electric field is on the order of 10^6. When the enhancement factor of the electric field is f, that of the Raman signal is f^4. SERS depends on the structure (gap size, shape, etc.) ,metal, and incident light. Ikeda *et al.* performed the Raman spectroscopy for self-assembled monolayer of 4-chlorophenyl-isocyanide (CPI-SAM) at Pt (100) facet[24]. When the gold nanoparticles were put on the SAM, the Raman signals were enhanced. On the other hand, the Raman signal was not detected when no gold nanoparticles were put on the SAM. (Fig. 2.1.4.) The enhancement was considered to be induced by the excitation of the plasmon between the nanoparticles and the facet.

CM effect is related to the light induced resonant charge transfer between metal and molecules (Fig. 2.1.5.). Lombardi *et al.* proposed the charge transfer theory for SERS on the basis of the idea that vibrations may cause mixing electronic states (Herzberg-Teller theory). Raman tensor elements can be represented by three terms (A term, B term and C term) as follows. [25]

$$\alpha = A + B + C \qquad \text{2-1-7}$$

The totally symmetric modes can be enhanced by all three terms, while the non-totally symmetric modes can be enhanced by terms B and C. Terms B and C arise from the mixing between some electronic states by a particular vibration. Terms B and C can be represented by as follows.

$$B = \sum_{K \neq I} \sum_{k} \sum_{M \neq K} \left[\frac{M_{IK}^{\sigma} h_{KM} M_{MI}^{\rho}}{(h/2\pi)(\omega_{KI} - \omega)} + \frac{M_{IK}^{\rho} h_{KM} M_{MI}^{\sigma}}{(h/2\pi)(\omega_{KI} + \omega)} \right] \qquad \text{2-1-8}$$

$$\frac{<i|k><k|Q|f>}{(h/2\pi)\omega_{MK}} + \left[\frac{M_{IM}^{\sigma} h_{MK} M_{KI}^{\rho}}{(h/2\pi)(\omega_{KI} - \omega)} + \right.$$

$$\left. \frac{M_{IM}^{\rho} h_{MK} M_{KI}^{\sigma}}{(h/2\pi)(\omega_{KI} + \omega)} \right] \frac{<i|Q|k><k|f>}{(h/2\pi)\ \omega_{MK}}$$

$$C = \sum_{K \neq I} \sum_{k} \sum_{M \neq I} \left[\frac{h_{IM} M_{MK}^{\sigma} M_{KI}^{\rho}}{(h/2\pi)(\omega_{KI} - \omega)} + \frac{h_{IM} M_{MK}^{\rho} M_{KI}^{\sigma}}{(h/2\pi)(\omega_{KI} + \omega)} \right] \qquad \text{2-1-9}$$

$$\frac{<i|k><k|Q|f>}{(h/2\pi)\omega_{IM}} + \left[\frac{M_{IK}^{\sigma} M_{KM}^{\rho} h_{MI}}{(h/2\pi)(\omega_{KI} - \omega)} + \right.$$

$$\left. \frac{M_{IK}^{\rho} M_{KM}^{\sigma} h_{MI}}{(h/2\pi)(\omega_{KI} + \omega)} \right] \frac{<i|Q|k><k|f>}{(h/2\pi)\ \omega_{IM}}$$

Here, I, i, K, and k are ground states and excited states of electronic and vibronic state, respectively. In addition, each notation has the meaning as follows.

M_{AB}: electronic transition moment between the state A and B

h_{AB}: degree of mixing of the states A and B by a particular vibration

Q: normal coordinate

ω: energy of the incident light

ω_{AB}: energy gap between the states A and B

ρ, σ: three dimensional directions (x, y, z)

Terms B and C represent molecule-to-metal and metal-to-molecule charge transfer transition, respectively. These transitions obtain their intensity through intensity borrowing from an allowed transition of the molecule from a ground state to a excited state. Osawa *et al.* reported the SERS spectra of p-aminothiophenol (PATP) on Ag surfaces with different morphologies and compared it to conventional Raman spectra of PATP.[26] In that work, a rough Ag surface was prepared by thermal evaporation of Ag onto a CaF_2 substrate. Fig.2.1.6. shows the SERS spectrum of PATP adsorbed on a rough Ag substrate (top) and the conventional Raman spectrum of PATP (bottom). In contrast with the multiple peaks observed in the conventional spectrum, the SERS spectrum of PATP on a rough Ag substrate is dominated by substantially enhanced signals at 1573, 1440, 1391 and 1142 cm^{-1}. These peaks were assigned to the fundamental ring non-totally symmetric b_2 vibrational modes. The origin of appearance of the b_2 modes was attributed to the CM effect.

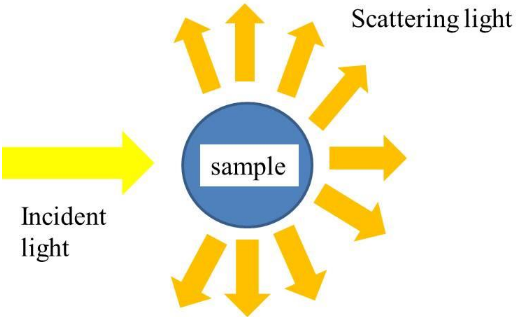

Fig.2.1.1. Raman scattering effect. The wavelength of the incident light differs from that of the scattering light.

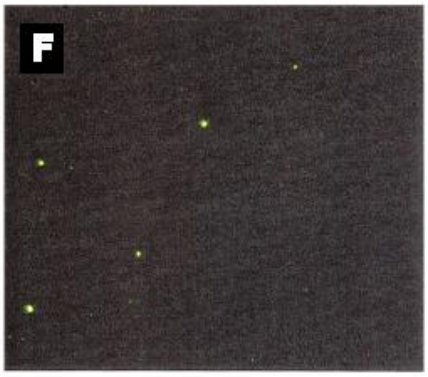

Fig.2.1.2. Filtered photograph taken from Ag colloid incubated with 2×10^{-9} M R6G. A high-performance bandpass filter was used to remove the scattered laser light and to pass Stokes-shifted Raman signals from 540 to 580 nm (920 to 2200 cm^{-1}). Continuous-wave excitation at 514.5 nm was provided by an Ar ion laser. Reprinted with permission from S. Nie and S. R. Emory, Probing Single Molecules and Single Nanoparticles by Surface-Enhanced Raman Scattering, *Science*, 1997, 275, 1102. Copyright 1997 AAAS.[21]

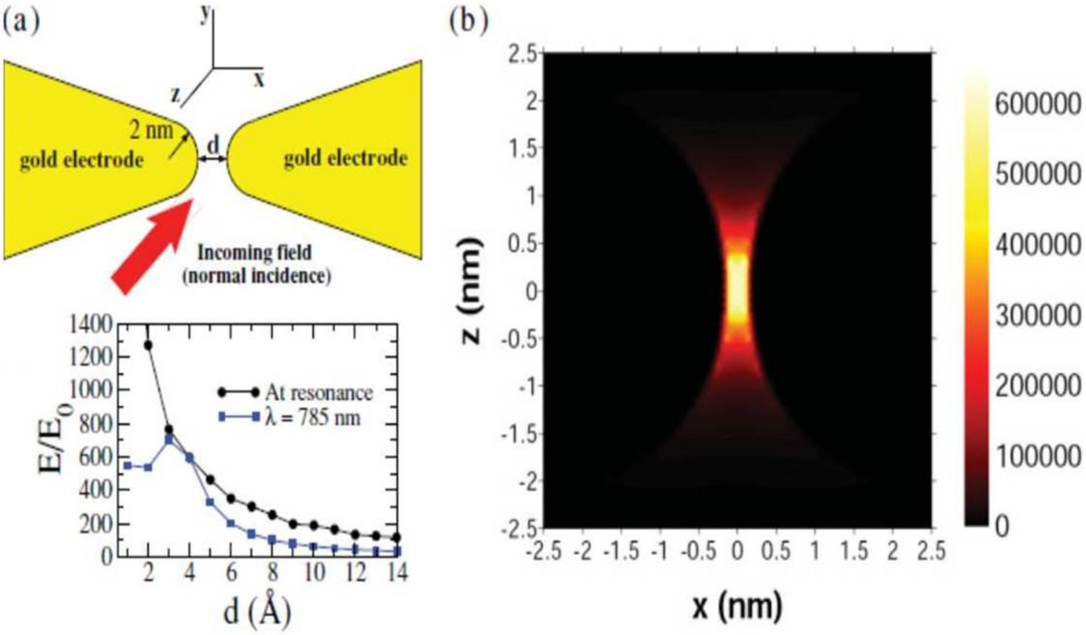

Fig. 2.1.3. (a) Schematic representation of the gold junction considered in the theoretical calculation. Inset in the lower part shows field enhancement in the middle of the gap as a function of the interelectrode distance at resonance and at λ = 785 nm. (b) Spatial distribution of the field intensity (normalized by the incident one) in the *x*-*z* plane for an interelectrode separation *d* = 3Å . The wavelength of the illuminating light is λ = 801 nm. Reprinted with permission from A. García-Martín, D. R. Ward, D. Natelson and J. C. Cuevas, Field enhancement in subnanometer metallic gaps, *Physical Review B*, 2011, 83, 193404.Copyright 2011 American Physical Society.[23]

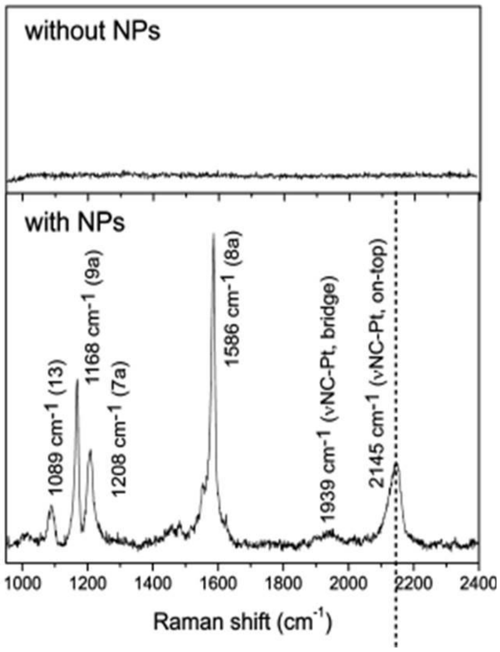

Fig.2.1.4. Raman spectra of CPI-SAM at the Pt(100) facet without (top panel) and with (bottom panel) Au NP adsorption. Reprinted with permission from K. Ikeda, J. Sato, N. Fujimoto, N. Hayazawa, S. Kawata and K. Uosaki, Plasmonic Enhancement of Raman Scattering on Non-SERS-Active Platinum Substrates, *Journal of Physical Chemistry C*, 2009, 113, 11816. Copyright 2009 American Chemical Society.[24]

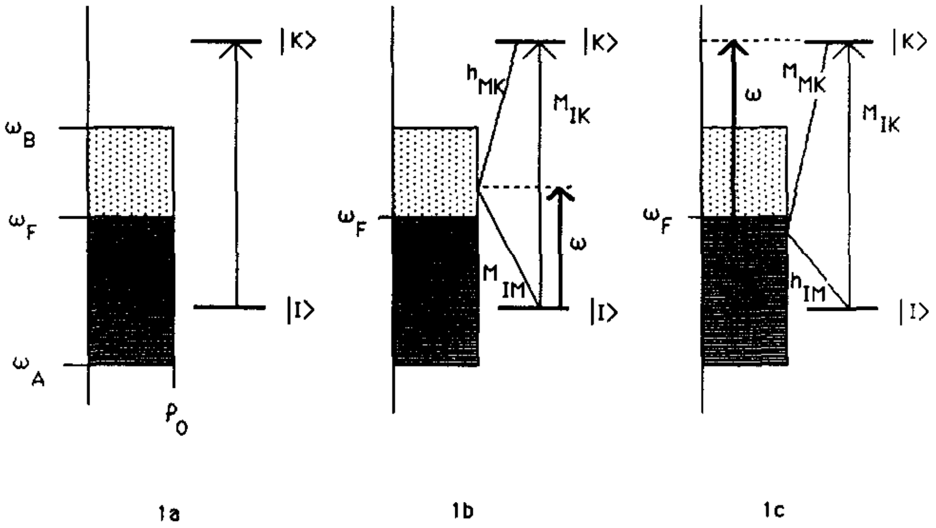

Fig.2.1.5. (a) Energy level scheme for molecule-metal system. The discrete molecular levels are *I* and *K*, between which a transmission is assumed to be allowed. The (continuous) metal levels of the conduction band of the metal are shown on the left. The conduction band ranges between ω_A and ω_B and is assumed to have a constant density of states ρ_0. The filled levels range up to ω_F, the Fermi level, and are depicted by lines, while the unfilled levels are depicted by dots. (b) The scheme for molecule-to-metal charge transfer transitions between the ground molecular state and unfilled levels of the metal. (c) The scheme for metal-to-molecule charge transfer transitions between the ground molecular state and unfilled levels of the metal. Reprinted with permission from J. R. Lombardi, R. L. Birke, T. Lu and J. Xu, *J. Chem. Phys.*, 1986, 84, 4174. Copyright 1986 AIPP. [25]

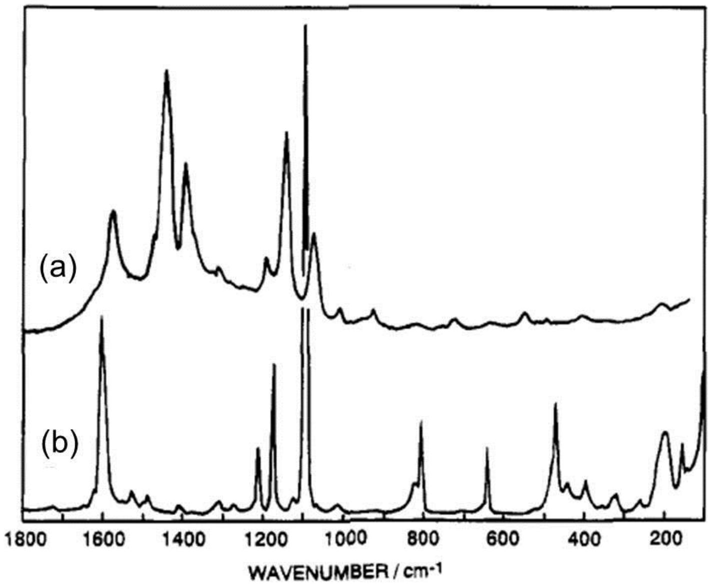

Fig.2.1.6. SERS spectrum of PATP adsorbed on a 8-nm thick silver film evaporated on a CaF_2 plate (a) and normal Raman spectrum of PATP in the solid state (b). Reprinted with permission from M. Osawa, N. Matsuda, K. Yoshii and I. Uchida, Charge Transfer Resonance Raman Process in Surface-Enhanced Raman Scattering from p-Aminothiophenol Adsorbed on Silver: Herzberg-Teller Contribution, *Journal of Physical Chemistry*, 1994, 98, 12702. Copyright 1994 American Chemical Society. [26]

2.2. Conductance measurement as vibrational spectroscopy

In 1966, Lambe and Jaklevic discovered that vibrational spectra can be obtained from molecules adsorbed at the buried metal-oxide interface of a metal-oxide-metal tunneling junction[27]. (Fig.2.2.1. (a)) In their experiment, the tunneling current was measured as a function of the voltage across the junction. Small, but sharp increases in the differential conductance dI/dV were observed when the energy of the tunneling electrons reached the energy of a vibrational mode for molecules in the junction. The increases in the conductance were interpreted as the result of electrons losing their energies to the vibrational mode, giving rise to an inelastic tunneling channel. A peak at each vibrational energy was observed in d^2I/dV^2. (Fig. 2.2.1. (b)) This method (inelastic electron tunneling spectroscopy, IETS) has been applied to a wide range of systems. The technical progress enabled the researchers to perform IETS for single molecules. In 1997, W. Ho *et al*. reported the first study of the vibrational spectra for a single molecule adsorbed on a solid surface[28]. They measured the inelastic electron tunneling spectra for an isolated acetylene (C_2H_2) on Cu (100) using a STM (Scanning Tunneling Microscope) under UHV at 8 K. (Fig. 2.2.2.) IETS also has been applied to molecular junctions. (Fig. 2.2.4.)

IETS is the vibrational spectroscopy based on electron-vibration interaction[3, 29]. When the applied voltage V across a molecular or atomic junction is equal to or higher than the energy of a certain vibration mode ($eV \geq \hbar\omega$, $\hbar\omega$ is the energy of a certain vibration mode.), the mode can be excited by interaction with the conduction electrons. Experimentally, the excitation of vibrational mode can be detected as the abrupt change of conductance in the bias voltage dependence of the differential conductance (dI/dV). Fig.2.2.3. (a) shows the schematic illustration of IETS. In the tunneling regime, the electrons can tunnel elastically when the bias voltage is less than the vibrational energy. Above a threshold voltage, where $eV = \hbar\omega$, an electron can excite a vibrational mode. This means that a second inelastic channel opens, in addition to the elastic channel. The opening of the inelastic channel results in an increase of the differential conductance dI/dV at $eV = \hbar\omega$. This change is observed in the derivative of the differential conductance, where a peak and a dip are observed for the positive and negative biases, respectively.

In addition to IETS, there are the cases in which the excitation of a vibrational mode by the conduction electrons results in the suppression of conductance[3, 29]. This type of spectrum is called point contact spectroscopy (PCS). PCS and IETS are similar measurements of current through the junction as a function of bias voltage. Fig.2.2.3. (b) shows the schematic illustration of PCS. In the contact regime, where the transmission probability is close to one, electrons are delocalized over the two electrodes. We can thus consider the momentum space as shown in Fig.2.2.3. (b). The right-moving electrons occupy higher states than the left-moving electrons when the bias voltage is applied to the junction. Above a threshold voltage, the electron can excite a vibrational mode of the junction, as with the case of the tunneling regime. Electrons around the top of the right-moving states lose energy via excitation of the vibrational mode. Electrons should scatter backwards, because the right-moving states are occupied at a lower energy. This backscattering results in the decrease in the differential conductance at $eV = \hbar\omega$. IETS and PCS are now widely used to analyze the atomic structure for molecular junctions as shown in Fig.2.2.4. and Fig. 1.1.7 (b).[11, 30]

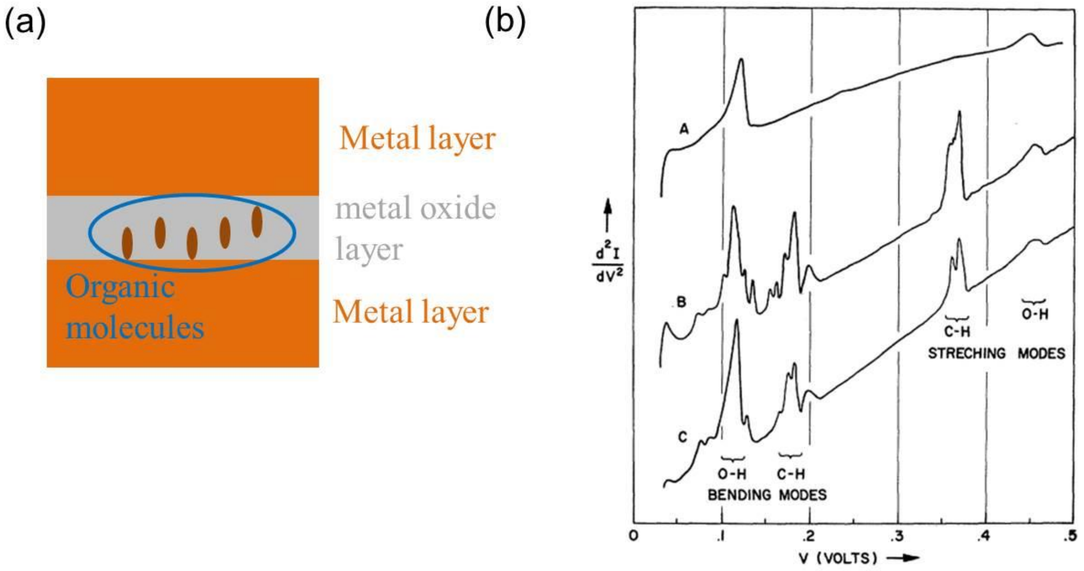

Fig.2.2.1. (a) Schematic view of the metal- oxide-metal tunneling junction which contains organic molecules at the interface of metal and metal oxide. (b) Bias voltage dependence of d^2I/dV^2 of metal-metal oxide-metal structure. A: added no organic molecules, B: added propionic acid molecules, C: added acetic acid molecules. In A, O-H bending mode was observed. Reprinted with permission from R. Jaklevic and J. Lambe, Molecular Vibration Spectra by Electron Tunneling, *Physical Review Letters*, 1966, 17, 1139. Copyright 1966 American Physical Society. [27]

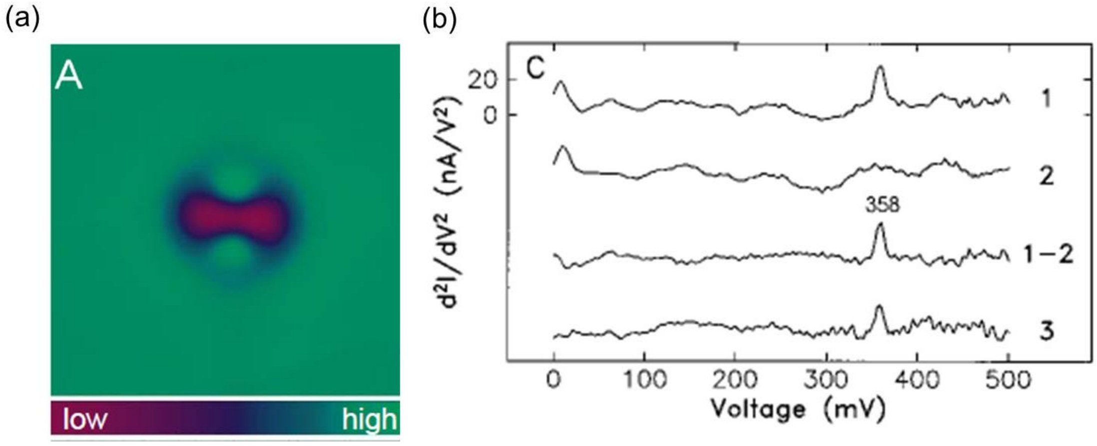

Fig.2.2.2. (a) STM image of a C_2H_2 molecule on the Cu(100) surface at 8 K. Acetylene appears as a dumbbell-shaped depression on the surface with a maximum depth of 0.23 Å. The imaged area, 25 Å by 25 Å, was scanned at a sample bias of 100 mV and tunneling current of 10 nA. (b) d^2I/dV^2 recorded directly over the molecule (1) and over the bare surface (2). The difference spectrum shows a peak at 358 mV. A difference spectrum taken with 2 mV modulation and a different tip (3) shows a smaller peak. Reprinted with permission from B. C. Stipe, M. A. Rezaei and W. Ho, Single-Molecule Vibrational Spectroscopy and Microscopy, *Science*, 1998, 280, 1732. Copyright 1998 AAAS.[28]

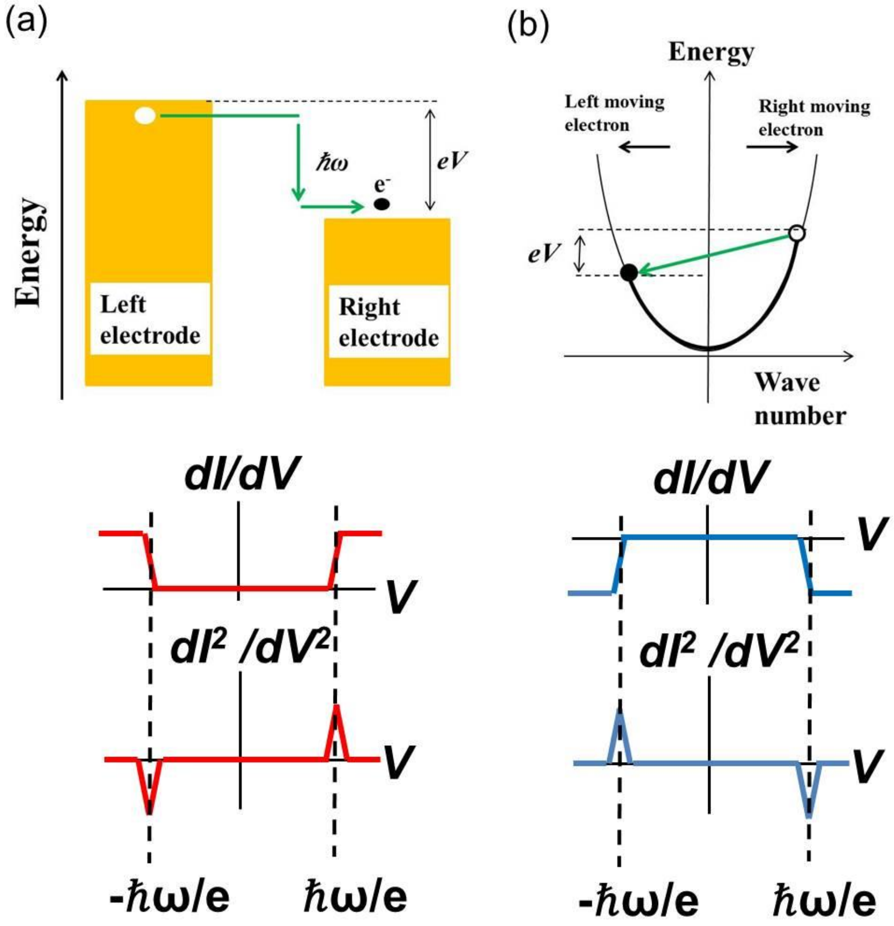

Fig.2.2.3. Schematic view of IETS and PCS, together with dI/dV and d^2I/dV^2. (a) An additional inelastic channel is opened by the excitation of a vibration mode. The conductance (dI/dV) increases above a threshold voltage. (b) The right-moving electrons are scattered backwards by the excitation of a vibrational mode. The conductance decreases above the threshold voltage.

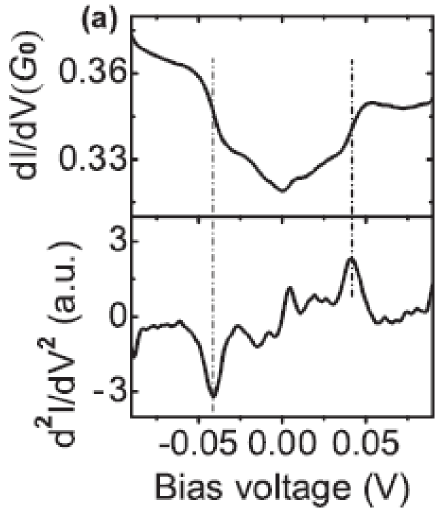

Fig. 2.2.4. Differential conductance (top) and its derivative for a single benzene/Pt junction. Reprinted with permission from M. Kiguchi, O. Tal, S. Wohlthat, F. Pauly, M. Krieger, D. Djukic, J. Cuevas and J. van Ruitenbeek, , *Physical Review Letters*, 2008, 101, 046801.Copyright 2008 American Physical Society. [30]

2.3. IV characteristic

IV characteristic is powerful tool to investigate the electronic structure of the junction[3, 31]. *IV* characteristic of the junction is represented by eq.2-3-1, assuming that the voltage is applied symmetrically between the left and right electrodes. [3]

$$I(V)=\frac{2e}{h}\int_{-\infty}^{\infty}dE\ \tau(E,V)[f_L(E)-f_R(E)]$$

$$=\frac{2e}{h}\int_{-\infty}^{\infty}dE\ \tau(E,V)[f(E-eV/2)-f(E+eV/2)] \qquad \text{2-3-1}$$

where e, h, V, $\tau(E,V)$, $f_{\mathrm{L,R}}(E)$ are the elementary electric charge, Planck's constant, bias voltage, transmission coefficient, and the Fermi function of left and right electrodes, respectively. Assuming that one molecular level (HOMO or LUMO) dominates transport, the transmission function is represented by Lorentzian;

$$\tau(E,V)=\frac{4\Gamma_{\mathrm{L}}\Gamma_{\mathrm{R}}}{[E-\varepsilon_0(V)]^2+[\Gamma_{\mathrm{L}}+\Gamma_{\mathrm{R}}]^2} \qquad \text{2-3-2}$$

where $\varepsilon_0(V)$ and $\Gamma_{\mathrm{L(R)}}$ are the energy of conduction orbital with respect to the Fermi energy (E_{F}) of electrodes, which we set to zero, and strength of the coupling between molecule and left (right) electrodes, respectively. The potential profile of the single BDT molecular junction has been investigated using the theoretical calculation[32, 33]. The voltage drop mainly occurs at the metal-molecule interface. For the asymmetric metal-molecule contacts, more bias voltage drops on the weakly coupled metal-molecule contact and less potential drops on the strongly coupled metal-molecule contact. The voltage-induced molecular level shifting can be, thus, roughly represented by Eq. 2-3-3[31].

$$\varepsilon_0(V)=\varepsilon_0+\frac{eV}{2}\frac{\Gamma_L-\Gamma_R}{\Gamma_L+\Gamma_R} \qquad \text{2-3-3}$$

The exact IV characteristics can be obtained by solving Eq. 2-3-1.At 0 K, I(V) can be represented by

$$I(V)=\frac{8e}{h}\frac{\Gamma_{\mathrm{L}}\Gamma_{\mathrm{R}}}{\Gamma_{\mathrm{L}}+\Gamma_{\mathrm{R}}}\left\{\tan^{-1}\left(\frac{\frac{\Gamma_{\mathrm{R}}}{\Gamma_{\mathrm{L}}+\Gamma_{\mathrm{R}}}\mathrm{eV}-\varepsilon_0}{\Gamma_{\mathrm{L}}+\Gamma_{\mathrm{R}}}\right)+\tan^{-1}\left(\frac{\frac{\Gamma_{\mathrm{L}}}{\Gamma_{\mathrm{L}}+\Gamma_{\mathrm{R}}}\mathrm{eV}+\varepsilon_0}{\Gamma_{\mathrm{L}}+\Gamma_{\mathrm{R}}}\right)\right\} \qquad \text{2-3-4}$$

However, the Fermi distribution function is not a step function at temperatures higher than 0 K[3]. Then, following Sommerfeld expansion (Eq. 2-3-5) can be used to solve eq.

2-3-1.

$$\int_0^{\infty} g(E)\,f(E)dE = \int_0^{\mu} g(E)dE + \frac{\pi^2}{6}(kT)^2 g'(\mu) + \cdots \quad , \quad \text{2-3-5}$$

where μ, $g(E)$, $g'(\mu)$, k and T are the chemical potential, energy-dependent function, first derivative of $g(E)$ at $E=\mu$, Boltzmann constant and temperature, respectively. $I(V)$ can be represented by

$$I(V) = \frac{8e}{h}\frac{\Gamma_{\mathrm{L}}\Gamma_{\mathrm{R}}}{\Gamma_{\mathrm{L}}+\Gamma_{\mathrm{R}}}\left\{\tan^{-1}\left(\frac{\frac{\Gamma_{\mathrm{R}}}{\Gamma_{\mathrm{L}}+\Gamma_{\mathrm{R}}}\mathrm{eV}-\varepsilon_0}{\Gamma_{\mathrm{L}}+\Gamma_{\mathrm{R}}}\right)+\tan^{-1}\left(\frac{\frac{\Gamma_{\mathrm{L}}}{\Gamma_{\mathrm{L}}+\Gamma_{\mathrm{R}}}\mathrm{eV}+\varepsilon_0}{\Gamma_{\mathrm{L}}+\Gamma_{\mathrm{R}}}\right)\right\}$$

$$-\frac{8\pi^2}{3h}e(kT)^2\Gamma_{\mathrm{L}}\Gamma_{\mathrm{R}}\left[\frac{\frac{\Gamma_{\mathrm{R}}}{\Gamma_{\mathrm{L}}+\Gamma_{\mathrm{R}}}\mathrm{eV}-\varepsilon_0}{\left\{\left(\frac{\Gamma_{\mathrm{R}}}{\Gamma_{\mathrm{L}}+\Gamma_{\mathrm{R}}}\mathrm{eV}-\varepsilon_0\right)^2+\left(\Gamma_{\mathrm{L}}+\Gamma_{\mathrm{R}}\right)^2\right\}^2}+\frac{\frac{\Gamma_{\mathrm{L}}}{\Gamma_{\mathrm{L}}+\Gamma_{\mathrm{R}}}\mathrm{eV}+\varepsilon_0}{\left\{\left(\frac{\Gamma_{\mathrm{L}}}{\Gamma_{\mathrm{L}}+\Gamma_{\mathrm{R}}}\mathrm{eV}+\varepsilon_0\right)^2+\left(\Gamma_{\mathrm{L}}+\Gamma_{\mathrm{R}}\right)^2\right\}^2}\right]$$

2-3-6

where μ = E_{F} + $eV/2$ for the left electrode and E_{F} – $eV/2$ for the right electrode, respectively. The eq. 2-3-6 was used to evaluate ε_0 and $\Gamma_{\mathrm{L(R)}}$ by fitting the IV curve obtained in the experiment in Chapter.3. It should be noted that we can evaluate only the absolute value of ε_0 because of the symmetry of the functions in these equations. It is necessary to perform the other analysis such as thermopower measurement to clarify the sign of the ε_0, i.e. whether the conduction orbital is above or below the Fermi level.

2.4. Thermopower measurement

There is the phenomenon named thermoelectric effect or Seebeck effect in which voltage is induced when the temperature gradient is established in a material[34]. The voltage is called thermoelectric voltage. The thermoelectric voltage ΔV is proportional to the temperature gradient ΔT as follows.

$$\Delta V = S\,\Delta T \cdots \quad 2\text{-}4\text{-}1$$

S is called thermopower or Seebeck coefficient. This effect was discovered by Thomas Johann Seebeck in 1821. The thermoelectric effect has attracted wide attention because thermoelectric devices enable efficient energy conversion of waste heat into electrical energy. On the other hand, thermoelectric effect can be used to analyze the electronic structure. The sign of the thermopower can determine which charge carriers (electron or hole) dominate the electric transport in metals and semiconductors. In the following, thermoelectric effect is explained.

Fig. 2.4.1. illustrates the electric circuit for the measurement of thermopower. Material a is measuring object. Material b is used as lead. As mentioned above, temperature gradient ∇T induces voltage (or electric field) in materials. The measured thermoelectric voltage ΔV is described by[35]

$$\begin{aligned}
\Delta V &= \int_1^2 (-\boldsymbol{E}) \cdot d\boldsymbol{r} + \int_2^3 (-\boldsymbol{E}) \cdot d\boldsymbol{r} + \int_3^4 (-\boldsymbol{E}) \cdot d\boldsymbol{r} \\
&= \int_1^2 (-S_b)\, \nabla T \cdot d\boldsymbol{r} + \int_2^3 (-S_a) \cdot \nabla T \cdot d\boldsymbol{r} + \int_3^4 (-S_b) \cdot \nabla T \cdot d\boldsymbol{r} \\
&= \int_{T_0}^{T} (-S_b)\, \mathrm{d}T + \int_T^{T+\Delta T} (-S_a)\, dT + \int_{T+\Delta T}^{T_0} (-S_b)\, dT \\
&= \int_T^{T+\Delta T} (S_b - S_a)\, dT \\
&\cong (S_b - S_a)\Delta T \cdots \quad 2\text{-}4\text{-}2
\end{aligned}$$

where S_a and S_b are values of **absolute** thermopower of material a and b, respectively.

From eq.2-4-2, it can be said that

1) absolute thermopower (S_a) cannot be measured.

2) only **relative** thermopower (= S_b - S_a) can be measured.

For the estimation of the absolute thermopower, it is necessary to use the material of lead whose thermopower (S_b) is known. The thermoelectric effect has two contributions, such that $S = S_e + S_{ph}$. The term S_e has its origin in the diffusion of the electrons in the presence of a temperature gradient. The other term, S_{ph}, is due to the non-equilibrium distribution of the phonon, which drags the electrons. Only the contribution from the diffusion of the electrons will be discussed in the following.[3]

The thermopower of the atomic and molecular junction is represented by

$$S = -L_1(T)/eTL_0(T) \cdots \quad 2\text{-}4\text{-}3$$

$$L_n(T) = \int dE\left(-\frac{\partial f}{\partial E}\right)(E - E_F)^n \tau(E) \cdots \quad 2\text{-}4\text{-}4$$

where, e, T, f, $\tau(E)$, and E_F are electron charge, temperature, Fermi distribution function, transmission curve, and Fermi level, respectively. The thermopower of the atomic and molecular junction depends on the shape of the transmission curve and Fermi distribution function, which depend on the atomic configuration of the junction and temperature, respectively. By using Sommerfeld expansion, the following expression is obtained.

$$S = -\frac{\pi^2 k_B{}^2 T}{3e}\frac{\partial ln\tau(E)}{\partial E}|_{E=E_F} \cdots \quad (2\text{-}4\text{-}5)$$

Approximately, thermopower provides the information about the shape (slope) of the transmission curve at Fermi level. (Fig. 2.4.2.)

In 1999, Ludoph and Ruitenbeek reported the first thermopower measurements in gold atomic junctions.[36] Thermoelectric voltage was measured simultaneously with the conductance. In the experiment, thermopower jumped to new values simultaneously with the jumps in the conductance. Even tiny jumps or changes of slope of the conductance can be accompanied by large steps in the thermopower. The thermopower of the junction can have both a positive or negative sign. (Fig. 2.4.3.) In 2007, Reddy *et al*. reported the first thermopower measurement in molecular junctions.[37] They measured the thermopower of 1,4-benzenduthiol (BDT), 4,4'-dibenzendithiol (DBDT), 4,4"-tribenzenedithiol (TBDT) in contact with gold at room temperature and found the values of +8.7 ± 2.1 μV/K, +12.9± 2.2 μV/K, +14.2 ± 3.2 μV/K, respectively. The positive sign was thought to be originated from the p-type (hole) conduction in these junctions. In other words, the transport was thought to be dominated by the HOMO of the molecules. (Fig. 2.4.4.) In addition to the experiments, thermoelectric effect in atomic/molecular junction has been studied widely in terms of the theoretical calculation. Nakamura *et al*. actually demonstrated the significant temperature dependence of the thermopower, for the single organometallic complex wire, using a theoretical calculation.[38] The thermopower monotonically decreases with temperature and its sign changes from positive to negative at 220 K. This distinct sign change is caused by the existence of many molecular orbitals, near the Fermi level. (Fig. 2.4.5.) Dubi reported a theoretical study of the thermopower of single-molecule junctions with focus on phenylbased molecular junctions.[39] In this study, thermal fluctuations of the torsional angle between the phenyl rings and variations in the position of the molecular level alignment with respect to the electrode Fermi energy were taken into account. They found that at large molecular orbital variations, the thermopower becomes strongly dependent on the torsion angle and can even change sign. This study indicates that the theropower of the molecular junction is sensitive to the atomic structure. Now thermoelectric effect in atomic and molecular junctions are widely studied in terms of the analysis of electronic structure and energy harvesting. [40]

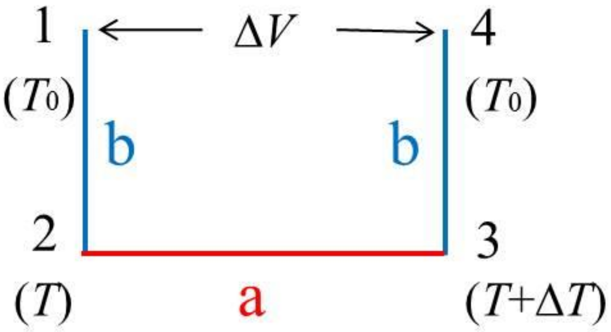

Fig. 2.4.1. Electric circuit for the measurement of thermopower. ΔV is measured thermoelectric voltage. T_0, T, $T+\Delta T$ are temperatures at 1(4), 2, and 3, respectively.

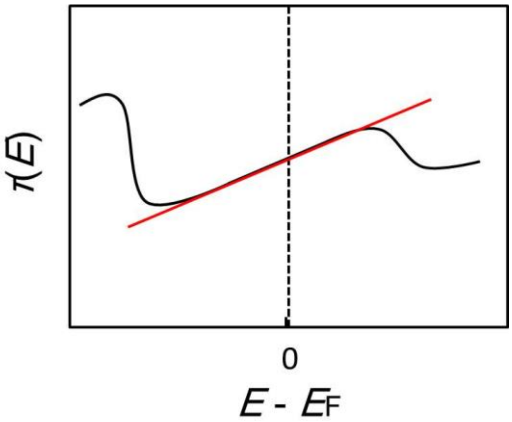

Fig. 2.4.2. Schematic illustration of the energy dependent transmission curve $\tau(E)$. Approximately, thermopower provide the slope of the $\tau(E)$ at Fermi level. (red solid line)

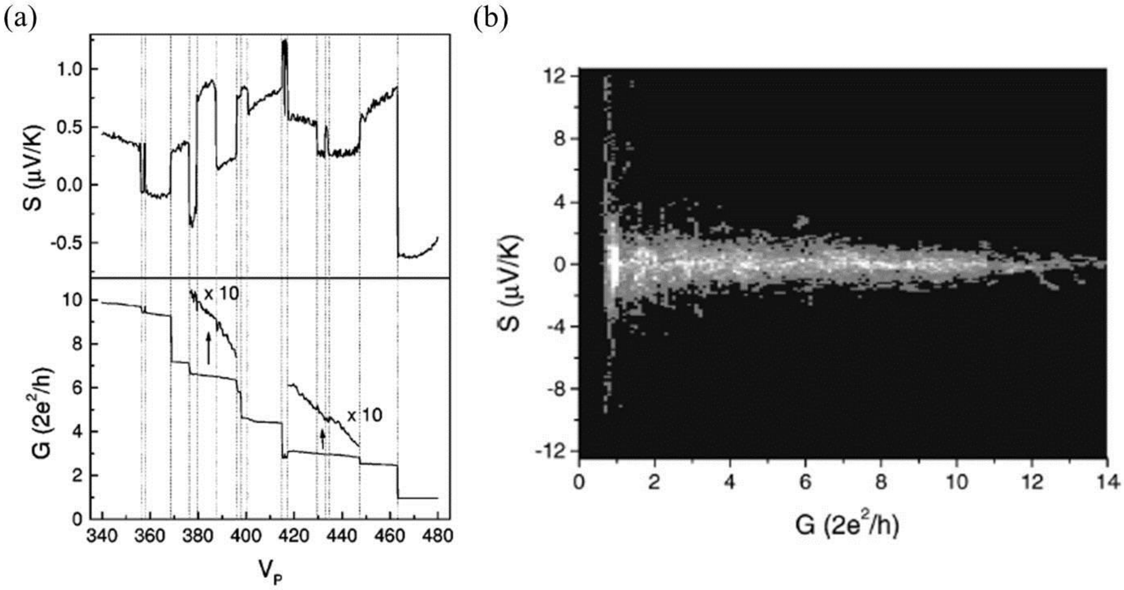

Fig.2.4.3. (a) Conductance G and thermopower S change in the breaking process of the gold wire. The vertical gray lines indicate the corresponding steps in the conductance and thermopower. (b) Density plot of thermopower against conductance: The thermopower axis is divided into 0.125 μV/K, and the conductance into $0.1G_0$ sections, creating 0.125 μV/K by $0.1G_0$ bins. The occurrence of a particular combination of conductance and S is added to its corresponding bin, and the sum of 220 curves for the two samples is plotted in gray scale above. Black represents no data points and white more than 100. Reprinted with permission from B. Ludoph and J. M. v. Ruitenbeek, Thermopower of atomic-size metallic contacts, *Physical Review B*, 1999, 59, 12290. Copyright 1999 American Physical Society. [36]

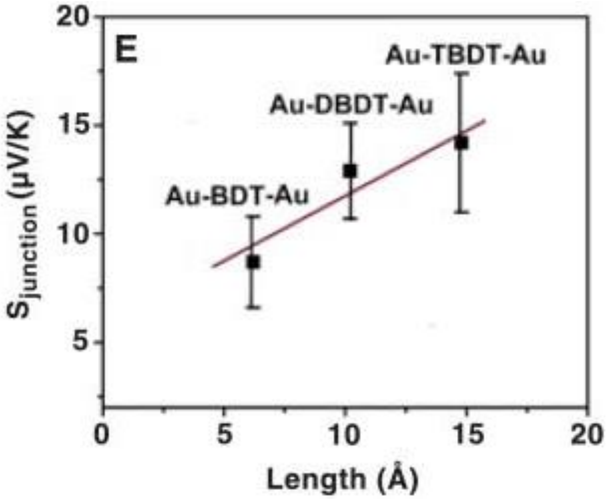

Fig.2.4.4. Plot of measured junction thermopower as a function of molecular length for BDT, DBDT, and TBDT. Reprinted with permission from P. Reddy, S. Y. Jang, R. A. Segalman and A. Majumdar, Thermoelectricity in Molecular Junctions, *Science*, 2007, 315, 1568-1571. Copyright 2007 AAAS.[37]

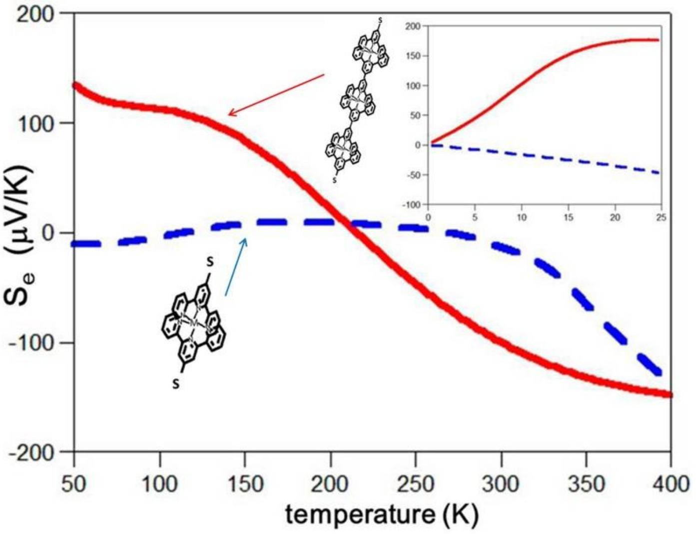

Fig.2.4.5. Plots of the thermopower (S_e) of Ru1L (red) and Ru3L (blue) as functions of temperature in the 50−400 K range. The molecular structures of Ru1L and Ru3L are shown in the graph. Inset: Plots in the temperature zone below 25 K. Adapted with permission from H. Nakamura, T. Ohto, T. Ishida and Y. Asai, Thermoelectric Efficiency of Organometallic Complex Wires via Quantum Resonance Effect and Long-Range Electric Transport Property, *Journal of the American Chemical Society*, 2013, 135, 16545.Copyright 2013 American Chemical Society.[38]

3, Analysis of atomic structure for 1,4-benzenedithiol molecule bridging between Au electrodes by surface enhanced Raman spectroscopy

3.1. Introduction

Raman spectroscopy has been utilized to the molecular junction, because surface enhanced Raman scattering (SERS) offers a single-molecule sensitivity[20]. The strong electric field formed between the nano gap electrodes enhances the intensity of Raman signal, and thus, Raman spectrum from the molecule in the nano gap is selectively observed. Tian *et al.* observed the increase in the SERS intensity of molecules in the nano gap with decreasing the gap size using mechanically controllable break junction method (MCBJ).[41] Liu *et al.* observed the splitting of the Raman peak, and the peak energy shift by applying the bias voltage to the single molecular junction.[42] Ioffe *et al.* succeeded in evaluating the effective temperature of the molecular junction by measuring both the Stokes and anti-Stokes components of the Raman scattering.[43] Ward *et al.* and Konishi *et al.* succeeded in the simultaneous conductance and SERS measurement of the single molecular junction.[16, 17] They observed the appearance of the b_2 modes for the molecular junctions, which were not observed in the bulk crystal. While the combination of SERS and conductance measurement of the molecular junctions is a powerful technique to characterize the molecular junction, there are several subjects. First, most previously reported experimental measurements have been limited to the conductance near zero bias, the current–voltage (IV) characteristics of the molecular junctions must be determined in order to study the junctions in detail.[44-46] The IV characteristics provide the information about the electronic structure of the molecular junctions, such as the energy difference between conduction orbital and Fermi level, and strength of the metal-molecule coupling. Second, the Raman signals which are characteristic of the molecular junction have not been fully understood. For some molecular junctions, b_2 modes have been observed, while they are not observed in the bulk crystal.[16, 17] The origin of the appearance of the b_2 mode is not fixed yet.

In the present study, the IV characteristics and SERS of the 1,4-benzendithiol molecular junction have been investigated using the stable fixed planar nanogap electrodes (gap size ≈ 1 nm). The IV characteristics revealed the number of molecules bridging metal electrodes, energy difference between the conduction orbital and Fermi level, and the strength of metal-molecule coupling. The conductance measurements confirmed the molecular bridge between Au electrodes. The SERS measurement showed the disappearance of the SH modes and red shift of internal vibration modes, which confirmed the molecular bridge between Au electrodes. For some molecular junctions, I observed the b_2 mode, which was not observed in the bulk crystal. The appearance of the b_2 mode could be explained by the photon-driven charge transfer between molecule and metal electrodes (CM effect).[47]

3.2. Experimental

To perform the SERS measurement of 1,4-benzenedithiol molecule bridging between Au electrodes, the nanogap electrodes shown in Fig.3.2.1. (a) were utilized. Fig. 3.2.1.(b) shows the scanning electron microscope (SEM) images of the Au nanogap electrode. Fig.3.2.2. shows the illustration of the procedure to fabricate the nanogap electrodes. The fixed planar nanogap electrodes were fabricated on Si wafer with 300 nm of thermal oxide, using oblique metal evaporation with a shadow mask, followed by an electromigration technique. To adjust the gap size of the electrodes, electromigration was used. Electromigration is forced atomic diffusion with the driving force due to an electric field and associated electric current in metals. Experimentally, the structural change is induced by applying the bias voltage. The structural change results in the abrupt change of the electric current. (Fig.3.2.3. (a)) Fig.3.2.3. (b) shows the *IV* characteristics before and after the electromigration.

To estimate the gap size, eq.3-2-1. was used. Eq.3-2-1 was proposed by the J. Simmons to analyze the IV characteristic of the electrodes separated by a thin insulating film.[48]

$$
\begin{aligned}
I(V) = {} & A \times 6.17 \times 10^{-10} \times \frac{1}{s^{2}} \times \\
& \left\{ \left(U - \frac{V}{2} \right) \exp\left(-1.025 \times 10^{-10} \times s \times \sqrt{\mathrm{U} - \frac{\mathrm{V}}{2}} \right) - \right. \\
& \left. \left(U + \frac{V}{2} \right) \exp\left(-1.025 \times 10^{-10} \times s \times \sqrt{\mathrm{U} + \frac{\mathrm{V}}{2}} \right) \right\}
\end{aligned}
\qquad (3\text{-}2\text{-}1)
$$

Here, *s*, *A*, and *U* are gap size, area, and work function, respectively.

To estimate the IV characteristic of the system in which the barrier height is not constant (Fig.3.2.4. (a)), J. Simmons proposed to use the mean barrier height instead (Fig.3.2.4. (b)). By using the rectangular potential barrier, eq.3-2-1 was obtained. The gap size was estimated by fitting the IV characteristic after the electromigration with eq. 3-2-1.(Fig. 3.2.5.) The gap size was adjusted to ~ 1 nm.

Fig. 3.2.6. shows the schematic view of the electronic and SERS measurements. The Au nanogap electrodes were immersed in a 1 mM 1, 4-benzendithiol ethanol solution at room temperature for 10 minutes. After removal of the solution, IV characteristics were

measured before and after the SERS measurements at room temperature using an source meter (Keithley 2612A). The bias voltage was not applied between nanogap electrodes during the SERS measurements. The SERS measurements were performed using commercial Raman microprobe spectrometer with 4 s integrations (Nanofinder30, Tokyo Instruments). Near-infrared (NIR) laser light (λ_{ex} = 785 nm, 70 mW) was used as excitation light. The NIR beam was focused onto the sample using an objective lens with 100× magnification and a numerical aperture of 0.95. The estimated spot size of irradiation was about 1 μm.

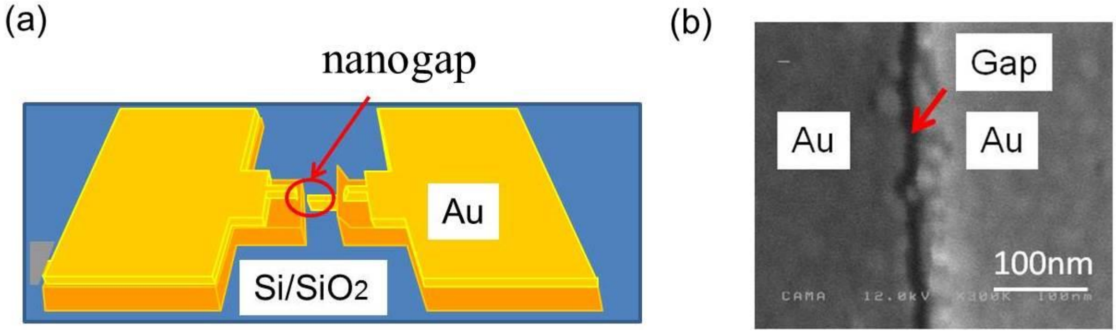

Fig.3.2.1. (a) Schematic view of the nanogap electrode. (b) SEM image of the nanogap electrode. Reprinted with permission from R. Matsuhita, M. Horikawa, Y. Naitoh, H. Nakamura and M. Kiguchi, Conductance and SERS Measurement of Benzenedithiol Molecules Bridging Between Au Electrodes, *The Journal of Physical Chemistry C*, 2013, 117, 1791. Copyright 2013 American Chemical Society.[47]

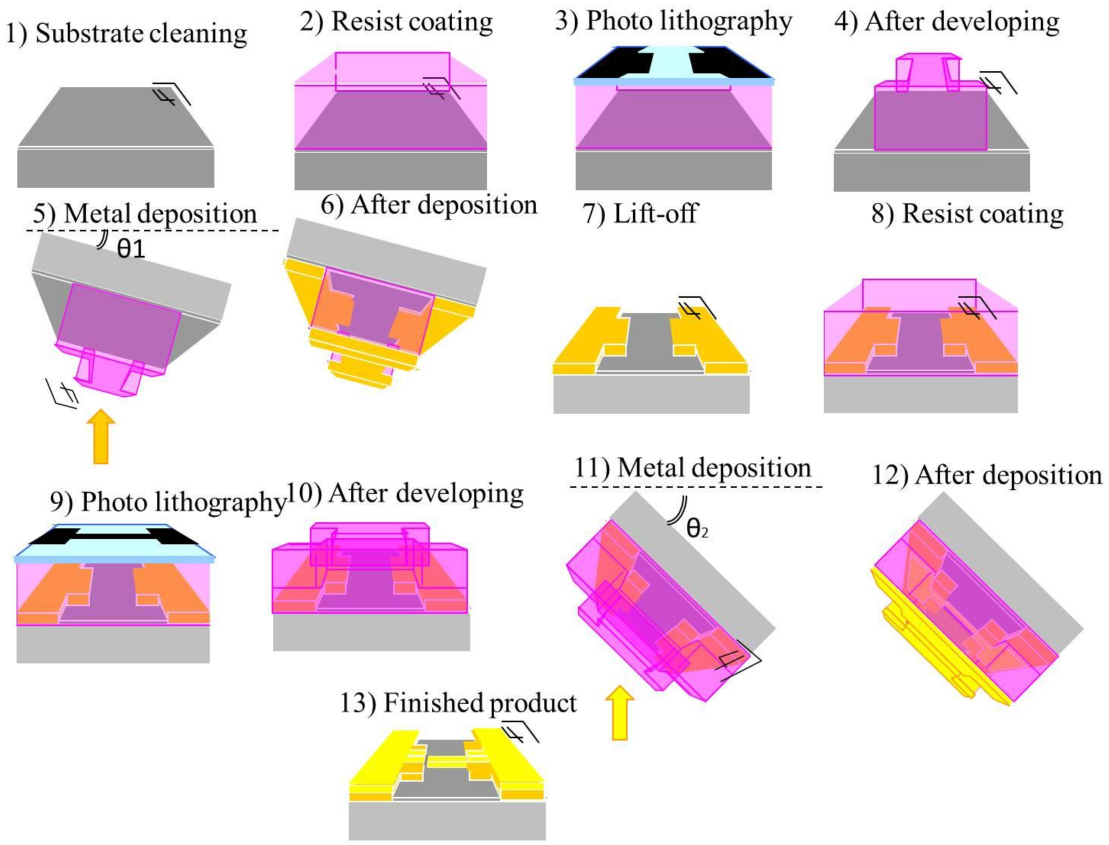

Fig.3.2.2. Procedure to fabricate the nanogap electrodes.

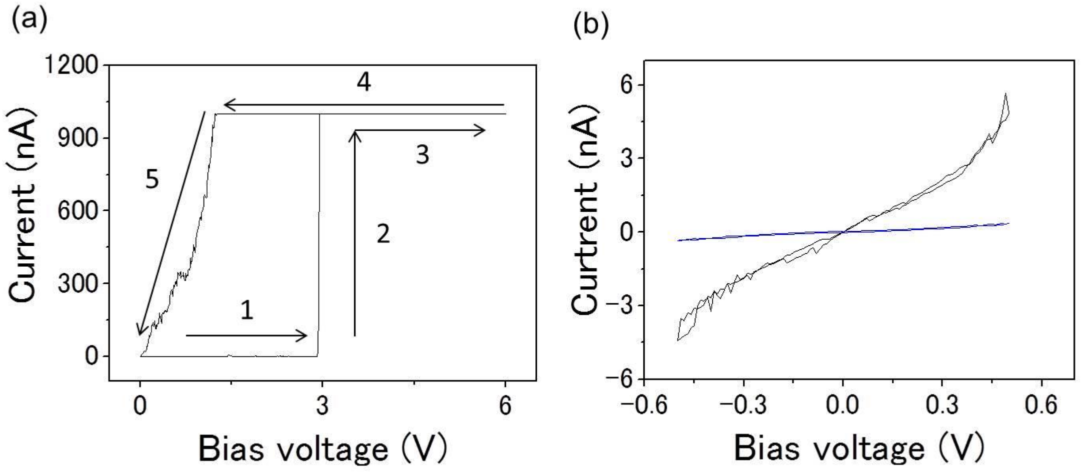

Fig.3.2.3. (a) IV characteristic in the electromigration. The numbers and the black arrows represent the order of change of electric current. The abrupt change of the current corresponds to the structural change of the nanogap. (b) IV characteristics before (blue) and after (black) the electromigration, respectively.

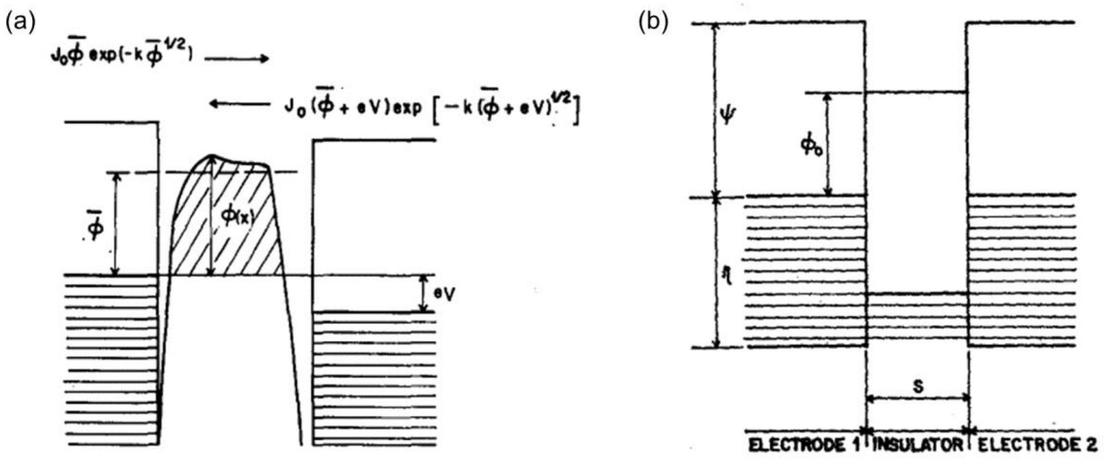

Fig.3.2.4. (a) General barrier in insulating film between two metal electrodes. $\bar{\phi}$ is the mean barrier height. (b) Rectangular potential barrier in insulating film between metal electrodes. Reprinted with permission from J. G. Simmons, Generalized Formula for the Electric Tunnel Effect between Similar Electrodes Separated by a Thin Insulating Film, *Journal of Applied Physics*, 1963, 34, 1793.Copyright 1963 AIPP.[48]

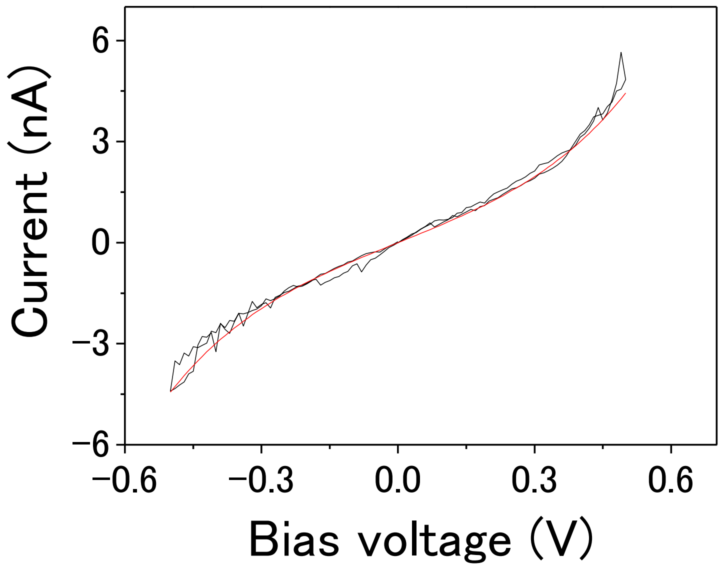

Fig.3.2.5. *IV* characteristic after the electromigration (Black). Red curve is the fitting result with eq.3-2-1. From the fitting result, the gap size was estimated to be 1.0 nm.

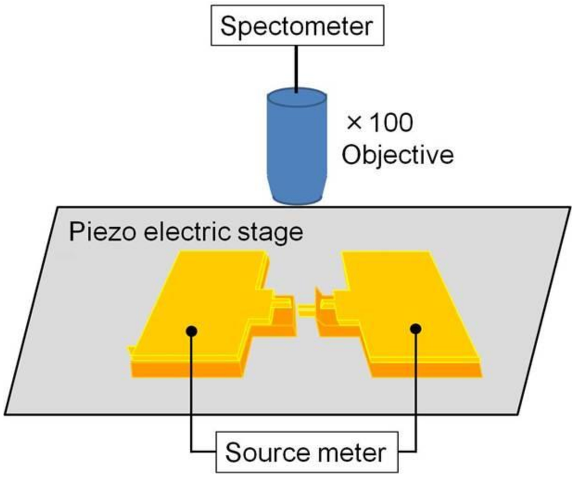

Fig3.2.6. Schematic view of the electronic and SERS measurements. Reprinted with permission from R. Matsuhita, M. Horikawa, Y. Naitoh, H. Nakamura and M. Kiguchi, Conductance and SERS Measurement of Benzenedithiol Molecules Bridging Between Au Electrodes, *The Journal of Physical Chemistry C*, 2013, 117, 1791. Copyright 2013 American Chemical Society.[47]

3.3. Results and discussion

Fig.3.3.1. (c) shows the examples of Raman spectra of underlying Si (A), the Au nanogap (B), and Au electrode (C). Strong band was observed around 520 cm^{-1}, corresponding to the underlying Si substrate. No features were observed in the Raman spectrum on the flat Au electrode. At the nano gap, intense bands were observed at 520, 1068, 1561cm^{-1}, which were assigned to the Si band, C-C stretching and C=C stretching modes, respectively. Fig.3.3.1.(b) shows the map of BDT SERS signal from the a_1 symmetry mode at 1561cm^{-1} (integrated from 1500 to 1620cm^{-1}). The SERS signal was enhanced around the nanogap region. In the absence of BDT molecules, intensity of the Raman signal was under the detection limit, which proved that the observed Raman signal was solely due to the BDT molecules in the gap, and not due to the bare Au nanogap electrodes or other contaminants.

Fig.3.3.2.(a) shows the IV characteristics of the molecular junction before and after the SERS measurement. The IV characteristics did not change with time, showing that the molecular junction had a high stability. The conductance of the molecular junction was obtained by numerical differentiation of the current with a voltage value of around zero in the voltage regime. The conductance was $9.6 \times 10^{-3}\ G_0$ for the molecular junction shown in Fig. 3.3.2.(a,b). The conductance of the single BDT molecular junction could be obtained by constructing the conductance histogram with break junction technique.[14] By comparing the conductance value with that of the single molecular junction, the number of molecules bridging the Au electrodes was determined to be one for the molecular junction shown in Fig. 3.3.2.(a,b). The average number of molecules bridging Au electrodes was around 30 by evaluating 36 samples. Here, it is noteworthy that the conductance of the molecular junction is affected by the surrounding molecules. Previously reported theoretical study showed that the conductance of the single molecule, where the molecule was surrounded by molecules, was up to five times higher than that of the isolated single molecule junction[49]. The conductance of the single molecule junction also varies with the metal-molecule contact configuration, bias voltage, environment, and other conditions[50]. I roughly evaluated the number of molecules bridging Au electrodes in the present study.

The IV characteristic was investigated based on the single level tunneling model (eq.

2-3-4).[1,5] At 0 K, IV characteristic of the molecular junction is represented by

$$I(V)=\frac{8e}{h}\frac{\Gamma_{\mathrm{L}}\Gamma_{\mathrm{R}}}{\Gamma_{\mathrm{L}}+\Gamma_{\mathrm{R}}}\left\{\tan^{-1}\left(\frac{\frac{\Gamma_{\mathrm{R}}}{\Gamma_{\mathrm{L}}+\Gamma_{\mathrm{R}}}\mathrm{eV}-\varepsilon_0}{\Gamma_{\mathrm{L}}+\Gamma_{\mathrm{R}}}\right)+\tan^{-1}\left(\frac{\frac{\Gamma_{\mathrm{L}}}{\Gamma_{\mathrm{L}}+\Gamma_{\mathrm{R}}}\mathrm{eV}+\varepsilon_0}{\Gamma_{\mathrm{L}}+\Gamma_{\mathrm{R}}}\right)\right\} \tag{3-3-1}$$

where ε_0, Γ_{L} and Γ_{R} are the energy of the conduction orbital, and the strength of the coupling between molecule and left and right electrodes, respectively. At finite temperature, it is necessary to take into account that the Fermi distribution function gets smeared out. IV characteristic of the molecular junction at finite temperature T can be represented by

$$I(V)=\frac{8e}{h}\frac{\Gamma_{\mathrm{L}}\Gamma_{\mathrm{R}}}{\Gamma_{\mathrm{L}}+\Gamma_{\mathrm{R}}}\left\{\tan^{-1}\left(\frac{\frac{\Gamma_{\mathrm{R}}}{\Gamma_{\mathrm{L}}+\Gamma_{\mathrm{R}}}\mathrm{eV}-\varepsilon_0}{\Gamma_{\mathrm{L}}+\Gamma_{\mathrm{R}}}\right)+\tan^{-1}\left(\frac{\frac{\Gamma_{\mathrm{L}}}{\Gamma_{\mathrm{L}}+\Gamma_{\mathrm{R}}}\mathrm{eV}+\varepsilon_0}{\Gamma_{\mathrm{L}}+\Gamma_{\mathrm{R}}}\right)\right\}$$

$$-\frac{8\pi^2}{3h}e(kT)^2\Gamma_{\mathrm{L}}\Gamma_{\mathrm{R}}\left[\frac{\frac{\Gamma_{\mathrm{R}}}{\Gamma_{\mathrm{L}}+\Gamma_{\mathrm{R}}}\mathrm{eV}-\varepsilon_0}{\left\{\left(\frac{\Gamma_{\mathrm{R}}}{\Gamma_{\mathrm{L}}+\Gamma_{\mathrm{R}}}\mathrm{eV}-\varepsilon_0\right)^2+(\Gamma_{\mathrm{L}}+\Gamma_{\mathrm{R}})^2\right\}^2}+\frac{\frac{\Gamma_{\mathrm{L}}}{\Gamma_{\mathrm{L}}+\Gamma_{\mathrm{R}}}\mathrm{eV}+\varepsilon_0}{\left\{\left(\frac{\Gamma_{\mathrm{L}}}{\Gamma_{\mathrm{L}}+\Gamma_{\mathrm{R}}}\mathrm{eV}+\varepsilon_0\right)^2+(\Gamma_{\mathrm{L}}+\Gamma_{\mathrm{R}})^2\right\}^2}\right]$$

3-3-2

The first term is the same as eq. 3-3-1, and the second term is the correction term caused by the finite temperature. By fitting the experimental result with eq. 3-3-2, the Γ_{L}, Γ_{R}, and ε_0 were determined to be 0.030 eV, 0.033 eV, and 0.63 eV, respectively. In order to accurately determine ε_0, 26 samples were investigated, resulting in the ε_0 histogram presented in Fig. 3.3.2.(c). The histogram shows a well-defined peak at 0.61 eV with 0.08 eV width. The average and standard deviation of ε_0 were 0.59 eV and 0.11 eV, respectively. The energy difference between conduction orbital and Fermi level was 0.6 (±0.1) eV for the BDT molecular junction in the present study. The finite strength of the coupling (~10 meV on average) suggested the binding of the BDT molecule to Au electrodes and interaction between them. In the present study, I took into account that the Fermi distribution function got smeared out for finite temperature. The temperature correction term was about several % of the first term at 300 K.

The conductance measurement confirmed the bridging of BDT molecule between Au electrodes. Then the Raman spectra of the molecular junction were investigated. Fig.3.3.3. shows the typical SERS spectra of BDT molecular junction. In most of spectra, C-C and C=C stretching modes were observed. (Fig. 3.3.4.) Sometimes, we observed modes around 1400 cm^{-1} (upper 2 spectra) for 8 distinct samples. Here, it is noteworthy that the SH modes (908, 2556cm^{-1}) were not observed in the BDT molecular junction.[34] The absence of the SH modes indicated that the S-H bonds were broken and BDT molecule bound to both Au electrodes. The SH modes would be observed when the BDT molecule binds to one of the Au electrode and other SH anchoring group is free (Fig. 3.3.5. ~ 3.3.6.). The present SERS result supported the formation of the molecular junction.

I then discuss the peak shift of the vibration mode of the molecular junction. On average, the C=C (C-C) stretching mode was observed at 1562cm^{-1} (1063 cm^{-1}) for the molecular junction, while it was observed at 1572cm^{-1} (1094 cm^{-1}) in the bulk crystal. The C=C and C-C stretching modes showed the red-shift. When the molecule adsorbs on metal surface, the bonding orbitals are formed by the interaction between HOMO of molecule and unoccupied state of metal, and between LUMO and occupied state of metal. Electron transfers from HOMO (bonding orbital) to metal state, and electron transfers from metal to LUMO (anti-bonding)[1]. Therefore, the interaction between molecule and metal leads to the decrease in the bond strength of the molecule. The red-shift of C=C and C-C stretching modes is originated from the interaction between BDT molecule and metal electrode, which confirms the bridging of BDT molecule between Au electrodes. The changes of vibrational energy by electron transfer are also observed for the hexa-carbonyl complex system[51]. (Table 3.3.1.)

I then discuss the appearance of 1400 cm^{-1} peak (b_2 mode) based on the Lombardi's model explained above in Chapter 2.1.[25] According to this model, Raman tensor elements are represented as α=A+B+C. Term A represents a Frank-Condon contribution, and B and C terms represent Herzberg-Teller contributions. Term B and C correspond to molecule-to-metal and metal-to-molecule charge transfer transitions, respectively. Totally symmetric modes can be enhanced by all three terms, while non-totally symmetric modes can be enhanced via the terms B and C. When I assume that B term (molecule-to-metal charge transfer transition) may contribute to the Raman scattering, the following conditions needed to be satisfied in order for the term B to be nonvanishing: 1) There is at least one allowed transition from the molecular ground state to the excited state. 2) Transitions from the molecule to the metal is allowed. 3) The direct product of $\Gamma_M \times \Gamma_K \times \Gamma_Q$ contains the totally symmetric representation, where Γ_M, Γ_K and Γ_Q are the irreducible representation of charge transfer sate, excited state and the vibrational mode, respectively. HOMO of BDT is b_1 symmetry and the LUMO is a_2 symmetry, assuming the C_{2V} symmetry (Fig. 3.3.7.). Therefore, the transition from the molecular ground state to the excited state ($b_1 \times a_2$=B2) is allowed. At room temperature, molecular orientation fluctuates with time in the molecule junction. In some instances, the molecular axis could orient normal to the surface. In this configuration, charge transfer state is a_1 symmetry (Fig. 3.3.8.).[26] $\Gamma_M \times \Gamma_K \times \Gamma_Q$ contains the totally symmetric representation for b_2 mode. Under these conditions, b_2 mode is enhanced by the B term. Here again, the interaction between molecule and metal electrodes leads to appearance of the b_2 modes. Since molecular orientation fluctuated at room temperature, b_2 modes did not always appear, which agreed with the experimental results. Several possibilities have been considered to explain the appearance of b_2 modes in SERS. A charge transfer (CT) process as discussed in the present study, and chemical reaction induced by the laser irradiation have been discussed to explain the appearance of b_2 modes for p-aminothiophenol on Ag surface[52-54]. Further investigation is required to fix the origin of the appearance of the b_2 modes.

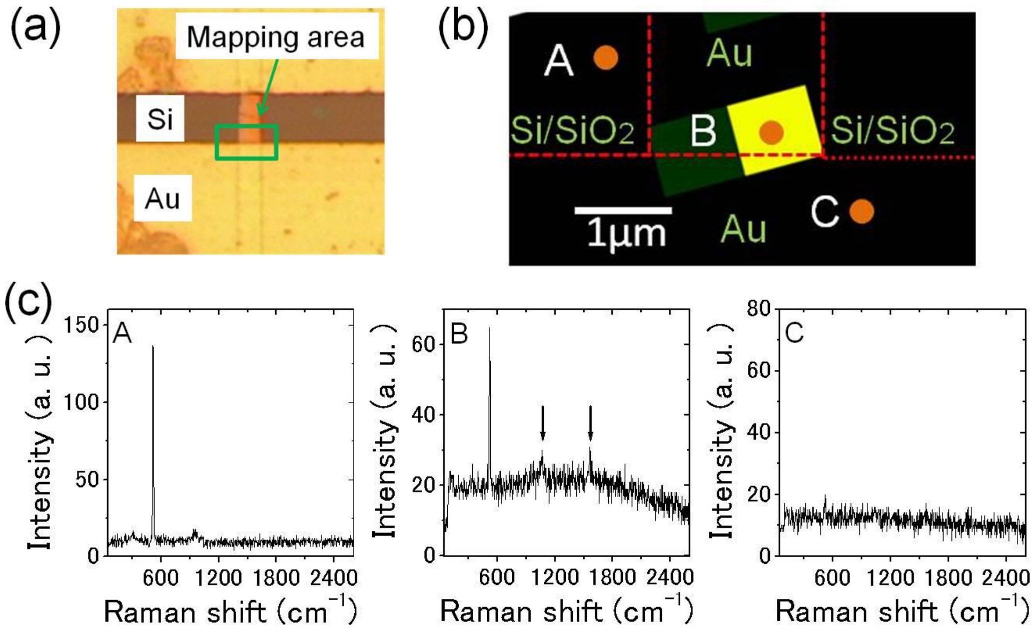

Fig. 3.3.1. (a) Photo image of the Au nano gap electrode, (b) Map of BDT SERS signal from the a_1 symmetry mode at 1561cm^{-1} (integrated from 1500 to 1620cm^{-1}), (c) Raman spectra of underlying (A) Si, (B) Au nanogap and (C) Au electrode. Reprinted with permission from R. Matsuhita, M. Horikawa, Y. Naitoh, H. Nakamura and M. Kiguchi, Conductance and SERS Measurement of Benzenedithiol Molecules Bridging Between Au Electrodes, *The Journal of Physical Chemistry C*, 2013, 117, 1791. Copyright 2013 American Chemical Society.[47]

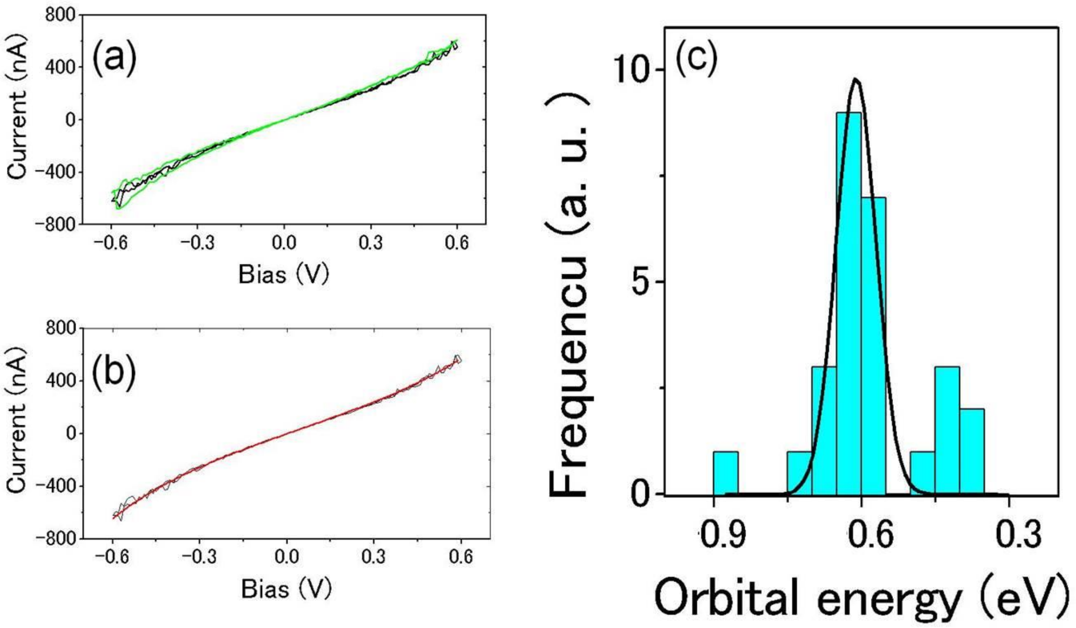

Fig.3.3.2. (a) Example of IV characteristic of BDT molecular junction before (black) and after (green) the SERS measurement, (b) IV characteristic of BDT molecular junction together with fitted results (red line) based on the single level tunneling model, (c) The distribution of ε_0 for BDT molecular junction obtained by 26 samples. Adapted with permission from R. Matsuhita, M. Horikawa, Y. Naitoh, H. Nakamura and M. Kiguchi, Conductance and SERS Measurement of Benzenedithiol Molecules Bridging Between Au Electrodes, *The Journal of Physical Chemistry C*, 2013, 117, 1791. Copyright 2013 American Chemical Society.[47]

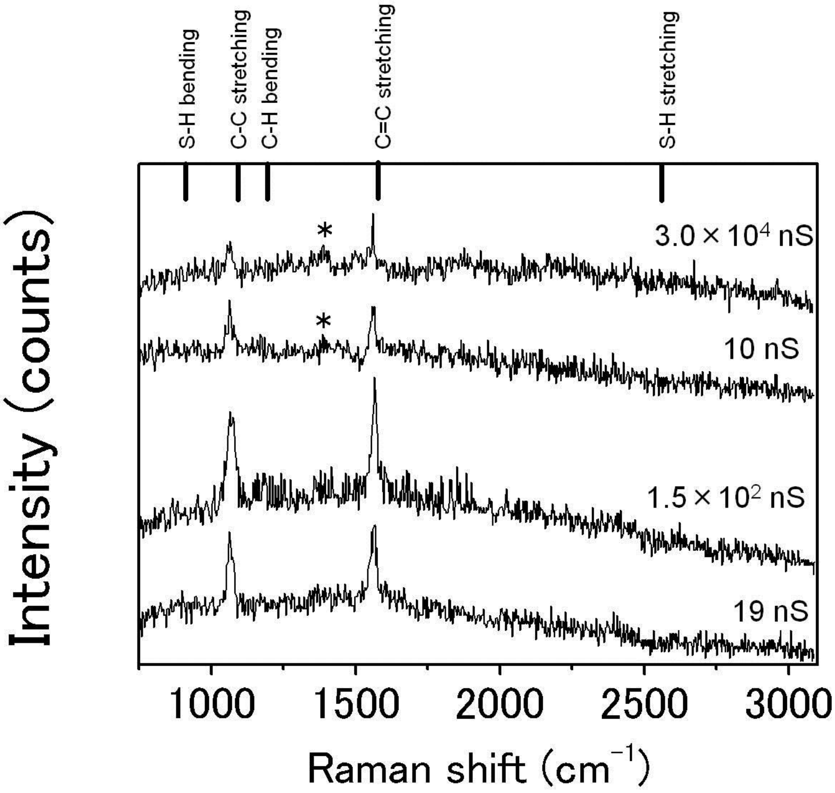

Fig. 3.3.3. Example of SERS of BDT molecular junctions. The inset shows the conductance of the molecular junction. The vertical lines indicate the vibration modes of the bulk crystal assigned to each mode with the calculation result. Reprinted with permission from R. Matsuhita, M. Horikawa, Y. Naitoh, H. Nakamura and M. Kiguchi, Conductance and SERS Measurement of Benzenedithiol Molecules Bridging Between Au Electrodes, *The Journal of Physical Chemistry C*, 2013, 117, 1791. Copyright 2013 American Chemical Society.[47]

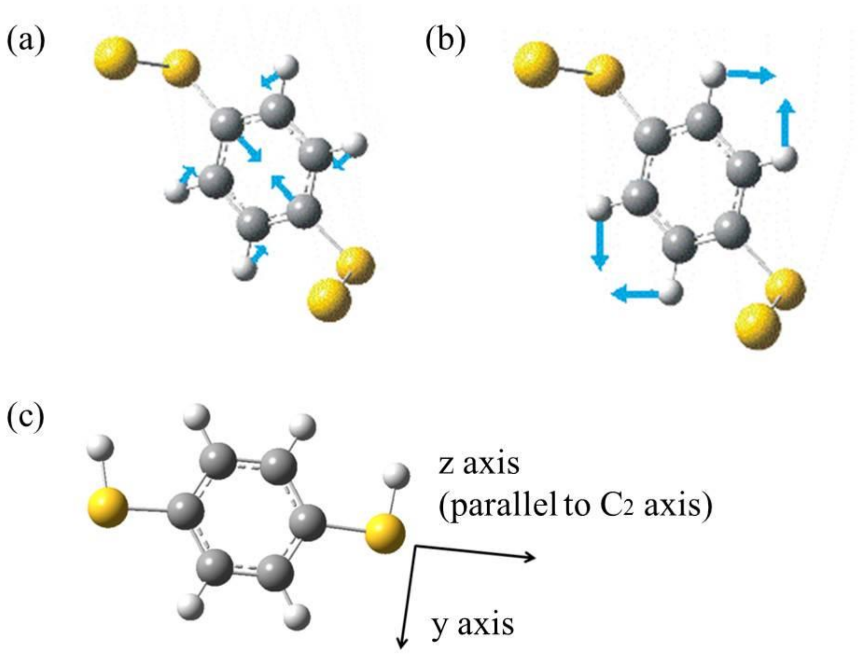

Fig.3.3.4. (a) a_1 mode of BDT molecule with two S-Au bonds assigned to the Raman signal at 1063 $\mathrm{cm^{-1}}$. (b) a_1 mode of BDT molecule with two S-Au bonds assigned to the Raman signal at 1562 $\mathrm{cm^{-1}}$. (c) Molecular structure of BDT molecule. DFT calculations were performed with Gaussian 03 by the B3LYP method using the basis sets of 6-31G(d,p) for C, H, and S, and LANL2DZ for Au atoms. The symmetric representations were assumed under a C_{2V} symmetric point group. The C_2 axis was chosen to be the molecular junction axis as shown in (c).

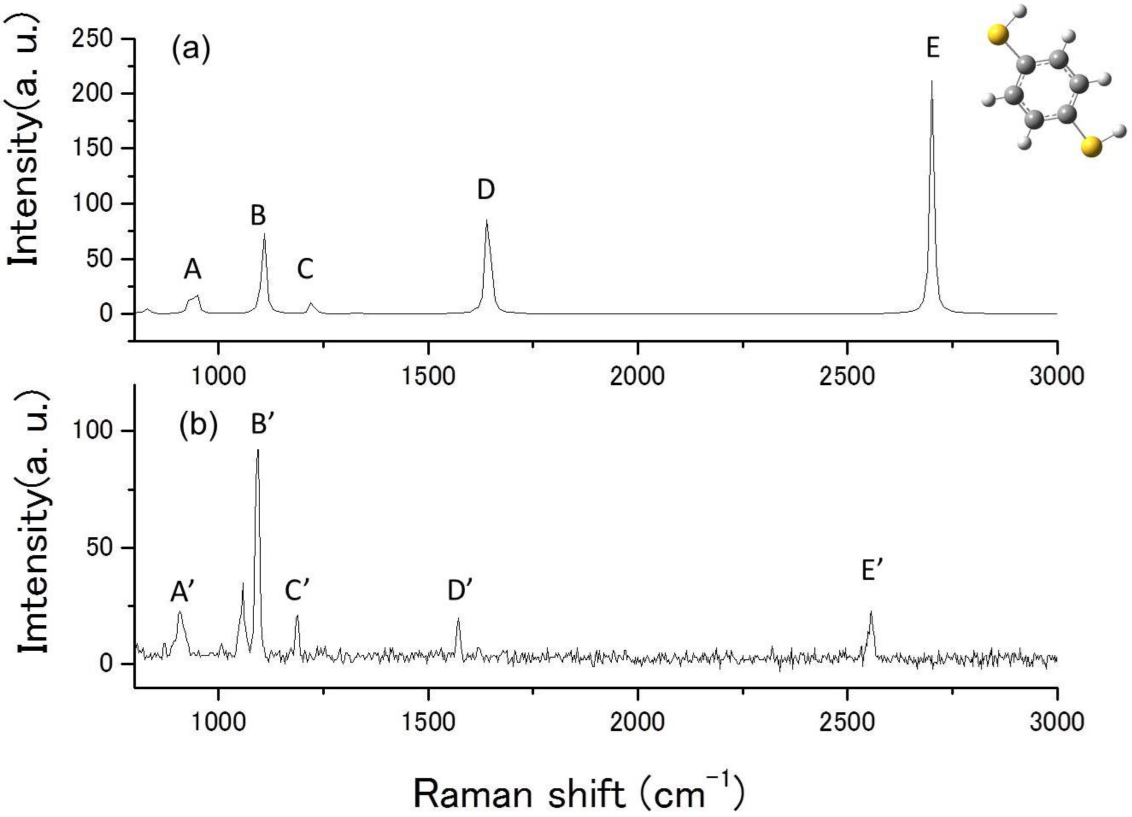

Fig.3.3.5. (a) The simulated Raman spectrum of BDT molecule. (b) The Raman spectrum of BDT bulk crystal.

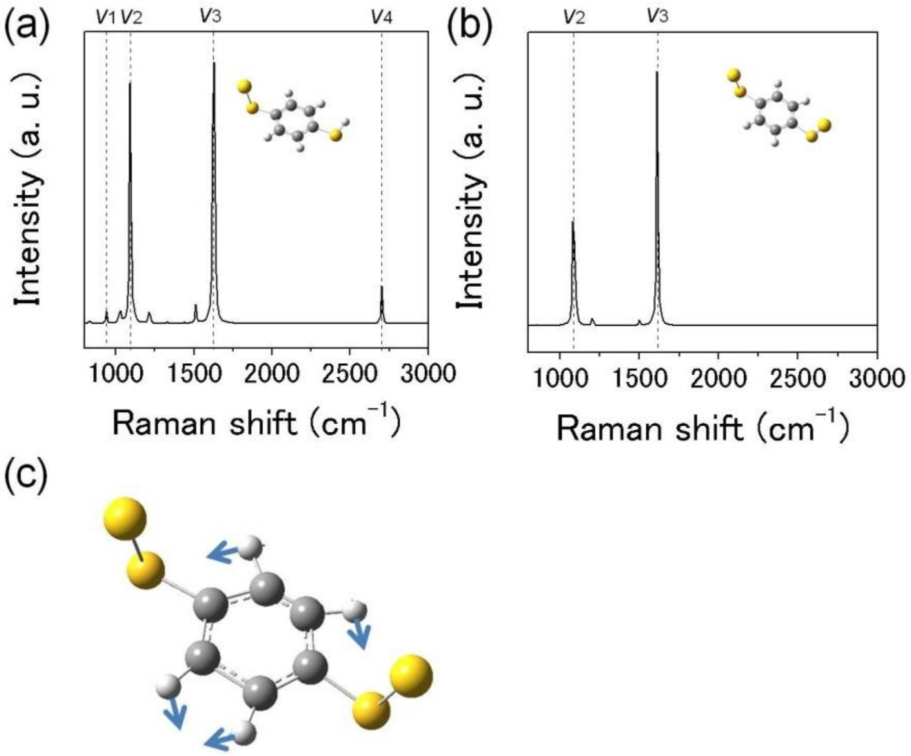

Fig.3.3.6. (a,b) The simulated Raman spectra of BDT molecules with one (a) and two Au atoms (b), respectively. ν_1, ν_2, ν_3, and ν_4 indicate S-H bending, C-C stretching, C=C stretching, and S-H stretching modes, respectively. Insets show the structures for each molecule. (c) The b_2 mode of BDT molecule with two S-Au bonds. Reprinted with permission from R. Matsuhita, M. Horikawa, Y. Naitoh, H. Nakamura and M. Kiguchi, Conductance and SERS Measurement of Benzenedithiol Molecules Bridging Between Au Electrodes, *The Journal of Physical Chemistry C*, 2013, 117, 1791. Copyright 2013 American Chemical Society.[47]

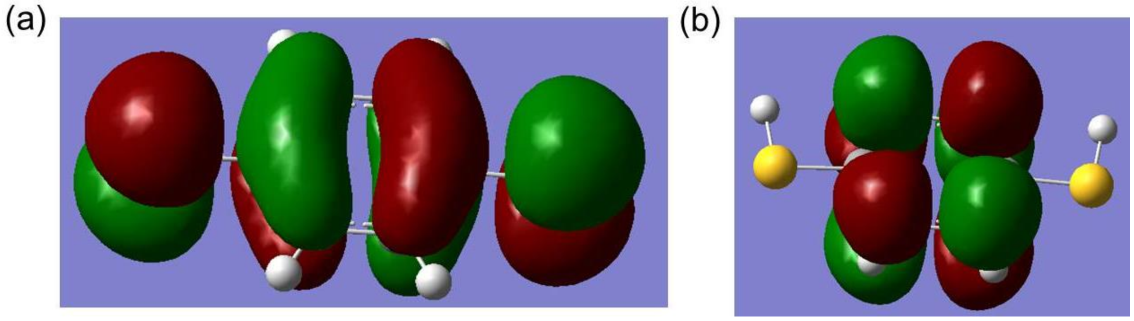

Fig.3.3.7. Molecular orbitals of a BDT molecule. (a) HOMO, (b) LUMO. Reprinted with permission from R. Matsuhita, M. Horikawa, Y. Naitoh, H. Nakamura and M. Kiguchi, Conductance and SERS Measurement of Benzenedithiol Molecules Bridging Between Au Electrodes, *The Journal of Physical Chemistry C*, 2013, 117, 1791. Copyright 2013 American Chemical Society.[47]

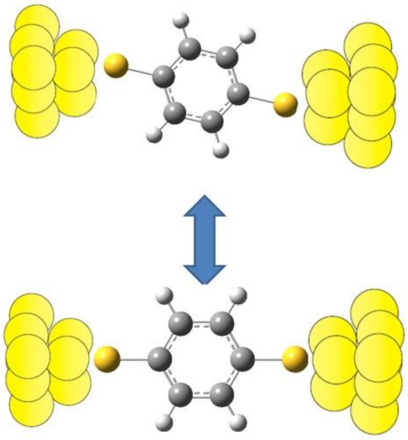

Fig.3.3.8. Schematic illustration of the structural fluctuation of the molecular junction.

Table.3.3.1. Vibrational energy of CO stretching mode.[51]

Compound	Vibrational energy/ cm^{-1}
CO(gas)	2143
$[Mn(CO)_6]^+$	2090
$[Cr(CO)_6]$	2000
$[V(CO)_6]^-$	1860
$[Ti(CO)_6]^{2-}$	1750

3.4. Conclusion

I have measured electric conductance and SERS spectra for the benzenedithiol molecules bridging between Au nano gap electrodes at room temperature. The number of the molecules and electronic structure of the benzenedithiol molecular junction were determined by the IV characteristics. The energy difference between conduction orbital and Fermi level was determined to be 0.6 eV based on the single level tunneling model considering that the Fermi distribution function got smeared out for finite temperature. The finite strength of the metal-molecule coupling (~10 meV) indicated the interaction between benzenedithiol molecule and Au electrodes. The SERS spectra were different from that of the bulk crystal, due to this interaction. The SH modes were not observed for the molecular junction, because the S-H bonds were broken and BDT molecule bound to both Au electrodes. The C=C (C-C) stretching mode was observed at 1562cm^{-1} (1063 cm^{-1}) for the molecular junction, while it was observed at 1572cm^{-1} (1094 cm^{-1}) in the bulk crystal. The redshift of the C=C and C-C stretching modes could be explained by the interaction between benzenedithiol molecule and Au. I observed the apperance of the b_2 modes for some molecular junctions, which were not observed in the bulk crystal. The appearance of the b_2 modes could be explained by the charge transfer between benzenedithiol molecule and Au. I could investigate the interaction between benzenedithiol molecule and Au by measurments on conductance and SERS.

4, Development of system to measure thermopower and electrical conductance simultaneously

To perform the simultaneous measurement of thermopower and electrical conductance, it is necessary to use a voltmeter, an ammeter, a voltage or current source, thermometers, and heaters. The measurement can be performed properly when each component operates correctly in the measurement system. In this chapter, I will explain the consideration of each component. Then, I will show the result of the measurement of thermopower for the thermocouple with the measurement system to check whether the system operates correctly.

4.1. Fabrication of heater

It is necessary to establish the temperature difference across the junction to induce thermoelecric voltage. The Pt resistive heaters explained below were used for this purpose. Fig.4.1.1. shows the schematic view of the heater. The Pt resistive heaters (width: 200 μm, length: 8 mm, thickness: 200 – 300 nm) were deposited on the polyimide tape by magnetron sputtering. The top of the heater was covered with polyimide thin film for electrical insulation. The covered Pt resistive heater was attached to the fluoroplastic saturated glass cloth tape for thermal insulation. The temperature was controlled by applying an electrical current to the Pt heaters.

Fig.4.1.1. Schematic view of the heater.

4.2. Thermometer

There are several kinds of thermometer such as thermocouple, resistance thermometer, diode thermometer, and radiation thermometer. In this study, resistance thermometers were used because of the easy handling. The resistance thermometers are used to measure the temperature by correlating the electrical resistance of the thermometer with the temperature. To measure the temperature above room temperature, platinum resistance thermometers were used. The platinum thermometer increases linearly in electrical resistance with an increase of the temperature. To measure the temperature below 150 K, RuO_2 resistance thermometers were used. The RuO_2 thermometer increases exponentially in electrical resistance with a decrease of the temperature. In the low temperature region, the Pt thermometer has two problems described below.

1, the linearity of change in electrical resistance is not maintained.

2, the sensitivity of the thermometer decreases with a decrease of the temperature.

Considering these problems, the RuO_2 thermometers were used to measure the temperature in the low temperature region. The Pt thermometers had been already calibrated by their manufacturer. On the other hand, RuO_2 thermometers had not been calibrated by their manufacturer. The calibration of the RuO_2 thermometers was performed as follows.

Fig.4.2.1. (a) shows the setup to for the calibration. The RuO_2 thermometers and a reference thermometer (calibrated Si diode thermometer) were attached to the surface of the copper block with varnish. Manganin wire heater was attached to the block to control the temperature by applying an electrical current. The setup (Fig.4.2.1. (a)) was placed inside the copper pot of the chamber shown in Fig.4.2.1. (b). The chamber was immersed in the liq. N_2 or liq. He after the evacuation. The calibration was performed by changing the temperature with the manganin heater and measuring the resistance of the RuO_2 thermometer and the temperature of the reference thermometer. (Fig.4.2.1. (c)) All RuO_2 thermometers used in this study were calibrated.

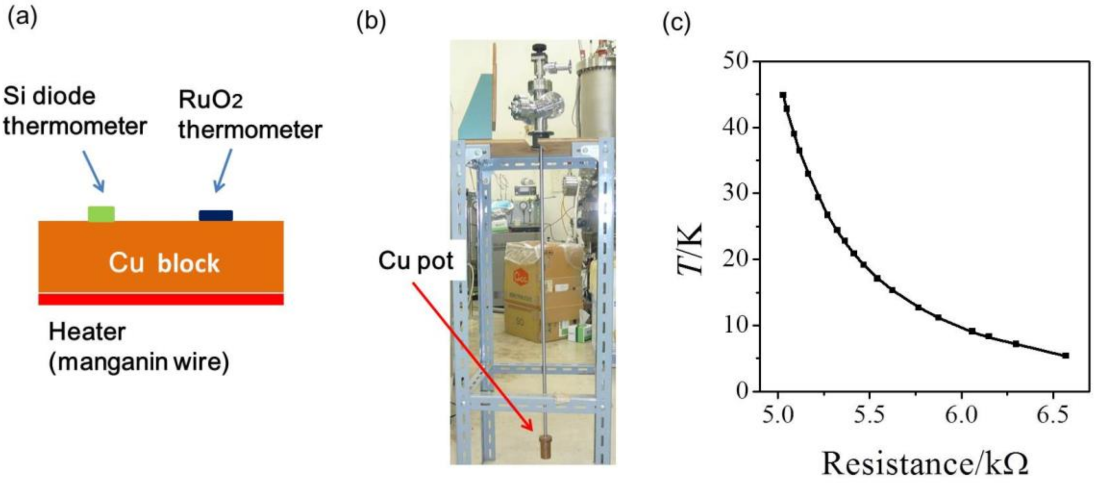

Fig.4.2.1. (a) Schematic view of the setup for the calibration of the RuO_2 thermometers. The Si diode thermometer was used as the reference thermometer. (b) Photograph of the chamber. The setup shown in (a) was placed in inside the copper pot. (c) Example of the calibration result of the RuO_2 thermometer. (Black points) Black curve is the fitting result.

4.3. Simultaneous measurement of thermoelectric voltage and electrical conductance with source measure unit

Source measure unit (SMU, or source meter) was used. SMU provides voltage and current sourcing and measurement capabilities. In this study, SMU was used to perform the simultaneous measurement of thermopower and electric conductance. The procedure of the measurement is shown in Fig. 4.3.1. (a). In the voltage measurement, measured voltage signal is affected by the offset voltage of the SMU. The offset voltage depends on the electrical resistance of the sample, measurement speed, and the day of the experiment. In this study, the measurement speed has been fixed for all measurements. The measurement of the offset voltage was performed after every measurement. Fig. 4.3.1.(b) shows the example of the resistance dependence of the offset voltage of the SMU used in this study. The offset voltage was 0 ~ 20 μV.

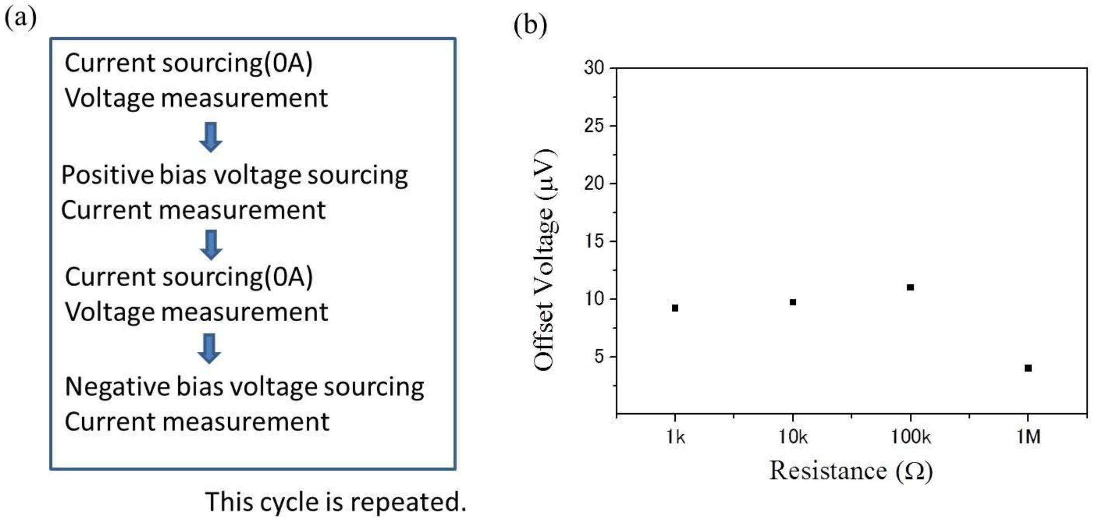

Fig.4.3.1. (a) Procedure of the simultaneous measurement of conductance and thermopower. (b) Example of resistance dependence of the offset voltage of the SMU used in this study. Fixed metal film resistors were used to estimate the offset voltage.

4.4. Measuring thermopower of Pt-Fe thermocouple

To check whether the thermopower measurement can be performed correctly with the Pt resistive heaters, the thermometers, and the source measure unit, the thermopower measurement was performed for a platinum-steel thermocouple at 300 K and 100 K. (Fig.4.4.1. (a)) The experimental values of the absolute thermopower of steel were compared with those of a literature. Fig.4.4.1. (b) shows the results of the measurement at 300 K and 100 K. The relative thermopowers $\Delta V/\Delta T$ were evaluated by the linear fitting for the results. The values of $\Delta V/\Delta T$ are shown in Table.4.4.1. The absolute thermopower of steel can be estimated by

$$S_{\mathrm{Fe}} = S_{\mathrm{Pt}} - \Delta V/\Delta T \quad \cdots \quad 4\text{-}4\text{-}1$$

where S_{Fe} and S_{Pt} are absolute thermopower of steel and platinum, respectively. By using the literature values of S_{Pt}, the experimental values of S_{Fe} can be estimated. The experimental and literature values of S_{Fe} are shown in Table.4.4.1. The experimental values of S_{Fe} agree with those of the literature. From this result, I concluded that the thermopower measurement was performed correctly with the Pt resistive heaters, the thermometers, and the source measure unit described above.

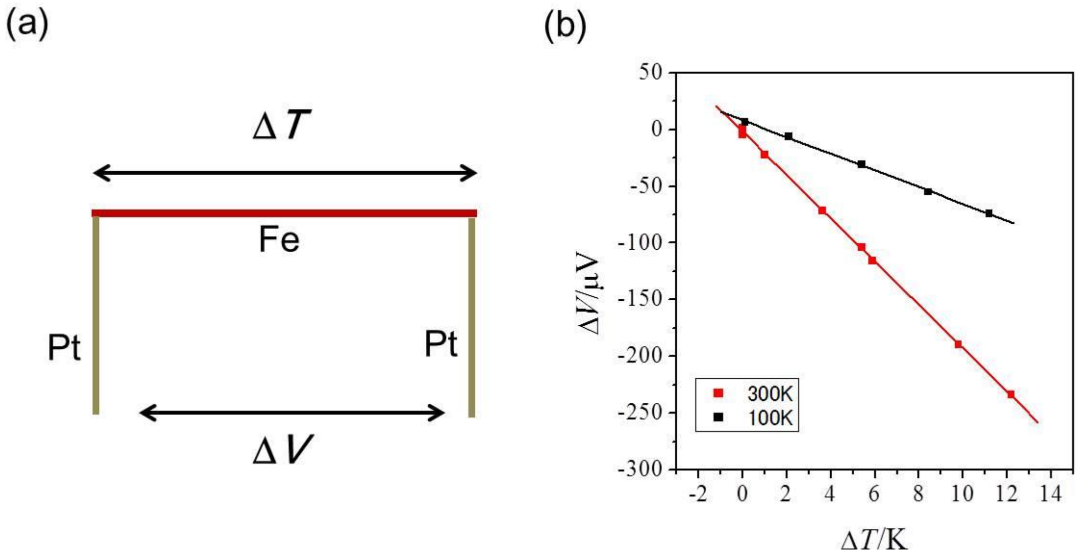

Fig.4.4.1. (a) Schematic view of the Pt-Fe thermocouple. Thermoelectric voltage ΔV can be induced by establishing the temperature difference ΔT between the two Pt-Fe contacts. (b) The thermoelectric voltage ΔV as a function of the temperature difference ΔT for 300 K (red square) and 100 K (black square). Red and black lines are the linear fitting results. For the measurements at 300 K and 100 K, Pt thermometers and the calibrated RuO_2 thermometers were used, respectively.

Table 4.4.1. Experimental results and literature values for the measurement of Pt-Fe thermocouple

Temperature in the measurement	$\Delta V/\Delta T$ ($\mu V \cdot K^{-1}$)	S_{Pt}(literature**) ($\mu V \cdot K^{-1}$)	S_{Fe}(experiment) ($\mu V \cdot K^{-1}$)	S_{Fe}(literature***) ($\mu V \cdot K^{-1}$)
300*	-19.1	-5.28	13.8	14
100*	-7.4	4.29	11.7	12

* The average of the temperature was 303 K for “measurement at 300 K” and 95 K for “measurement at 100 K”, respectively.

**From Ohtsuka *et al.* [35]

*** From Blatt *et al.* [55]

5, Measurement of thermopower of single Au atomic junction

5.1. Introduction

Au atomic junctions have been most widely utilized as metal electrodes for single molecular junctions. In this study, Au electrodes were used to fabricate the Au/BDT junctions and to analyze the atomic and electronic structure of the junctions. As mentioned above, thermopower measurements were performed for Au/BDT junctions to analyze the electronic structure. Before that, the measurements of thermopwer of gold atomic junctions were performed to (1) check whether the thermopower measurements can be performed properly for the atomic-sized system and (2) elucidate the thermoelectric property of the single gold atomic junctions which were used as the electrodes in the Au/BDT junctions.

Thermoelectric effects of Au atomic junctions have been studied as a model system of atomic and molecular junction. Ludoph *et al.* investigated thermopower of Au atomic junctions in vacuum at low temperature (~10 K)[36]. The thermopower was randomly distributed and was either positive or negative in sign.(Fig. 2.4.3.) The variation of thermopower decreased with the conductance of the junctions with the oscillation whose period was $2e^2/h$ (G_0). The oscillation was caused by the quantum interference: the electron wave transmitted through the junction is backscattered to the junction by impurities or defects and then partially reflected at the junction, this wave interferes with the directly transmitted wave and modifies the conductance. Tsutui *et al.* investigated the thermopower of the Au atomic junctions in vacuum around room temperature.[56] The thermopower depended on the junction conductance and oscillated with a period of G_0. Through these investigations, it has been clarified that the thermopower of the Au atomic junction is sensitive to the atomic configuration.

While thermopower measurements have been performed for various metal atomic contacts and molecular junctions, the temperature dependence of the thermopower has not been studied satisfactory. The change in the temperature of the junction modulates the shape of the Fermi distribution function and atomic configuration of the junction, which can induce the change in the thermopower. Actually, Nakamura *et al.* showed the significant temperature dependence of the thermopower for the single organometallic complex wire using the theoretical calculation (Fig.2.4.5.)[38]. The thermopower monotonically decreases with the temperature and changes its sign from positive to negative at 220 K. The distinct sign change of thermopower is caused by the existence of many molecular orbitals nearly the Fermi level. However, there are little experimental investigations on the effect of temperature on the thermopower of the atomic and molecular junctions.

In the present study, I focused on the temperature dependence of the thermoelectric voltage and its variation of the Au atomic contact.[57] The origin of the variation of thermopower has been discussed based on the quantum interference of electrons backscattered by defects near the contact, and variation of the atomic configuration[36, 58].

5.2. Experimental

The measurements were performed using a MCBJ technique in air around room temperature[59]. A schematic diagram of the sample configuration is shown in Fig. 5.2.1.(a). By bending the phosphor bronze substrate, the notched Au wire (0.1 mm in diameter, 10 mm in length) breaks, allowing atomic-size contacts to be adjusted. The substrate was fabricated as the following process. The two Pt resistive heaters (width 200 μm, length 8 mm, thickness 200-300 nm) was deposited on the polyimide tape by magnetron sputtering. The top of the heater was covered with the polyimide tape for electrical insulation. The covered Pt heater was put on the phosphor bronze substrate using fluoroplastic saturated glass cloth tape. The notched Au wire was fixed with epoxy adhesive (Stycast 2850FT) on the covered Pt heater, where each side of the contact was touched to the heater. The platinum resistance thermometer sensors (Pt-100) were attached to the each side of the contact. The notched Au wire was attached to long thin (50 μm) Cu wires at both ends. They connected the notched Au wire to the current and voltage leads, anchored at the bath temperature, hence forming an open gold loop. The glass cloth tape and thin Cu wire served as thermal resistance to the substrate and bath temperature, respectively. The sample was placed in a regular MCBJ setup.

The conductance and thermopower were measured in four steps (Fig. 4.3.1.). The voltage over the contact was measured at zero dc bias current twice, and the current over the contact was measured at +50 mV and -50 mV dc voltage bias. Each cycle took about 0.3s. The current and voltage were measured with a source measure unit (Keithley 2612A) while maintaining a constant temperature gradient over the contact and sample temperature by applying about 10-400 mW heating power to the Pt heaters. The conductance was obtained from the current difference for the two voltage polarities, and the thermoelectric voltage was obtained by averaging the two voltage values at zero bias current. The thermopower was obtained by dividing thermoelectric voltage V_{TE} by temperature difference across the contacts ΔT. Here, I subtracted the contribution of the offset voltage of the source measure unit, which was evaluated with standard resistor (1k~1M Ω), and the contribution of thermopower of bulk Au (1.94 μV/K)[34]. The thermopower and conductance measurements were performed with the 4 distinct samples. The formation of the Au atomic contacts was checked by the conductance measurements using MCBJ setup. Fig. 5.2.1.(b) shows the conductance traces and histogram of the Au contacts measured. The appearance of plateaux and a peak at 1 G_0 indicated the successful preparation of single Au atomic contacts [59].

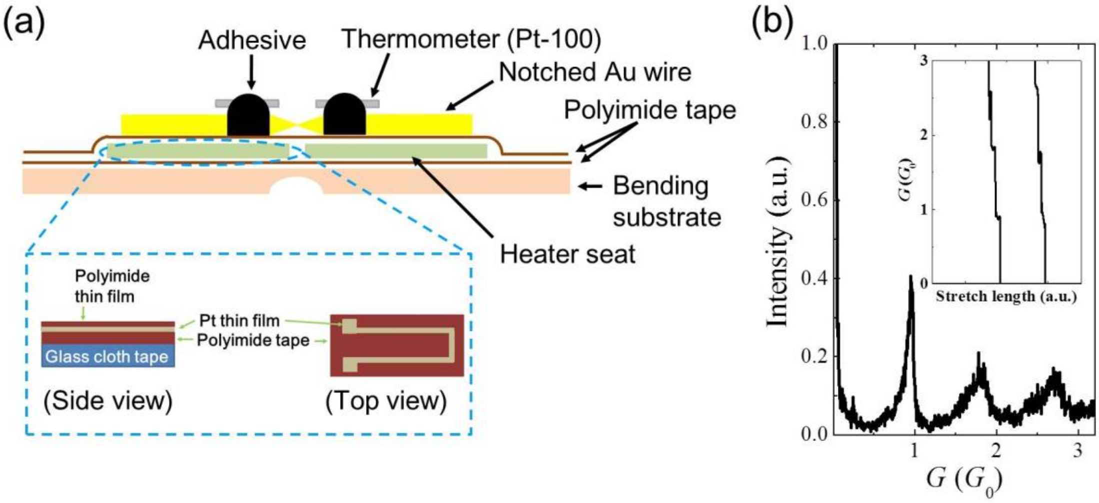

Fig.5.2.1. (a) Schematic diagram of the modified MCBJ setup used for simultaneous measurement of conductance and thermopower. (b) Conductance histogram of Au contacts constructed from 404 traces. Bias voltage was 0.1 V. Inset shows conductance traces. Reprinted with permission from R. Matsushita, S. Kaneko, S. Fujii, H. Nakamura and M. Kiguchi, Temperature dependence of the thermopower and its variation of the Au atomic contact, *Nanotechnology*, 2015, 26, 045709. Copyright 2015 IOP Publishing.[57]

5.3. Results and discussion

Fig.5.3.1.shows examples of the simultaneous measurement of thermoelectric voltage and conductance of the Au contacts during the self breaking process. The self breaking is a thermally activated fracture of the Au atomic contact. In this study, the Au contacts were stretched until the conductance of the nanocontact was around 10 G_0. Then the electrode separation was fixed, and the conductance and thermoelectric voltage of the Au contacts were measured during the self-breaking process. The thermoelectric voltage was randomly distributed around the horizontal line, and its fluctuation was large at low conductance regime. The abrupt change in the thermoelectric voltage did not always correlate with the change in the conductance.

Fig. 5.3.2.(a) shows plot of thermopower against conductance (G) obtained from 19 traces. Note that the thermopower fluctuated more largely in lower conductance region with both positive and negative in sign, which consisted with the Fig. 5.3.1. and agreed with the previous study by Ludoph and van Ruitenbeek[36]. Figure 5.3.2.(b) shows a standard deviation of thermopower against conductance. The standard deviation was evaluated by sorting all data points as a function of conductance. The standard deviation of thermopower increased with a decrease in the conductance and drastically increased below 1 G_0. Considering the coherent backscattering of the electrons near the contact, the standard deviation of the thermopower is represented by $\sigma_S = A\frac{\sqrt{\sum_{n=1}^{N}\tau_n{}^2(1-\tau_n)}}{\sum_{n=1}^{N}\tau_n}$, where A and τ_n are the constant and transmission of n-th channel, respectively [36]. When it is assumed that the transmission channels open one by one, σ_S can be simplified to $\sigma_S = A(n - G/G_0)^{0.5}/n$ for $G \rightarrow nG_0$ in the conductance interval $(n\text{-}1)G_0 < G < nG_0$, where n is the integer[60]. This equation explains the general trend of the decrease in the standard deviation of the thermopower with an increase in conductance (n). When the number of transmission channel is one, σ_S can be simplified to $\sigma_S = A\sqrt{1-\tau}$, which explains the drastic increase in σ_S below 1 G_0 as shown in Fig. 5.3.2.(b)).

Fig. 5.3.3.(a) shows the average and standard deviation of the thermoelectric voltage for the Au atomic junctions showing conductance value of 1 G_0 (0.7-1.3 G_0), as a function of the temperature difference across the junction. The average thermoelectric voltage was close to zero, which did not depend on the temperature difference. In

contrast, the standard deviation linearly increased with the temperature difference across the contact, indicating that the individual atomic junction had a certain thermopower and the thermoelectric voltage linearly increased with the temperature difference across the contact. The thermopower depends on the first derivative of transmission curve to the energy at the Fermi level as follows.

$$S = -\frac{\pi^2 {k_B}^2 T}{3e}\frac{\partial ln\tau(E)}{\partial E}|_{E=E_F} \cdots \text{ (5-3-1)}$$

In the case of Au atomic junction, the transmission curve is flat near the Fermi level for perfect atomic contacts, leading to the thermopower value of zero[61]. The defects and impurities near the contact modulate the transmission curve, and the first derivative of transmission curve to the energy can take various finite values either positive or negative in sign[36]. The average thermoelectric voltage, thus, became zero by averaging the thermoelectric voltage of the Au atomic junctions, while the average of the absolute value of the thermoelectric voltage, that is, the standard deviation of the thermoelectric voltage linearly increased with the temperature difference across the contact.

Figure 5.3.3.(b) shows the average and standard deviation of the thermopower of the Au atomic junctions showing conductance value of 0.7-1.3 G_0 as a function of the sample temperature. The average thermopower was obtained from 19 data sets. The average thermopower was close to zero, which was negligibly small with respect to the variation of the thermopower of the junction, which agreed with the result performed by Ludoph *et al.*[36] Meanwhile, Tsutsui *et al.* reported the negative thermopower of the Au atomic junction[56]. The difference can be explained by the formation process of the Au atomic contacts. Ludoph *et al.* and I prepared the Au atomic junctions after making the large Au contacts which induced large structural variation in the bulk electrodes. On other hand, Tsutsui *et al.* prepared the Au atomic contacts using a feedback mechanism to hinder fusing of the contact during the formation process. The individual Au atomic contacts contained large structural variation for the Ludoph *et al.* and our sample, while the Tsutsui's sample had a similar structure including the distribution of defects and impurity near the junction. In the Tsutsui's sample, the distribution of defects and impurity near the junction was fixed, and thus, they showed a finite thermopower, because the thermopower was sensitive to the distribution of defects, as discussed in the previous section. On the other hand, in Ludoph *et al.* and my sample, the distribution of

defects and impurities near the junction was not controlled. Therefore, the average thermopower became zero by averaging the samples with large structural variation. In the case of the Au atomic junction prepared with the break junction technique, it is impossible to control the distribution of defects near the junction.

Considering Eq.5-3-1, the standard deviation of thermopower seems to increase with the sample temperature. However, the observed standard deviation of thermopower decreased above 320 K (see Fig. 5.3.3. (b)). Transmission curve through the contact depends on the distribution of impurities or defects within a coherent length of the contact, as discussed in the above[62]. The variation of the thermopower increases with the density of the defects near the junction. The observed decrease in the variation of the thermopower above 320 K suggests the decrease in the density of defects of the Au atomic junction. That means, I could evaluate the crystallinity of the Au atomic contacts by the variation of the thermopower.

I then discuss the mechanism of the decrease in the density of defects near the contact above 320 K. The atomic motion and diffusion increases with the decrease in the coordination number of metal[63-67]. The decrease in the melting temperature of the nanometer sized metallic clusters has been reported in experimental and theoretical studies (Fig. 5.3.4. (a))[63, 64]. Malis *et al.* studied the temperature induced structural change of 1-5 nm Au nano particles supported on silicon substrate with x-ray diffraction [66]. The nano particles underwent dramatic structural changes at temperatures as low as 390 K. Nan *et al.* reported that the surface corrugation change became apparent for the Au thin film above 370 K using UHV-scanning tunneling microscope (STM) (Fig. 5.3.4. (b) [65]. Peale *et al.* reported that mass flow on the Au (111) surface in air even at room temperature with STM[67]. The Au atomic junction is a low dimensional nano structure, and thus the atomic motion should be enhanced compared to the bulk Au. Above the 320 K, the atomic motion could be significantly enhanced, and thus, the crystallinity of the junction was improved, leading the decrease in the density of defects near the junction.

Here it should be noted that variation of the thermoelectric voltage decreased above 320 K as shown in Fig. 5.3.3.(b), while Fig. 5.3.3.(a) shows that the variation of the thermoelectric voltage linearly increased with the temperature difference across the contact. In the latter experiments, the temperature difference was below 16 K, that means, the average sample temperature was kept below 320 K, where the improvement of the crystallinity was not observed. Therefore the variation of the thermoelectric voltage linearly increased with temperature difference (Fig. 5.3.3.(a)).

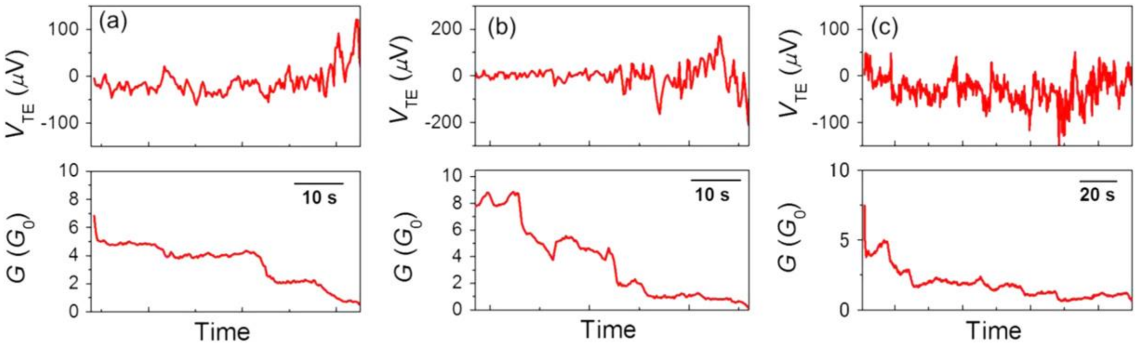

Fig. 5.3.1. Simultaneous conductance and thermoelectric voltage measurement during the self-breaking process. (a) The temperature of the hot (T_H) and cold (T_L) side were T_H = 304 K and T_L = 295 K, T_{ave} = 299 K (average between T_H and T_L), (b) T_H = 311 K, T_L = 297 K, T_{ave} = 304 K, (c) T_H = 334 K, T_L = 321 K, T_{ave} = 328 K. Reprinted with permission from R. Matsushita, S. Kaneko, S. Fujii, H. Nakamura and M. Kiguchi, Temperature dependence of the thermopower and its variation of the Au atomic contact, *Nanotechnology*, 2015, 26, 045709. Copyright 2015 IOP Publishing.[57]

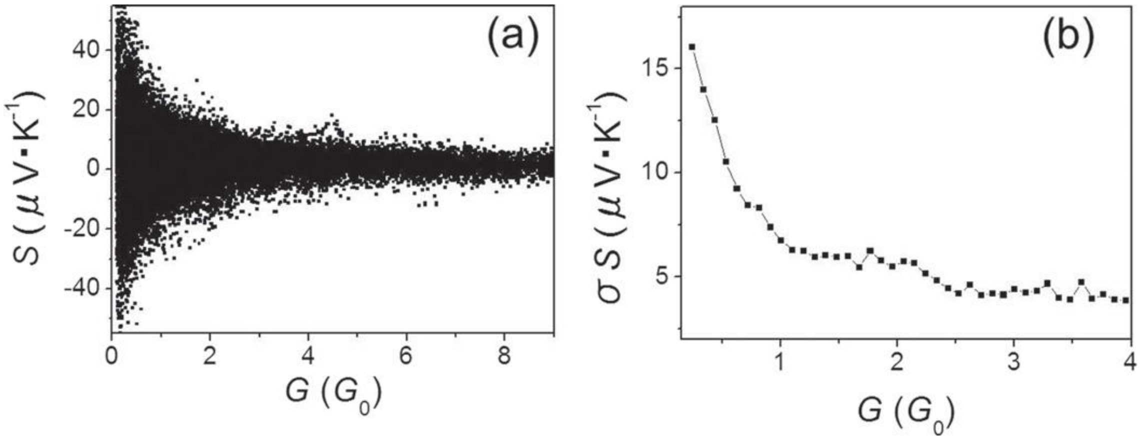

Fig. 5.3.2. (a) Plot of thermopower (S) against conductance (G) obtained from 19 traces, (b) standard deviation of thermopower against conductance. The bin size is $0.095G_0$. The sample temperature (T_{ave}) was at 310 ± 10 K. Reprinted with permission from R. Matsushita, S. Kaneko, S. Fujii, H. Nakamura and M. Kiguchi, Temperature dependence of the thermopower and its variation of the Au atomic contact, *Nanotechnology*, 2015, 26, 045709. Copyright 2015 IOP Publishing.[57]

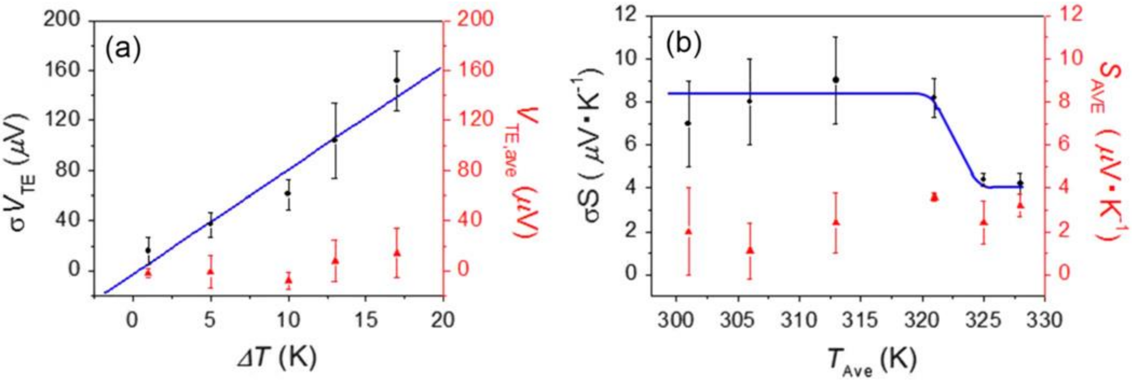

Fig.5.3.3. (a) The average ($V_{\mathrm{TE,ave}}$: red triangle) and standard deviation ($\sigma\ V_{\mathrm{TE}}$: black circle) of the thermoelectric voltage as a function of temperature difference across the contact obtained from 17 conductance and thermoelectric voltage traces. The conductance of Au atomic contact was 0.7–$1.3G_0$ and the sample temperature was at 300 ± 10 K. Blue is the fitting result, with a linear line. (b) The average (S_{ave}: red triangle) and standard deviation (σS: black circle) of the thermopower of the Au atomic contact as a function of the sample temperature (T_{ave}) obtained from 19 conductance and thermoelectric voltage traces. The blue line is given as a guide to the eye. Reprinted with permission from R. Matsushita, S. Kaneko, S. Fujii, H. Nakamura and M. Kiguchi, Temperature dependence of the thermopower and its variation of the Au atomic contact, *Nanotechnology*, 2015, 26, 045709. Copyright 2015 IOP Publishing.[57]

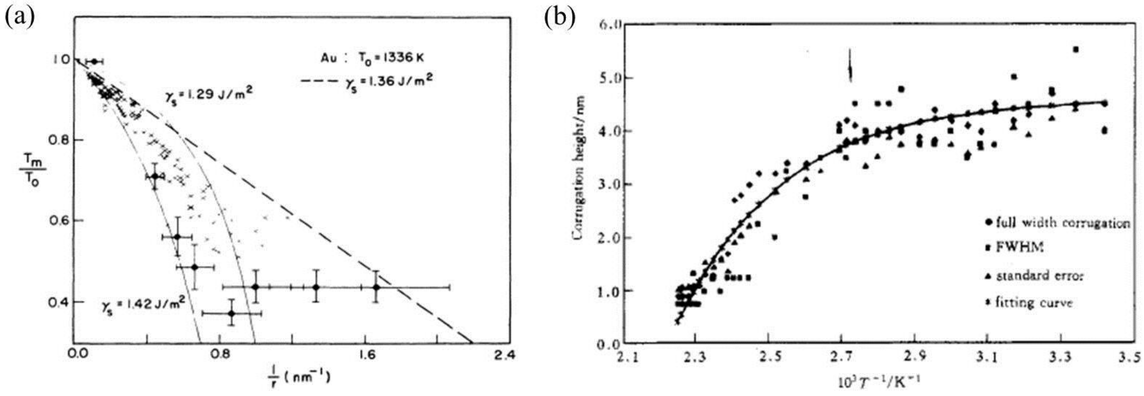

Fig. 5.3.4. (a) A plot of the relative lowering of the melting point for gold clusters vs the inverse cluster radius. T_m: melting point, T_0: melting point of bulk Au, r: Cluster size. Reprinted with permission from T. Castro, R. Reifenberger, E. Choi and R. Andres, Size-dependent melting temperature of individual nanometer-sized metallic clusters, *Physical Review B*, 1990, 42, 8548. Copyright 1990 American Physical Society. [64] (b) Plot of surface corrugations versus temperature for Au thin film. A transition temperature at ~ 100°C is indicated by an arrow. Reprinted with permission from L. Nan, D. Allan and L. Gang-Yu, In situ STM study of thermal annealing of Au thin films: An investigation on decay of nanometer Au clusters and 2D islands, *ACTA PHYSICA SINICA (Overseas Edition)*, 1997, 6, 531. Copyright 1997 Chinese Academy of Sciecne.[65]

5.4. Conclusion

The simultaneous measurement of thermopower and conductance were performed for Au atomic junctions during the breaking process in air around room temperature. It was shown that the system for themopower measurement developed in this study can be used to study the thermoelectric feature of the atomic-sized junction. The thermopower was randomly fluctuated especially large in lower conductance region with both positive and negative in sign. While the average thermopower was negligibly small, the standard deviation of thermoelectric voltage linearly increased with the temperature difference across the contacts. The standard deviation of the thermopower increased with a decrease in the conductance and drastically increased below 1 G_0. The increase in the standard deviation of thermopower was explained by the coherent backscattering of the electrons near the junction. Above 320 K, the standard deviation of thermopower decreased, which indicated the decrease in the density of defects for the Au atomic junctions. The Au atomic junctions are low dimensional nano materials, therefore, the atomic motion could be significantly enhanced junctions. The present study indicates that the standard deviation of the thermopower provides the information about thermopower of the Au atomic junction and the atomic structure of the Au atomic junctions (e.g. crystallinity and distribution of defects).

6, Analysis of atomic and electronic structure of 1,4-benzenedithiol molecule bridging between Au electrodes

6.1. Introduction

In Chapter 3, the basic properties of the atomic and electronic structure of Au/BDT junctions were elucidated. From the SERS measurements, it was shown that (1) the SH bonds were broken and BDT molecule bound to both Au electrodes and (2) the interaction between molecule and gold electrodes leaded to the decrease in the bond strength of the molecule. From IV characteristic measurements, the energy difference between conduction orbital and Fermi level was estimated to be 0.6 eV. On the other hand, the dynamics and type of conduction (transport through HOMO or LUMO) of the molecular junctions were not discussed well in this study. In Chapter 5 by using the thermopower measurement system for the single Au atomic junctions, it was found that the average of theropower was ~ 0 μV/K at room temperature.

In the present study, the thermopower measurement system constructed in this study was used to analyze the electronic structure of the molecular junctions in the dynamics. Molecular junctions show the various values of the physical property. This is because the physical property is sensitive to the fluctuation at atomic structure. The sensitivity of the physical property to the atomic structure is disadvantage for the stability of the physical property of the junction. On the other hand, that is also advantage because one specific junction can show a variety of physical properties by changing the atomic/electronic structure.(ex. switching in Fig. 1.1.8.) To exploit the diversity of the physical property of the junction, it is necessary to clarify the atomic and electronic structure of the junction in the dynamics.

To understand the atomic and electronic structure of the junctions, experimental methods are well used with the theoretical calculation. For example, H. Rascon-Ramo *et al.* applied a small-amplitude, high frequency, sinusoidal mechanical signal to a series of molecular junctions during junction formation and breakdown[68]. They determined the most probable binding and contact configurations for the molecular junctions at room temperature in solution by measuring the current response signal and performing the molecular dynamics simulation. Theoretical calculation enables people to understand the electronic and atomic structure in detail. On the other hand, there is a risk in using the theoretical calculation because it is always assumed that molecular junctions have some specific structure. As stated above, one of the characteristics of the molecular junctions is the diversity of the atomic/electronic structures. The assumption can exclude the possibility that the junctions have the structures except the structures used in the calculation.

Therefore, it is important to combine some experimental methods to understand the atomic and electronic structure comprehensively. For example, H. Song *et al*, measured the gate voltage dependence of the conductance of the molecular junction[8]. In the measurement, they performed the vibrational spectroscopy (IETS) to confirm the chemical species in the junction. Electronic structure analysis (gate voltage dependence of the electronic conductance) and atomic structure analysis (IETS) were combined to understand the atomic/electronic structure of the junction comprehensively. In their study, the fixed nanogap electrodes were used. The fixed nanogap electrode has the advantage to fabricate the stable molecular junction rather than the break junction (BJ) technique. Therefore, they did not mention the dynamics of the molecular junction.

In the usage of break junction technique, the atomic structures of the junction tend to change more easily than the usage of fixed nanogap electrode. Therefore, BJ technique is appropriate for studying the dynamics of the molecular junctions.

In this study, themopower, conductance, IETS, and IV characteristic were measured in situ for the Au/BDT molecular junction to understand the atomic and electronic structure in the dynamics of the molecular junction comprehensively.[69]

6.2. Experimental

The simultaneous measurements of thermopower and conductance were performed with the same way with the MCBJ substrates explained in 5.2. Pt thermometers and RuO_2 thermometers were used for the measurements around room temperature (300 – 320 K) and at low temperature (20 ~ 50 K). A ring cell fabricated by silicone resin on a MCBJ substrate was filled with a dilute ethanol solution of BDT molecules adjusted to a concentration of 5 mM. Then, the substrate was left in air for the evaporation of the solvent. The MCBJ substrate was bent by a three-point bending mechanism to adhere BDT molecules on the fresh breakage Au surface. For the measurements at low temperature, the samples were put in the vacuum chamber, which was cooled down by immersing the chamber in the liq. He. (Fig. 6.2.1.) The contribution of thermopower of bulk Au was subtracted with the literature value of thermpower of bulk Au.[70, 71]
In the simultaneous measurements of thermopower and conductance at low temperature, IV characteristics and IETS were also measured in situ. IV characteristics were measured with the DAQ device. IETS measurements were performed using a standard lock-in technique. (Fig. 6.2.2.) The conductance was recorded for the fixed contact configuration using an AC modulation of 1 mV amplitude and 7.777 kHz frequency while slowly ramping the DC bias between −100 and +100 mV. The experiments were performed for 3 and 8 independent samples for the measurements around room temperature and at low temperature, respectively.

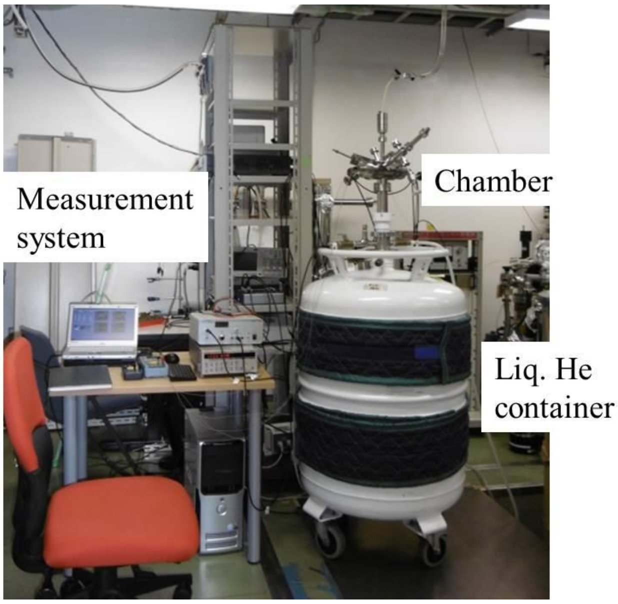

Fig. 6.2.1. Photograph of the apparatuses for the thermopower, IETS, and *IV* characteristic measurements at low temperature. Samples were put the chamber and cooled by immersing the chamber in liq. He.

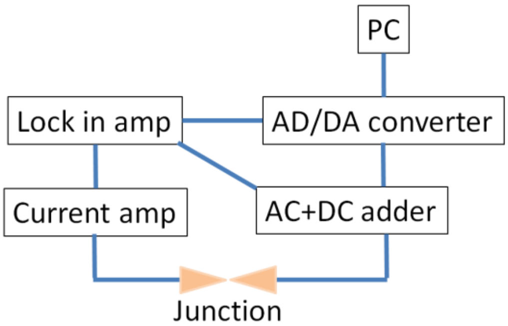

Fig.6.2.2. Electric circuit for IETS measurement

6.3. Results and discussion

Fig.6.3.1. shows examples of the simultaneous measurement of thermoelectric voltage and conductance of the Au/BDT junctions during the breaking process at room temperature. For the 3 samples, the measurements were performed at different temperature differences. Fig.6.3.2. (a) shows the average of the thermoelectric voltage showing a conductance value of 0.009–0.1 G_0, as a function of the temperature difference over the junction. The average values tend to be positive in sign because the positive voltage signals appeared more frequently than the negative ones. On the other hand, the behaviors of the thermoelectric voltage differed from each other. In the simultaneous measurement of thermoelectric voltage and conductance, positive (Fig. 6.3.1.(a) and (b)) and negative (Fig. 6.3.1.(c) and (d)) voltage signals were observed. To elucidate the thermoelectric properties of the Au/BDT junctions which show the positive and negative voltage, the data was divided to the group showing the positive voltage signals and the one showing the negative voltage signals. Then, the average values of the thermoelectric voltage were calculated for each group. The results of the analysis are shown in Fig. 6.3.2.(b). As stated above, the behaviors of the average of the thermoelectric voltage differed from each other in Fig.6.3.2. (a). This is because of the difference in the contributions of the positive and negative voltage signals to the whole data in each experiment.

Here, it should be noted that the behavior of the positive voltage signals agreed with each other for the 3 sample. In the simultaneous measurement of thermoelectric voltage and conductance, the positive voltage signals were observed more frequently than the negative ones. For the positive voltage signals, thermopower was estimated to be +15.5 μV/K by fitting the average values linearly. (Fig. 6.3.3.) This value is close to the values of +15 μV/K obtained by Tsutsui[72] *et al.* and +8.7 μV/K obtained by Reddy *et al.*[37] (Fig. 2.4.4.) The result indicates that electron transport occurs mainly through HOMO in the BDT molecular junctions as shown in Fug. 6.3.4[73]. On the other hand, the negative voltage signals were also observed as stated above. In terms of the theoretical calculation, it was proposed that the Au/BDT single molecular junctions can have the transmission curve whose slope at the Fermi level is positive. [74, 75] (Fig. 6.3.5.)

In the simultaneous measurement of thermopower and conductance at low temperature, IV characteristics and IETS were also measured in situ. (Fig.6.3.6. and Fig. 6.3.7.) By fitting IV characteristics of the 39 molecular junctions obtained in the measurements with Breit-Wigner formula (eq. 2-3-4), the energy gap between the conduction orbital and the Fermi energy (ε_0) was estimated to be 0.93 ± 0.44 eV. In the SERS and IV characteristic measurement, ε_0 was estimated to be 0.59 ± 0.11 eV. The average values of the ε_0 agreed with each other. The difference of the standard deviation between the MCBJ substrates and fixed nanogap electrodes indicates that the diversity of the electronic structure of the junction is larger for MCBJ substrate than the fixed nanogap electrodes.

Fig. 6.3.7.(a) and (c) show vibrational spectra (IETS) of Au/BDT junctions. In the spectra, the vibrational modes such as Au-S stretching mode were observed. (The assignments are shown in the captions.) The IETS measurements show that the BDT molecule actually bridged the Au electrodes. Next, I investigated the thermopower of the Au/BDT junctions, which was already characterized by IETS. Fig.6.3.7. (b) shows the conductance and thermopower as a function of time, where the separations of the electrodes were fixed.

The conductance value most frequently obtained by a previous study was 0.01 G_0[14]. Therefore, I assigned that value to our single molecular junction. From the conductance values in Fig.6.3.7. (b), the junction in these results were actually single molecular junctions. The single molecular junction in Fig. 6.3.7. (b) and (d) show the positive and negative thermopower values. These are results of the electron transport through HOMO and LUMO, respectively. In the simultaneous measurements of thermopower and conductance, the negative correlation between the absolute value of thermopower and conductance is seen, i.e. the absolute value of thermopower decreases as the conductance increases and vice versa.

I now discuss the negative correlation between the conductance and thermopower based on the single tunneling model. Assuming that the one molecular level dominates the transport, the transmission function is represented by the Lorentzian:

$$\tau(E) = \frac{4\Gamma_L\Gamma_R}{(E-\varepsilon_0)^2+(\Gamma_L+\Gamma_R)^2} \qquad (6\text{-}3\text{-}1)$$

where, ε_0 and $\Gamma_{L(R)}$ are the energy of the conduction orbital with respect to the Fermi level (E_F) of the electrodes and the strength of the coupling between the molecule and the left (right) electrode, respectively. The electronic conductance (G) of the junction is proportional to the $\tau(E)$ at Fermi level:

$$G = G_0 \tau(E_F) \quad (6\text{-}3\text{-}2)$$

Similarly, the thermopower of the molecular junction is related to $\tau(E)$:

$$S = -\frac{\pi^2 {k_B}^2 T}{3e} \frac{\partial ln\tau(E)}{\partial E} |_{E=E_F} \quad (6\text{-}3\text{-}3)$$

Thus, the electronic conductance is proportional to the transmission function at the Fermi level, while the thermopower is proportional to the slope of the transmission function at the Fermi level. The slope of the transmission function is large when the resonant peak is sharp and the Fermi level is at the steep part of the resonant peak. The resonant peak is broadened when the interaction (coupling) between the molecule and the metal electrodes in the single molecular junction increases. This broadening leads to a decrease in the above factor, i.e., a decrease in the thermopower of the single molecular junction, assuming that the energy of the resonant peak does not change significantly with the strength of the interaction. (Fig. 6.3.8.) A number of factors are known to affect, to a greater or lesser degree, the final electronic configuration of a molecular junction, thus ultimately altering its conductance and thermopower. Based on previously reported experimental and theoretical studies on thiol-terminated molecular wires, molecular orientation, i.e., molecular tilt angle, is the main factor that affects the electrical performance of molecular junctions(Fig. 6.3.9.)[76]. Increasing the tilt angle (θ = 0 for molecules perpendicular to the electrode's surface) results in an increase in hybridization of the thiol and phenyl termini with the Au surface states, which in turn leads to a marked increase in conductance. Based on this, the observed fluctuations in junction conductance were interpreted in terms of changes in the orientation of BDT within the metallic nanogap.

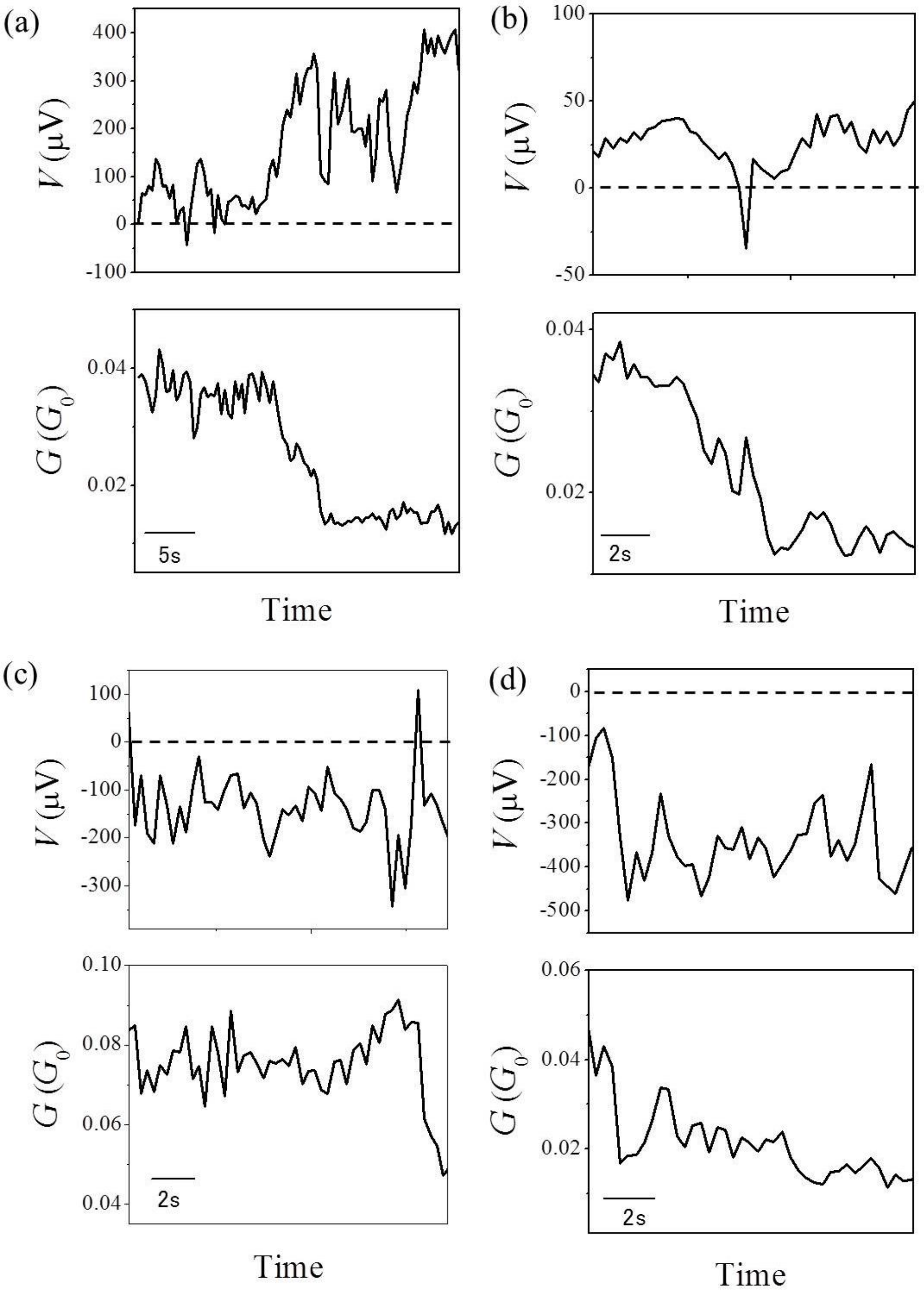

Fig. 6.3.1. Simultaneous conductance and thermoelectric voltage measurement during the breaking process. The contribution of the bulk Au is subtracted from the voltage signals. (a) The temperature of the hot (T_H) and cold (T_L) side were T_H = 323.9 K and T_L = 308.8 K, (b) T_H = 309.6 K, T_L = 307.0 K, (c) T_H = 320.1 K, T_L = 306.8 K, (d) T_H = 316.8 K, T_L = 307.8 K. The dashed lines indicate lines of V = 0V.

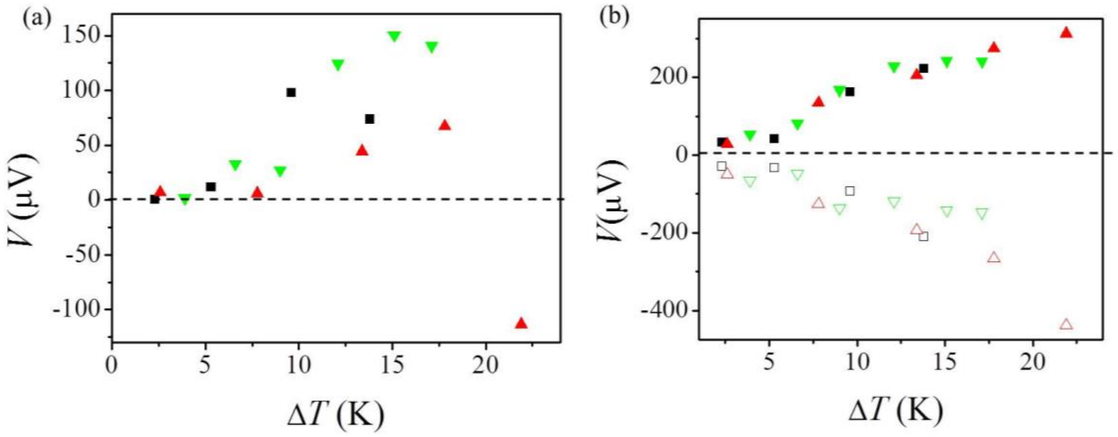

Fig. 6.3.2. (a) The average of the thermoelectric voltage as a function of temperature difference across the contact for the three experiments at room temperature. (b) The average of the thermoelectric voltage as a function of temperature difference across the junction for the three experiments. Colored points: The average for the positive voltage signals, Non-colored points: The average for the negative voltage signals. For (a) and (b), the contribution of bulk Au is subtracted. The dashed lines indicate lines of $V = 0\text{V}$.

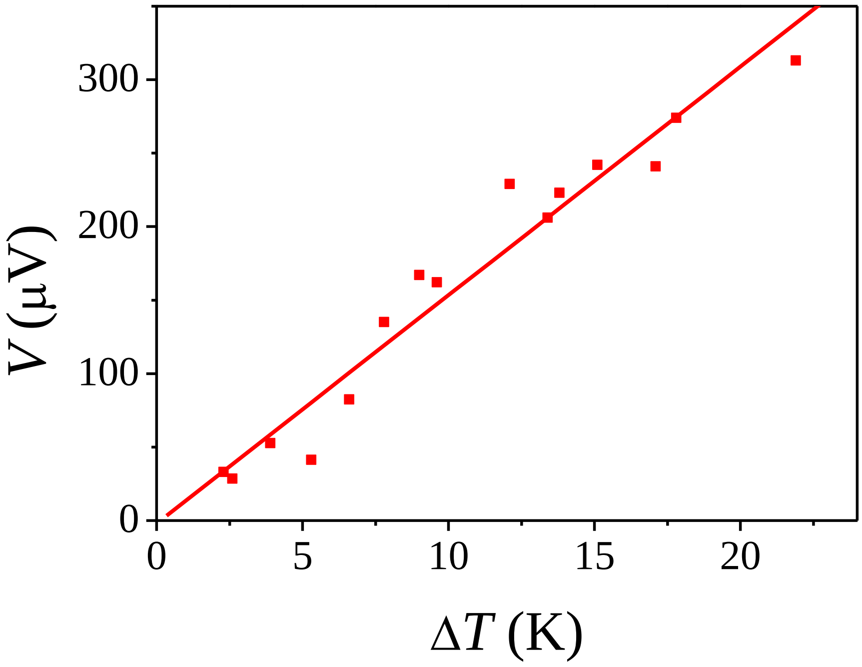

Fig. 6.3.3. The average of the thermoelectric voltage as a function of temperature difference across the junction at room temperature for the positive voltage signals. The red solid line is linear fitting result. The contribution of the bulk Au is subtracted from the voltage signals.

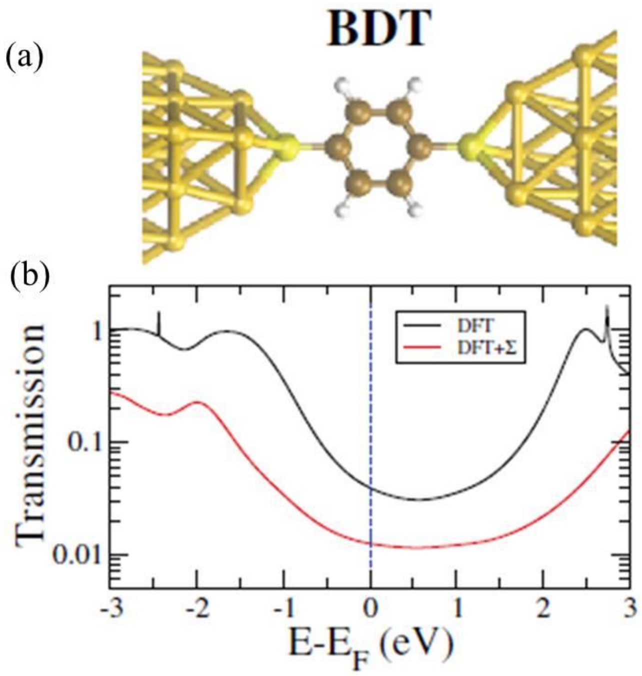

Fig. 6.3.4. Transmission curve in Au–BDT–Au junction. (a) Au–BDT–Au geometry investigated here. (b) The computed transmission curves as a function of the energy. The results obtained with the two *ab initio* methods are shown. For clarity, the position of the Fermi level is indicated by dashed vertical lines. Transport is dominated by the HOMO and slope at the Fermi level is negative. (= Thermopower is positive in sign.) From L. A. Zotti, M. Bürkle, F. Pauly, W. Lee, K. Kim, W. Jeong, Y. Asai, P. Reddy and J. C. Cuevas, Heat dissipation and its relation to thermopower in single-molecule junctions, *New Journal of Physics*, 2014, 16, 015004., used under the terms of the Creative Commons Attribution 3.0 licence.[73]

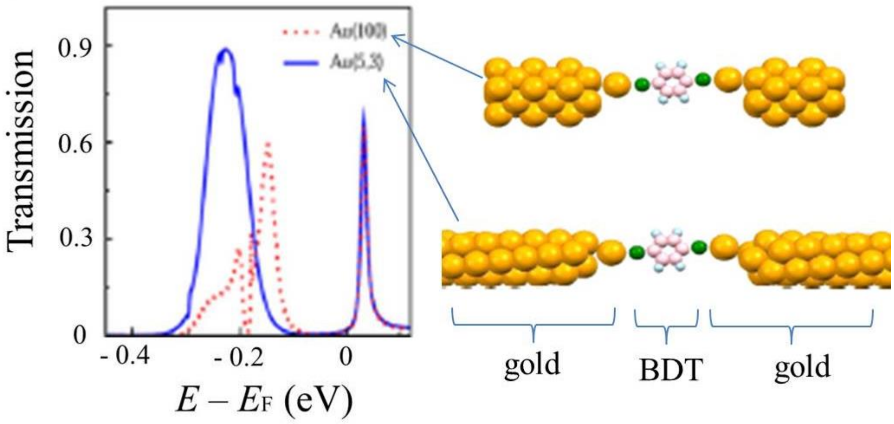

Fig.6.3.5. Transmission curves for the geometries shown on the right side of the graph. Adapted with prmission from A. Sen, C.-J. Lin and C.-C. Kaun, Single-Molecule Conductance through Chiral Gold Nanotubes, *The Journal of Physical Chemistry C*, 2013, 117, 13676. Copyright 2013 American Chemical Society.[74]

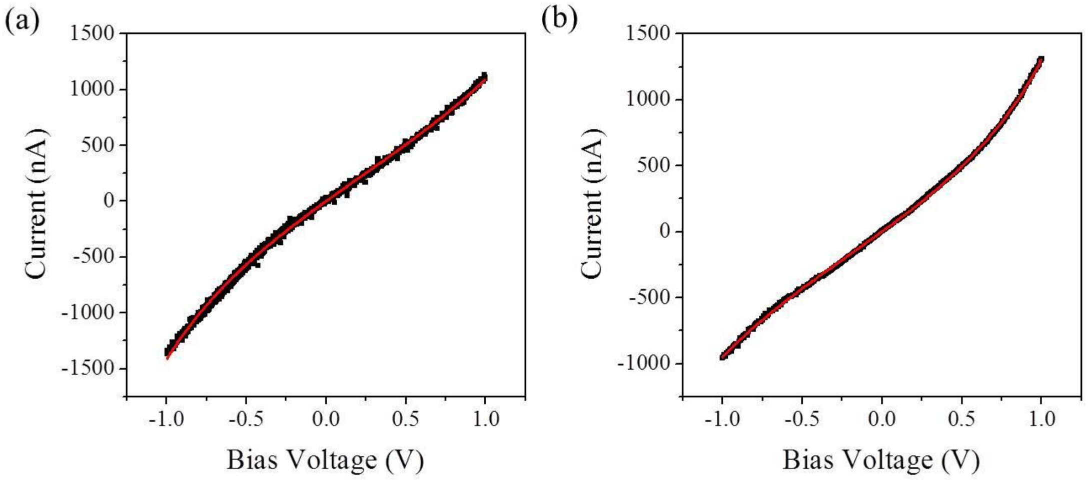

Fig.6.3.6. IV characteristics measured in the simultaneous measurement of thermopower and conductance. Black dots and solid red curves are the experimental results and fitting results with Breit-Wigner formula, respectively. (a) T_H = 21.3 K and T_L = 16.6 K, fitting result: ε_0 = 1.19 eV, Γ_L = 0.079 eV, Γ_R = 0.061 eV. (b) T_H = 40.5 K and T_L = 19.0 K, fitting result: ε_0 = 1.07 eV, Γ_L = 0.050 eV, Γ_R = 0.066 eV.

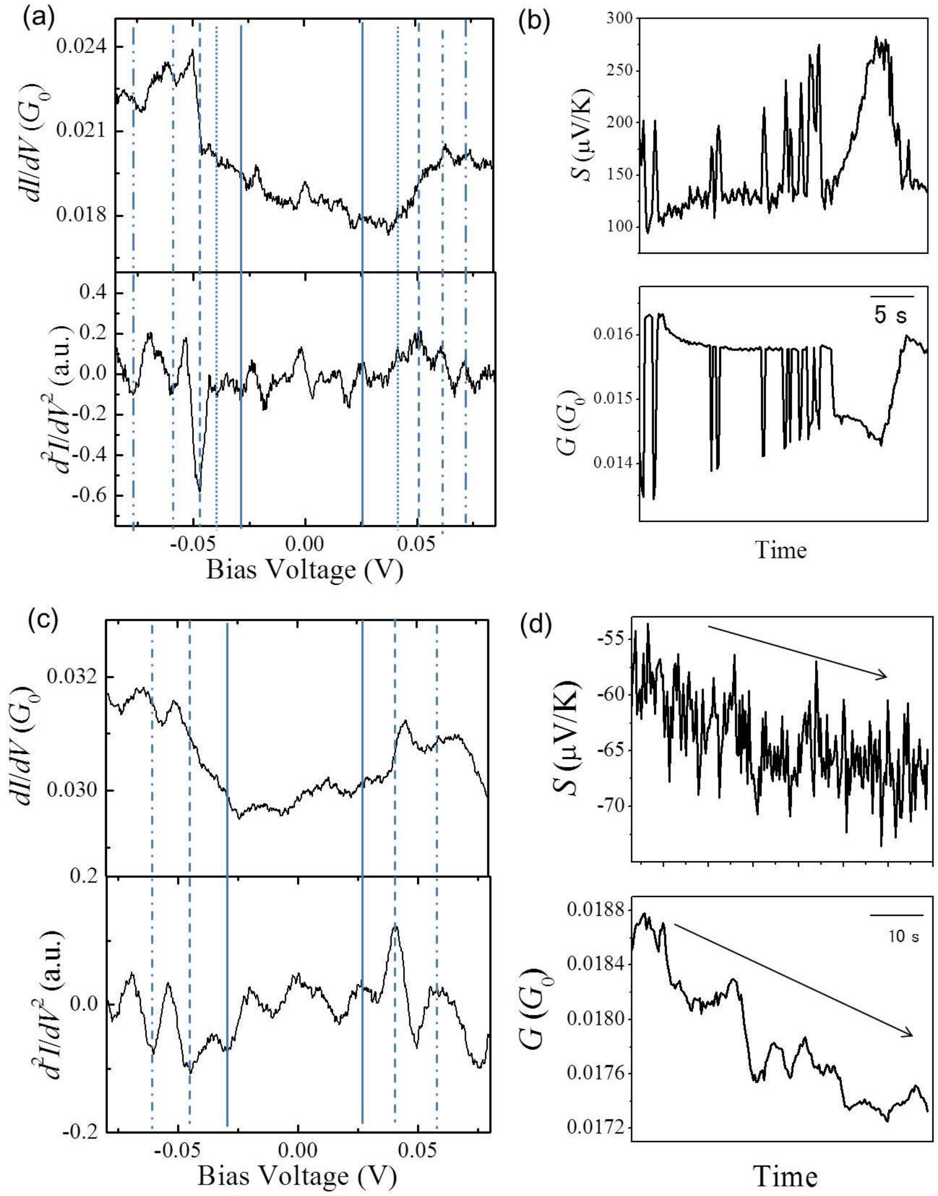

Fig,6.3.7. (a) IETS of the molecular junction. The peaks in dI^2/dV^2 are found at 27 (Au-S stretching), 41 (Au-S stretching), 49 (C-S stretching), 60 (C-C-C bending), and 74 mV (C-S stretching), respectively. (b) conductance (lower) and thermopower of the single BDT molecular junction as functions of time after the measurement of the spectrum in (a). T_H = 24.0 K, T_L = 19.9 K. (c) IETS of the molecular junction The peaks in dI^2/dV^2 are found at 28 (Au-S stretching), 43 (Au-S stretching), and 59 mV (C-S stretching), respectively. (d) conductance (lower) and thermopower of the single BDT molecular junction as functions of time after the measurement of the spectrum in (c). T_H = 23.5 K, T_L = 18.2 K. The lines are eye guides. [77]

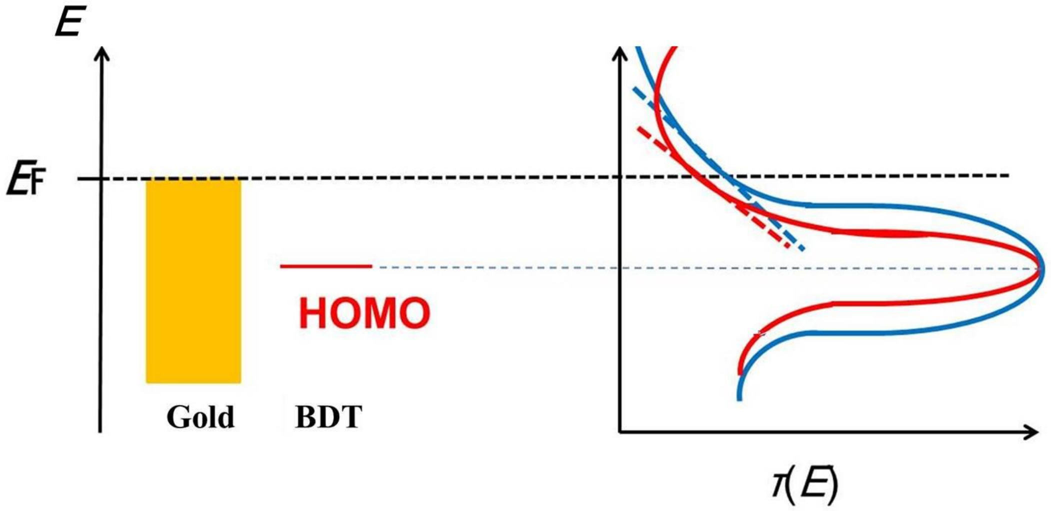

Fig. 6.3.8. Schematic energy diagram of the single BDT molecular junction for strong metal–molecule coupling (blue solid curve) and weak metal–molecule coupling (red solid curve) state in the case of the transport through HOMO. Red and blue dashed lines correspond to the slopes at the Fermi level.

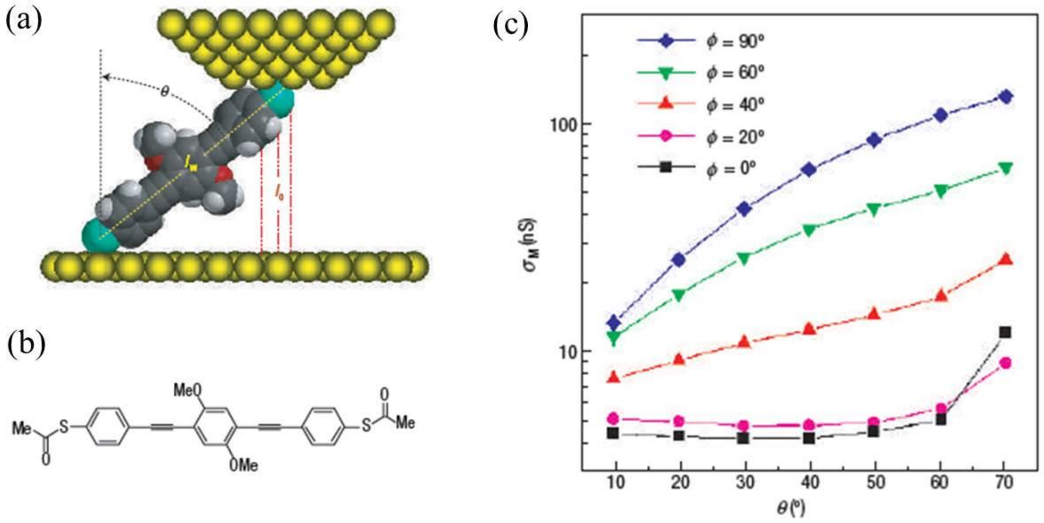

Fig. 6.3.9. (a) Schematic illustration of a single molecular junction. Molecule show a tilt angle (θ). (b) Objective molecule for the theoretical calculation shown in (c). (c) Conductance versus θ for five rigid rotations φ of the molecule about its axis bonded on hollow-to-top sites. For an angle of ϕ=0◦ (black squares) the plane of the end phenyl rings lies perpendicular to the gold (111) surface and for ϕ=90◦ (blue diamond) the end phenyl rings lie almost parallel to the gold surface. Reprinted with permission from W. Haiss, C. Wang, I. Grace, A. S. Batsanov, D. J. Schiffrin, S. J. Higgins, M. R. Bryce, C. J. Lambert and R. J. Nichols, Precision control of single-molecule electrical junctions ,*Nature Materials*, 2006, 5, 995-1002.Copyright 2006 Nature Publishing Group. [76]

6.4. Conclusion

The simultaneous measurements of thermopower and conductance at room temperature revealed that the Au/BDT molecular junctions have positive thermpower (transport through HOMO) mainly. The value of the positive thermopower agreed with the thermopower values of Au/BDT junctions obtained in the previous studies. On the other hand, negative thermopower was also observed.

Thermopower, conductance, IV characteristics and IETS were measured at low temperature in situ to understand the atomic and electronic structure of the junction in the dynamics comprehensively. From the results of the IV characteristics, the energy gap between the conduction orbital and the Fermi level (ε_0) was estimated to be 0.93 ± 0.44 eV in this measurement. IETS measurement provided the evidence confirming the presence of BDT molecules in the junction. The simultaneous measurements at low temperature revealed a negative correlations between the electrical conductance and the thermopower of the single molecular junction, thought to be attributable to the change in the strength of the interaction between the molecule and the metal electrodes. The thermopower of the single molecular junction decreases with an increase in the strength of the interaction between the molecule and the metal electrodes, assuming that one molecular level dominates the transport and that the energy of the molecular orbital does not change. Conversely, the conductance of the single molecular junction increases with an increase in the strength of the interaction between the molecule and the metal electrodes. The fluctuations in the thermopower and the electrical conductance reflect the changes in the orientation of the BDT molecule in the single molecular junction.

7, Concluding remarks

One of the characteristics of the molecular junction is the diversity of the physical property. The diversity is originated from the fluctuation of the atomic and electronic structure. To understand the origin of the physical property in the dynamics, it is necessary to analyze the atomic and electronic structure in the dynamics of the molecular junctions, which determine the physical property such as electron transport. In this study, some methods were combined and utilized to analyze the atomic and electronic structure of the junction in situ. Au/BDT junctions were chosen as the object of this study because there are many studies on the electron transport of the Au/BDT junctions in terms of theory and experiment. This system enables me to understand the experimental results in detail.

First, Raman spectra were measured with the measurement of the IV characteristics. The number of the molecules and electronic structure of the benzenedithiol molecular junction were determined by the *I*-*V* characteristics. The energy difference between conduction orbital and Fermi level was determined to be 0.6 eV based on the single level tunneling model considering that the Fermi distribution function got smeared out for finite temperature. The SERS spectra were different from that of the bulk crystal, due to the interaction between metal and molecule. The SH modes were not observed for the molecular junction, because the S-H bonds were broken and BDT molecule bound to both Au electrodes. The C=C (C-C) stretching mode was observed at 1562cm^{-1} (1063 cm^{-1}) for the molecular junction, while it was observed at 1572cm^{-1} (1094 cm^{-1}) in the bulk crystal. The redshift of the C=C and C-C stretching modes could be explained by the interaction between benzenedithiol molecule and Au. The apperance of the b_2 modes were observed for some molecular junctions, which were not observed in the bulk crystal. The appearance of the b_2 modes could be explained by the charge transfer between benzenedithiol molecule and Au electrodes. The basic knowlegde of the atomic and electronic structure of the Au/BDT junctions were obtined in this study. (Chapter 3)

Next, the system for the simultaneous measurement of thermopower and conductance was constructed to obtain the information of the slope of the transmission curve at the Fermi level. Thermopower measurements of the platinum-steel thermocouple were performed to check whether the thermopower measurements can be performed properly. The obtained value of the thermopower agreed with the literature values, which indicated that the measurements were performed properly. (Chapter 4)

After the construction of the system, simultaneous measurements of thermopower and conductance were performed for the single gold atomic junctions. The measurements were performed to (1) check whether the thermopower measurements can be performed properly for the atomic-sized system and (2) elucidate the thermoelectric property of the single gold atomic junctions which were used as the electrodes in the Au/BDT junctions. The thermoelectric voltage of the junctions fluctuated in the stretching process, and had both positive and negative values. The width of the voltage distribution decreased in the higher conductance region. The fluctuation of the thermoelectric voltage originates from the backscattering of electrons around the junctions. The deviation of the thermoelectric voltage was proportional to the temperature difference. This proportionality shows that the deviation of the voltage provides the information about the thermopower of the junctions. I found that the deviation of the thermopower decreased in the higher temperature region, which seems to contradict simple expectation. The unusual behavior can be explained by the improvement of the crystallinity around the junction via heating of the junctions. (Chapter 5)

Finally, thermopower measurements were performed for the Au/BDT junctions. In addition to the thermopower measurement, IETS and IV characteristics were also measured at low temperature in situ to elucidate the atomic and electronic structure comprehensively in the dynamics of the junctions. The simultaneous measurements of thermopower and conductance at room temperature revealed that the Au/BDT molecular junctions have positive thermpower mainly. The value of the positive thermopower agreed with the thermopower values of Au/BDT junctions obtained in the previous studies. Thermopower, conductance, IV characteristics and IETS were measured at low temperature in situ to understand the atomic and electronic structure of the junction comprehensively in the dynamics. From the results of the IV characteristics, the energy gap between the conduction orbital and the Fermi level (ε_0) was estimated to be 0.93 ± 0.44 eV in this measurement. IETS measurement provided the evidence confirming the presence of BDT molecules in the junction. The simultaneous measurements at low temperature revealed negative correlations between the electrical conductance and the thermopower of the single molecular junction, thought to be attributable to the change in the strength of the interaction between the molecule and the metal electrodes. The thermopower of the single molecular junction decreases with an increase in the strength of the interaction between the molecule and the metal electrodes, assuming that one molecular level dominates the transport and that the energy of the molecular orbital does not change. Conversely, the conductance of the single molecular junction increases with an increase in the strength of the interaction between the molecule and the metal electrodes. The fluctuations in the thermopower and the electrical conductance reflect the changes in the orientation of the BDT molecule in the single molecular junction. (Chapter 6)

As stated in 1.3., the diversity of the physical property is one of the characteristics of the molecular junction. The diversity can be observed in the dynamics. Therefore, it is necessary to analyze the atomic and electronic structure in the dynamics. In situ measurement system constructed in this study will contribute to the understanding the atomic and electronic structure of the junction comprehensively and search for the novel property of the junction.

8, References

1. A. Zangwill, *Physics at Surfaces* Cambridge University Press, 1988.
2. K. S. Novoselov, V. I. Falko, L. Colombo, P. R. Gellert, M. G. Schwab and K. Kim, *Nature*, 2012, 490, 192.
3. J. C. Cuevas and E. Scheer, *Molecular Eelctronics: An Introduction to Theory and Experiment*, World Scientific Publishing Co. Pte. Ltd., Singapore, 2010.
4. M. Kiguchi and S. Kaneko, *Physical chemistry chemical physics : PCCP*, 2013, 15, 2253-2267.
5. A. Aviram and M. A. Ratner, *Chemical Physics Letters*, 1974, 29, 277.
6. R. M. Metzger, B. Chen, Ulf Ho1pfner, M. V. Lakshmikantham, D. Vuillaume, T. Kawai, X. Wu, H. Tachibana, T. V. Hughes, J. Hiromi Sakurai, W. Baldwin, C. Hosch, M. P. Cava, L. Brehmer and G. J. Ashwell, *Journal of the American Chemical Society*, 1997, 119, 10455.
7. R. E. Holmlin, R. Haag, M. L. Chabinyc, R. F. Ismagilov, A. E. Cohen, A. Terfort, M. A. Rampi and G. M. Whitesides, *Journal of the American Chemical Society*, 2001, 123, 5075.
8. H. Song, Y. Kim, Y. H. Jang, H. Jeong, M. A. Reed and T. Lee, *Nature*, 2009, 462, 1039-1043.
9. H. Ohnishi, Y. Kondo and K. Takayanagi, *Nature*, 1998, 395, 780.
10. M. A. Reed, C. Zhou, C. J. Muller, T. P. Burgin and J. M. Tour, *Science*, 1997, 278, 252-254.
11. R. H. M. Smit, Y. Noat, C. Untiedt, N. D. Lang, M. C. van Hemert and J. M. van Ruitenbeek, *Nature*, 2002, 419, 906-909.
12. S. Y. Quek, M. Kamenetska, M. L. Steigerwald, H. J. Choi, S. G. Louie, M. S. Hybertsen, J. B. Neaton and L. Venkataraman, *Nature nanotechnology*, 2009, 4, 230-234.
13. I. Diez-Perez, J. Hihath, Y. Lee, L. Yu, L. Adamska, M. A. Kozhushner, Oleynik, II and N. Tao, *Nature chemistry*, 2009, 1, 635-641.
14. B. Q. Xu and N. J. J. Tao, *Science*, 2003, 301, 1221-1223.
15. C. Kittel, *Introduction to Solid State Physics*, Wiley, USA, 2004.
16. T. Konishi, M. Kiguchi, M. Takase, F. Nagasawa, H. Nabika, K. Ikeda, K. Uosaki, K. Ueno, H. Misawa and K. Murakoshi, *Journal of the American Chemical Society*, 2013, 135, 1009-1014.
17. D. R. Ward, N. J. Halas, J. W. Ciszek, J. M. Tour, Y. Wu, P. Nordlander and D. Natelson, *Nano letters*, 2008, 8, 919-924.

18. 濱口宏夫 and 平川暁子, *ラマン分光法*, 学会出版センター, 日本, 1988.
19. C. V. Raman and K. S. Krishnan, *Nature*, 1928, 121, 501.
20. S. Marqués-González, R. Matsushita and M. Kiguchi, *Journal of Optics*, 2015, 17, 114001.
21. S. Nie and S. R. Emory, *Science*, 1997, 275, 1102-1106.
22. 岡本隆之 and 梶川浩太郎, *プラズモニクス—基礎と応用*, 講談社, 日本, 2010.
23. A. García-Martín, D. R. Ward, D. Natelson and J. C. Cuevas, *Physical Review B*, 2011, 83, 193404.
24. K. Ikeda, J. Sato, N. Fujimoto, N. Hayazawa, S. Kawata and K. Uosaki, *Journal of Physical Chemistry C*, 2009, 113, 11816–11821.
25. J. R. Lombardi, R. L. Birke, T. Lu and J. Xu, *J. Chem. Phys.*, 1986, 84, 4174-4180.
26. M. Osawa, N. Matsuda, K. Yoshii and I. Uchida, *Journal of Physical Chemistry*, 1994, 98, 12702-12707.
27. R. Jaklevic and J. Lambe, *Physical Review Letters*, 1966, 17, 1139-1140.
28. B. C. Stipe, M. A. Rezaei and W. Ho, *Science*, 1998, 280, 1732-1735.
29. M. Kiguchi and R. Matsushita, *Molecular Electronics An Experimental and Theoretical Approach*, Pan Stanford Publishing, Singapore, 2015.
30. M. Kiguchi, O. Tal, S. Wohlthat, F. Pauly, M. Krieger, D. Djukic, J. Cuevas and J. van Ruitenbeek, *Physical Review Letters*, 2008, 101, 046801.
31. Y. Kim, T. Pietsch, A. Erbe, W. Belzig and E. Scheer, *Nano letters*, 2011, 11, 3734-3738.
32. Z. Zhang, Z. Yang, J. Yuan and M. Qiu, *The Journal of chemical physics*, 2008, 128, 044711.
33. G. C. Liang, A. W. Ghosh, M. Paulsson and S. Datta, *Physical Review B*, 2004, 69.
34. *Thermoelectrics Handbook Macro to Nano*, CRC press, USA, 2006.
35. *輸送現象測定*, 丸善, 日本, 2000.
36. B. Ludoph and J. M. v. Ruitenbeek, *Physical Review B*, 1999, 59, 12290-12293.
37. P. Reddy, S. Y. Jang, R. A. Segalman and A. Majumdar, *Science*, 2007, 315, 1568-1571.
38. H. Nakamura, T. Ohto, T. Ishida and Y. Asai, *Journal of the American Chemical Society*, 2013, 135, 16545-16552.
39. Y. Dubi, *The Journal of chemical physics*, 2013, 138, 114706.
40. Y. Dubi and M. Di Ventra, *Reviews of Modern Physics*, 2011, 83, 131-155.
41. J.-H. Tian, B. Liu, X. Li, Z.-L. Yang, B. Ren, S.-T. Wu, N. Tao and Z.-Q. Tian, *J. Am. Chem. Soc.*, 2006, 128, 14748-14749.
42. Z. Liu, S. Y. Ding, Z. B. Chen, X. Wang, J. H. Tian, J. R. Anema, X. S. Zhou, D. Y. Wu,

B. W. Mao, X. Xu, B. Ren and Z. Q. Tian, *Nature communications*, 2011, 2, 305.

43. Z. Ioffe, T. Shamai, A. Ophir, G. Noy, I. Yutsis, K. Kfir, O. Cheshnovsky and Y. Selzer, *Nature nanotechnology*, 2008, 3, 727-732.
44. S. Guo, J. Hihath, I. Diez-Perez and N. Tao, *Journal of the American Chemical Society*, 2011, 133, 19189-19197.
45. C. M. Guedon, H. Valkenier, T. Markussen, K. S. Thygesen, J. C. Hummelen and S. J. van der Molen, *Nature nanotechnology*, 2012, 7, 305-309.
46. E. H. Huisman, C. M. G. don, B. J. v. Wees and S. J. v. d. Molen, *Nano letters*, 2009, 9, 3909.
47. R. Matsuhita, M. Horikawa, Y. Naitoh, H. Nakamura and M. Kiguchi, *The Journal of Physical Chemistry C*, 2013, 117, 1791-1795.
48. J. G. Simmons, *Journal of Applied Physics*, 1963, 34, 1793.
49. R. Dahlke and U. Schollwock, *Physical Review B*, 2004, 69, 085324.
50. F. Chen, X. Li, J. Hihath, Z. Huang and N. Tao, *Journal of the American Chemical Society*, 2006, 128, 15874.
51. P. Atkins, T. Overton, J. Rourke, M. Weller and F. Armstrong, *Shriver and Atkins Inorganic Chemistry*, Oxford University Press, UK, 2006.
52. K. Ikeda, S. Suzuki and K. Uosaki, *Nano letters*, 2011, 11, 1716-1722.
53. Y.-F. Huang, H.-P. Zhu, G.-K. Liu, D.-Y. Wu, B. Ren and Z.-Q. Tian, *Journal of the American Chemical Society*, 2010, 132, 9244.
54. K. Kim, K. L. Kim, H. B. Lee and K. S. Shin, *The Journal of Physical Chemistry C*, 2012, 116, 11635-11642.
55. F. J. Blatt, D. J. Flood, V. Rowe, P. A. Schroeder and J. E. Cox, *Physical Review Letters*, 1967, 18, 395-396.
56. M. Tsutsui, T. Morikawa, A. Arima and M. Taniguchi, *Scientific reports*, 2013, 3, 3326.
57. R. Matsushita, S. Kaneko, S. Fujii, H. Nakamura and M. Kiguchi, *Nanotechnology*, 2015, 26, 045709.
58. J. A. Malen, P. Doak, K. Baheti, T. D. Tilley, A. Majumdar and R. A. Segalman, *Nano letters*, 2009, 9, 3406-3412.
59. N. Agraït, A. L. Yeyati and J. M. van Ruitenbeek, *Physics Reports*, 2003, 377, 81-279.
60. F. Pauly, J. K. Viljas, M. Bürkle, M. Dreher, P. Nielaba and J. C. Cuevas, *Physical Review B*, 2011, 84.
61. J. K. Viljas and J. C. Cuevas, *Physical Review B*, 2007, 75.
62. C. Untiedt, G. R. Bollinger and N. Agrait, *Physical Review B*, 2000, 62, 99962-99965.
63. P. Buffat and J. P. Borel, *Physical Review A*, 1976, 13, 2287-2298.

64. T. Castro, R. Reifenberger, E. Choi and R. Andres, *Physical Review B*, 1990, 42, 8548-8556.
65. L. Nan, D. Allan and L. Gang-Yu, *ACTA PHYSICA SINICA (Overseas Edition)*, 1997, 6, 531-549.
66. O. Malis, C. Byard, D. Mott, B. N. Wanjala, R. Loukrakpam, J. Luo and C. J. Zhong, *Nanotechnology*, 2011, 22, 025701.
67. D. R. Peale, *Journal of Vacuum Science & Technology A: Vacuum, Surfaces, and Films*, 1992, 10, 2210.
68. H. Rascon-Ramos, J. M. Artes, Y. Li and J. Hihath, *Nature materials*, 2015, 14, 517-522.
69. S. Kaneko, Y. Nakamura, R. Matsushita, S. Marqués-González and M. Kiguchi, *Applied Physics Express*, 2015, 8, 065201.
70. W. B. Pearson, *Soviet Physics Solid State*, 1961, 3, 1024.
71. A. M. Guenault and D. G. Hawksworth, *J. Phys. F: Metal Phys.*, 1977, 7, 219.
72. M. Tsutsui, T. Morikawa, Y. He, A. Arima and M. Taniguchi, *Scientific reports*, 2015, 5, 11519.
73. L. A. Zotti, M. Bürkle, F. Pauly, W. Lee, K. Kim, W. Jeong, Y. Asai, P. Reddy and J. C. Cuevas, *New Journal of Physics*, 2014, 16, 015004.
74. A. Sen, C.-J. Lin and C.-C. Kaun, *The Journal of Physical Chemistry C*, 2013, 117, 13676-13680.
75. H. C. Nguyen, B. M. Szyja and N. L. Doltsinis, *Physical Review B*, 2014, 90.
76. W. Haiss, C. Wang, I. Grace, A. S. Batsanov, D. J. Schiffrin, S. J. Higgins, M. R. Bryce, C. J. Lambert and R. J. Nichols, *Nature materials*, 2006, 5, 995-1002.
77. L.-L. Lin, Chuan-Kui and a. Y. L. Wang, *ACS Nano*, 2011, 5, 2257.